HEAT TRANSFER ENHANCEMENT IN IMPINGING ROUND JETS

HEAT TRANSFER ENHANCEMENT IN IMPINGING ROUND JETS

By

NAN GAO, B. ENG.

A Thesis

Submitted to the School of Graduate Studies

in Partial Fulfilment of the Requirements

for the Degree

Master of Engineering

McMaster University

MASTER OF ENGINEERING (2001) MCMASTER UNIVERSITY

(Mechanical Engineering) Hamilton, Ontario

TITLE: Heat Transfer Enhancement In Impinging Round Jets

AUTHOR: Nan Gao

B. ENG.(Thermal Engineering)

Tsinghua University, Beijing, China, 1997

SUPERVISOR: Dr. Dan Ewing

NUMBER OF PAGES: xxiv, 143

TO MAMA AND BABA

Abstract

Measurements of the heat transfer produced by a round impinging jet exiting a fully developed pipe with a Reynolds number of 23,000 were performed for jet-to-plate spacing, H, ranging from 0.25 to 10 diameters, D. This included extending previous measurements by examining the Nusselt number distributions at every diameter increase in the jet-to-plate spacing, examining the effect of confinement on the heat transfer produced by the jet, measuring the heat transfer enhancement that can be achieved by adding tabs to the pipe outlet to enhance mixing in the jet, and measuring the heat transfer enhancement produced by adding trips on the impingement surface to promote turbulence in the wall jet. Flow visualization experiments, measurements of velocity field in the jet, and measurements of the dynamic pressure on the wall were performed to develop a greater insight into the development of the flow field in the configuration studied here.

The initial measurements of the impinging jet provide more detailed information on the change in the heat transfer as the impingement distance changes from 2 to 10 diameters. It was found that the heat transfer in the impingement region, $r/D \leq 0.5$, changed with jet-to-plate spacings but the heat transfer in the initial region of the wall jet $0.5 \leq r/D \leq 1.5$ was essentially independent of jet-to-plate spacing for $2 \leq H/D \leq 8$. The heat transfer for $r/D \geq 1.5$ differed significantly with jet-to-plate spacing. For spacings less than 3 diameters there was a strong secondary peak, previously observed. The level of the secondary peak decreased significantly for great separation distances

but it was found there was an observable inflection in the heat transfer distribution for impingement distances up to 7 diameters. Measurements of the dynamic wall pressure spectra and spatial correlations in the region of this secondary peak for jet-to-plate spacings of 2 and 4 diameters indicated this secondary peak was caused by the same mechanism, namely separation and break down of the vortex ring structures that developed in the jet. The vortex rings decay as they develop in the jet so it is not unexpected that they make a smaller contribution to the heat transfer in the wall jet as the jet-to-plate spacing increases.

Measurements of the heat transfer in the confined and unconfined impinging jet showed that the confinement enhanced the heat transfer in the impingement zone and the initial portion of the wall jet, $0 \leq r/D \leq 2$, for jet-to-plate spacings ranging from $0.25 \leq H/D \leq 2$. Measurements of the dynamic wall pressure suggested that the heat transfer enhancement was caused by the confining walls altering the dynamics of the large-scale structures in the impinging jet, though the exact mechanisms could not be determined from the measurements. The measurements also showed the heat transfer was reduced in the region $r/D \geq 2$ for jet-to-plate spacings less than 3 diameters, likely caused by the confinement altering the entrainment of cool ambient air into this region. In both causes the confinement had the largest effect on the heat transfer for the smallest jet-to-plate spacing.

The measurements of the heat transfer for impinging jets with tabs on the pipe outlet showed that the average Nusselt number in the region $r/D \leq 3$ could be enhanced by up to 4-5%. Larger heat transfer enhancement could be achieved using larger tabs. Measurements of the velocity field showed that the effect of the tabs differed depending on the number of tabs used in the array and the distance the impingement plate was positioned downstream of the outlet. In a 6 tab array, the blockage caused by the tabs seemed to be the dominant effect near the pipe outlet. This blockage created jets of high speed fluid between tabs that caused 6 regions of heat transfer

enhancement on the plate when the jet-to-plate spacing was 2 diameters. For larger spacing the mixing caused by the streamwise vortices generated on the plate diffused these jets causing a more uniform heat transfer enhancement in the region $r/D \leq 2$. For arrays with larger number of tabs 10, 12, and 16, the enhanced mixing seemed to dominate the blockage effect for the jet-to-plate spacing $2 \leq H/D \leq 6$ considered here.

It was found that the addition of trips on the impingement surface also enhanced the Nusselt number on the surface by up to 50%. It was found that the most significant heat transfer enhancement was caused by the first trip. Later trips had a smaller or in some cases a detrimental effect even when the spacing between the trips exceed 10 trip heights. Measurements of the dynamic wall pressure showed the trips enhanced the heat transfer by introducing small-scale turbulent motions in the separated region behind the trip. In the impinging jet, though, the trip also have a global effect on the evolution of the large-scale structures. For example, positioning a trip at $r/D=0.5$, which corresponds to the jet outlet, suppressed the heat transfer over the entire impingement region. The turbulence introduced by the trip also appears to suppress the separation of vortex ring and the secondary peak in the heat transfer associated with the event. Thus, the trip has a global effect on the heat transfer in the flow. The results suggest the heat transfer could be best enhanced using a single trip placed between $0.5 \leq r/D \leq 1.0$.

Acknowledgements

The author wishes to express his gratitude to his supervisor, Dr. Dan Ewing. His encouragement and advice were invaluable throughout the course of this study.

The author also greatly appreciates the time and efforts Dr. Ross Judd and Dr. Chan Ching put into reviewing this thesis.

Gratitude is also extended to Mr. Ron Lodewyks, Mr. Jim McLaren, Mr. Dave Schick, and Mr. Joe Verhaeghe for the kindly help.

Thanks also to Dr. J.S. Chang and Mr. Barry Diacon for kindly lending us the equipment.

Nomenclature

A   area of impingement plate, m^2

B_{pp} Fourier transform of azimuthal pressure correlation, V^2

b   tab height, m

C   trip-to-plate distance, m

D   nozzle diameter, m

F   pressure spectrum, $V^2/$Hz

f   frequency, Hz

f_e excitation frequency, Hz

f_n natural frequency, Hz

h   heat transfer coefficient, W/m^2K

h_o stagnation heat transfer coefficient, W/m^2K

H   jet to plate spacing, m

$\overline{h}$ average heat transfer coefficient, W/m^2K

I   current through the stainless steel foil, A

k_a thermal conductivity of air, W/mK

k_f thermal conductivity of stainless steel foil, W/mK

L_a depth of the air gap under the foil, m

M   Mach number

Nu   local Nusselt number, hD/k_a

$\overline{Nu}$ average Nusselt number, $\overline{h}D/k_a$

Nu_o stagnation Nusselt number, $h_o D / k_a$

P   trip-to-trip distance, m

Pr   Prantl number, ν / α

q_{cond} conduction heat flux loss, W/m^2

q_{conv} surface local convective heat flux, W/m^2

q_{rad} surface radiation heat flux, W/m^2

q_t total heat flux, W/m^2

r   radial coordinate of the surface, m

R   impingement plate electrical resistance, Ω

R_{pp} azimuthal correlation of dynamic wall pressure, V^2

Re   Reynolds number, $\overline{U} D / \nu$

r_R local surface recovering factor

St   Strouhal number, $f D / \overline{U}$

t   trip thickness and width, m

T_{aw} adiabatic wall temperature, K

T_{awo} stagnation adiabatic wall temperature, K

T_f film temperature, K

t_f half thickness of the foil, m

T_j jet temperature, K, $^o C$

T_j^o measured(total) jet temperature, K

T_j^* non-dimensional jet temperature

T_w local wall temperature, K

T_{wo} stagnation wall temperature, K

T_∞ ambient temperature, K

Tu   ratio of streamwise fluctuation velocity to mean velocity, u'/U

u' root mean square streamwise velocity, $u' = (\overline{u^2})^{1/2}$, m/s

U   local mean streamwise velocity, m/s

$\overline{U}$	average mean streamwise velocity, $4\dot{V}/\pi D^2$, m/s
U_{max}	local maximum mean velocity, m/s
$\dot{V}$	volume flow rate, m^3/s
V	voltage across the stainless steel foil, V
V_p	voltage given by pressure transducer and microphone, V
W	slot jet width, m
x	a spatial coordinate in a cartesian system, m
y	a spatial coordinate in a cartesian system, m
z	a spatial coordinate in a cartesian system, m
η	heat transfer enhancement factor, $h_{modified}/h_{original} - 1$
η^+	inner length scale in the pipe, m
γ	ratio of specific heat of air, c_p/c_v
ν	kinematic viscosity of air at film temperature, m^2/s
σ	Stefan-Boltzmann constant, $5.67 \times 10^{-8} W/m^2 K^4$,
ε_u	emissivity of the upper surface,
ε_b	emissivity of the bottom surface.

Contents

List of Tables

List of Figures

xv

xviii

xxii

Chapter 1

Introduction

Impinging jets are used to cool or dry surfaces in numerous practical applications ranging from annealing in steel making, shown in Figure 1.1, to impingement cooling inside gas turbine blades or electronic packages. The impinging jets used in these applications are typically classified according to geometry of the jet nozzle, the impingement surface, and the features of the flow. These include (a) the working fluids: i.e., submerged versus free jet, (b) the shape of the nozzle, (c) the orientation of the nozzle relative to the surface, (d) the presence of a confining wall, and (e) whether it is a single jet or an array of jets. Examples of these classifications are illustrated in Figure 1.2. Changing any of these features can and often does have a significant effect on the evolution of the impinging jets and the heat transfer produced by the jet. For example, a liquid jet in air, is normally unaffected by the presence of the ambient air so the jet velocity and diameter are normally only changed by the gravitation force. Thus, the heat transfer caused by the jet is unaffected by the jet-to-plate spacing if the acceleration of the jet by gravity is negligible. On the other hand, an air jet exiting in ambient air, or a submerged jet, will entrain fluid from the ambient as it evolves causing the jet to spread and the centerline velocity to decay. Thus, the heat transfer produced by the jet changes significantly with changes in the jet-to-plate
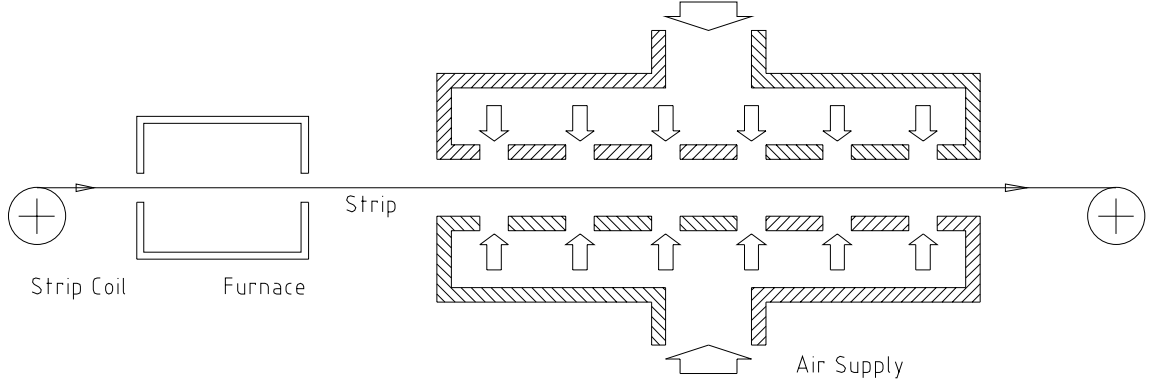
Figure 1.1: Application of Impinging jet: Schematic of continuous steel strip annealing line[1].

spacing. The research here will focus on a round submerged jet directed normal to a flat plate. Minor modification will be made to the nozzle geometry in an attempt to enhance the heat transfer but the basic geometry will always be a round nozzle.

This investigation will focus on cases where the impingement surface is located in the near field of the round jet since it is well known that the heat transfer is largest for these cases. For example, the local Nusselt number distribution for nozzle-to-plate spacings of 2, 6 and 10 diameters are shown in Figure 1.3. The Nusselt number is given by

$$Nu = \frac{hD}{k_a}, \tag{1.1}$$

where D is the nozzle diameter, k_a is the thermal conductivity of air, and the heat transfer coefficient given by

$$h = \frac{q_{conv}}{T_w - T_j}. \tag{1.2}$$

Here, q_{conv} is the convective heat flux, T_w is the wall temperature, and T_j is the jet temperature. It is clear that heat transfer rates at small jet-to-plate spacings H/D=2 and 6 are larger than for H/D=10 in the region $r/D < 4$.

The heat transfer produced by the impinging jet is a function of a number of

(a)

Gas

Gas

Gas

Liquid

Gas –Gas Submerged Jet   Liquid-Gas Free Jet

(b)

D

W

Round Jet   Slot Jet

(c)

Normally Impinged Jet   Obliquely Impinged Jet

(d)

D

D

Round Jet   Round Jet with
Confinement

(e)

D

D

Single round Jet   Multiple Round Jets
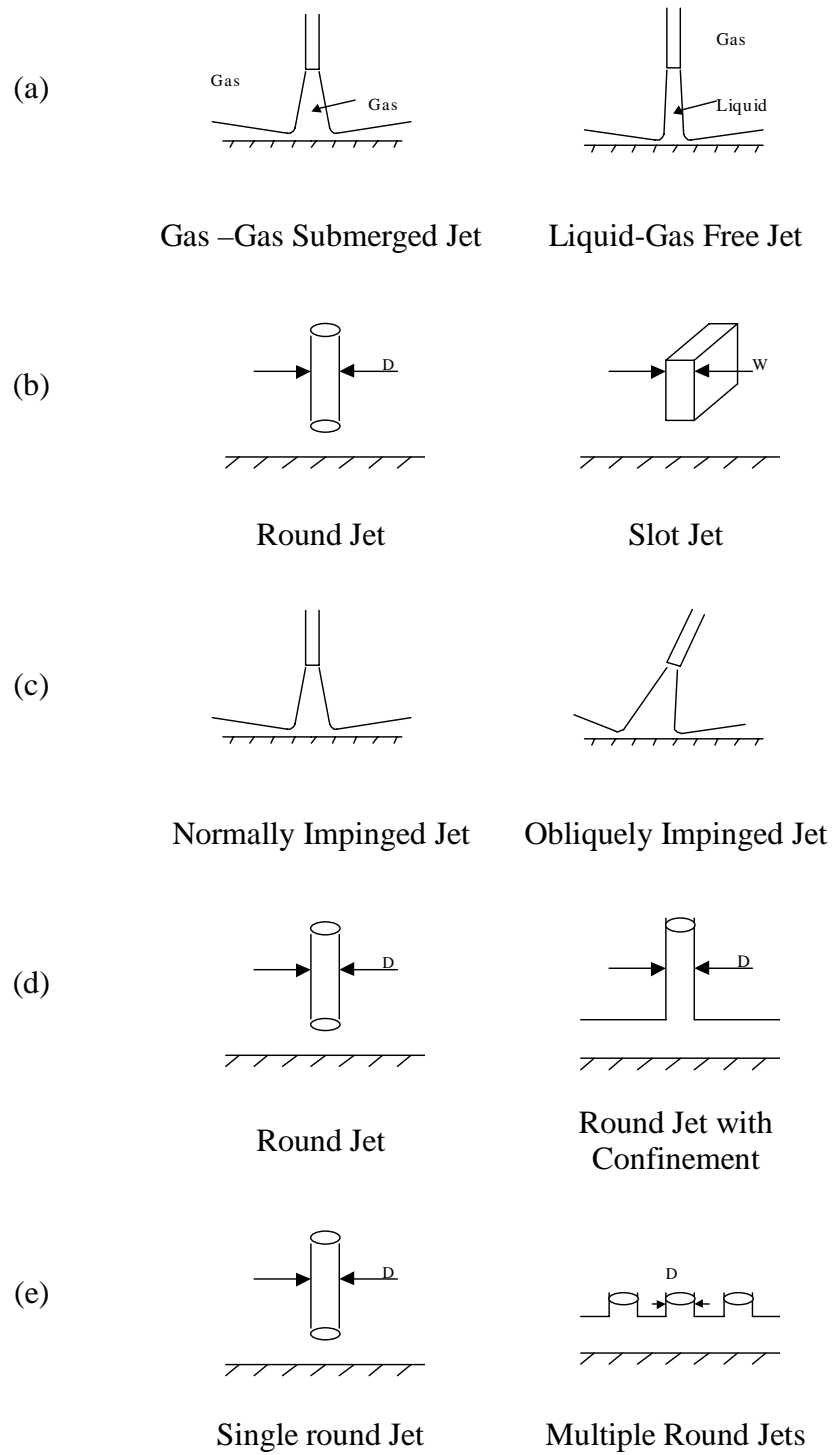
Figure 1.2: Jet classification.
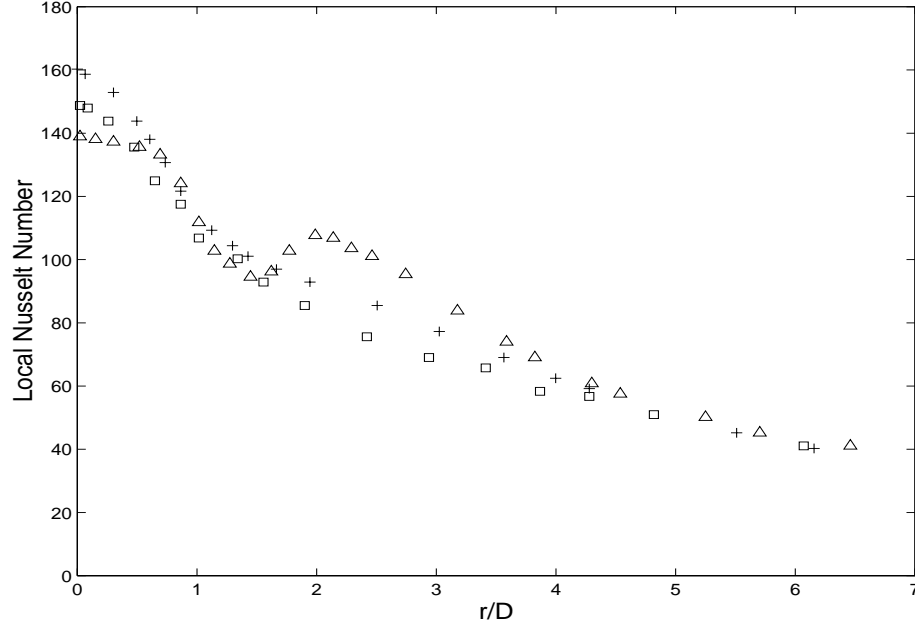
Figure 1.3: Local Nusselt Number distribution for jet issuing from a long pipe at Re=23,750[26] for $\triangle$ H/D=2, + H/D=6, $\square$ H/D=10.

variables. The functional dependence in non-dimensional form can be written as

$$Nu = Nu(Re, Pr, Tu, H/D, r/D, *),\qquad(1.3)$$

where Re is Reynolds number, Pr is Prantl number, Tu is turbulence intensity, H/D is jet-to-plate spacing, r/D is the lateral displacement from stagnation point, and * is used to represent any other geometric factor. The augment of turbulence level will enhance the stagnation Nusselt number for $1 \leq H/D \leq 10$ [24].

As with many practical devices, there is a great deal of interest in increasing the efficiency of the impinging jet by enhancing the heat transfer produced for a given mass flow rate or Reynolds number. A number of different techniques have been developed to enhance the heat transfer including modifying the nozzle geometry, pulsing the jet, and adding turbulence promoters or fins on the impingement surface. Many of these approaches are designed to modify the large-scale turbulent structures in order to increase entrainment into the jet and the mixing process in the flow. In most

of these investigations, little or no effort was made to establish how the flow field of the impinging jet was modified by the heat transfer enhancement technique. Further, although significant heat transfer enhancements have been observed, many of the technologies that achieved enhancement can not be utilized in practical engineering applications.

The objective of this project is to examine two different techniques to enhance the heat transfer. The first that has not been examined previously is to add tabs on the jet outlet. It is well know that these tabs enhance the mixing in free jets and it is expected this should enhance the heat transfer in impinging jet. The second approach is to use trips on the impingement surface that will enhance the turbulence in the wall and hence the heat transfer on the wall. Flow measurement and flow visualization will also be performed to understand how these strategies affect the flow structure and, in turn enhance the heat transfer rate.

hello

Chapter 2

Literature Review

There have been numerous investigations of the heat transfer produced by a submerged impinging round jet (hereafter the submerged round jet is implied) for a range of jet-to-plate spacing and nozzle configurations. It is well known that the heat transfer produced by these jets varies significantly with jet-to-plate spacings because of the development of the jet after it exits the orifice. Thus, a brief review of the characteristics of the flow field in the round jet and round impinging jet is included before proceeding to a review of heat transfer measurements. This is then followed by a discussion of investigations that have attempted to enhance the heat transfer produced by impinging jets.

2.1 Flow Field in the Round Jet

The evolution of the round jet is generally broken down into three regions illustrated in Figure 2.1. In the first region or near field the shear layer develops causing the turbulence intensity of the flow to increase as it evolves downstream. The center of the jet in this region is called the potential core because the flow in this region is irrotational for a jet exiting a contoured nozzle and the turbulent motions in this
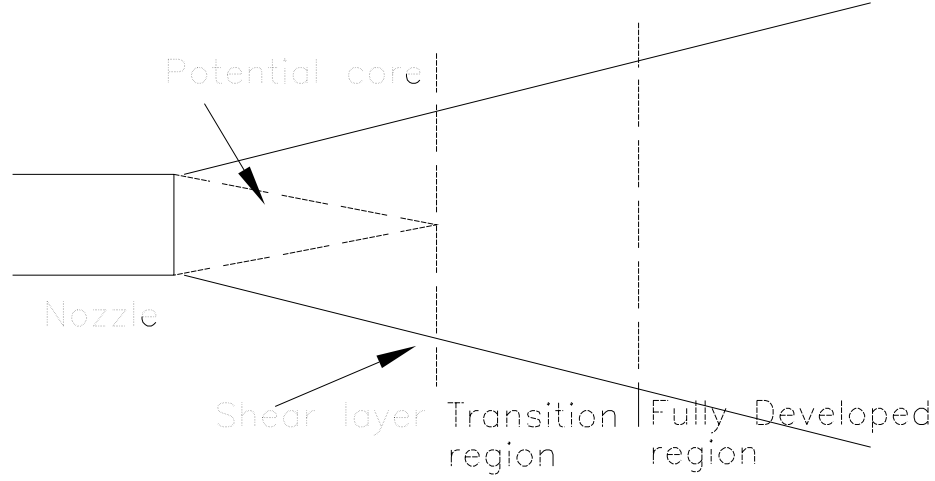
Figure 2.1: Flow zones of a free jet

region are only induced by the shear layers. Although this is not true for a jet exiting a pipe, the dynamics in the near field of a jet exiting a pipe are still dominated by the axisymmetric shear layer. The near field ends when the shear layer grows to fill the potential core causing the collapse or end of the potential core. This is a highly intermittent process and the location of the core's end is not stationary as it may appear in the figure[49]. This figure represents a time averaged view of the flow.

The second or intermediate region of the jet, after the end of the potential core, is a transition region where the flow goes from a shear layer dominated flow to a jet flow. In the final region or far field, the flow evolves in a self-similar manner where all the velocity and turbulent profiles have the same shape. The jet spreads linearly and the characteristic velocity decays as the distance increases.

The dynamics of the turbulent structures in the near field are of most interest here since the largest heat transfer in the impinging jet occurs when spacing between the jet and plate is less than approximately 6∼7 diameters. Initially, the development of the flow is dominated by the Kelvin-Helmohohz instability that causes the shear layer
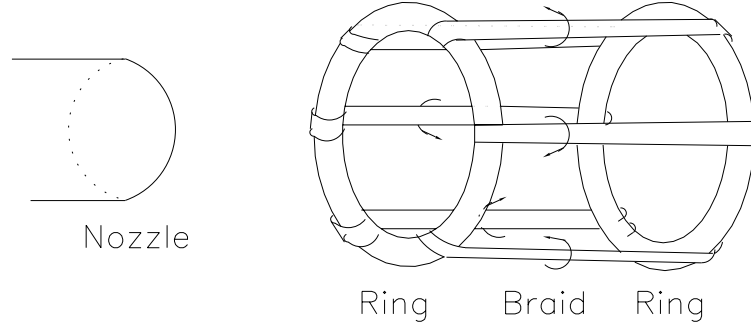
Figure 2.2: Sketch of streamwise vortices

to roll-up to form vortex rings. These structures undergo pairing[72] forming larger vortex rings. Glauser[70] showed that at a distance of $H/D \approx 3$ there are also large scale structures on the outside of the flow that are characterized by high azimuthal mode numbers.

Citriniti[74] later showed that these structure seem to be streamwise vortices located in the "braid" region between the ring structures as shown schematically in Figure 2.2. These streamwise vortices appear to play an important role in the mixing process, entraining slow moving flow from the ambient and ejecting high-speed flow from the center of the jet.

Most of the early investigations to control and enhance the mixing in round jets focused on forcing the ring mode. However, in light of the aforemention studies that showed the role of the streamwise modes, many recent efforts have focused on trying to amplify the streamwise modes[69][70]. The relative effectiveness of these two approaches is still an open question with seemingly contrary results being reported. One passive technique to enhance the higher azimuthal modes of the jet, that has not been investigated in impinging jet is adding tabs at the end of the jet. Bradbury and Khadem[63] investigated the effect of a small square tab at the exit of an axisymmetric free jet at Re=60,000. The tab produces dramatic changes in the jet development.

The contours of streamwise velocity show that the tab tends to split the jet almost in two with high velocity regions on either side of the tab. It is found that the length of the potential core is shortened by approximately two diameters and the turbulent fluctuation $(\overline{u^2})^{1/2}/U$ is increased at $2 \leq Z/D \leq 7$ downstream. Bradbury and Khadem speculate the distortion of jet by tabs might be caused by the stirring action of trailing vortex motions shed from the tabs.

The effect of a pair of delta tabs on the flow structure at small Reynolds number(Re=1950 and 4160) were studied by Reeder and Samimy[66]. It was found that a pair of counter-rotating vortices were generated by each tab, creating a low speed region behind the tab and two high speed regions at each side.

Flow Field in the Impinging Jet

The submerged impinging jet, shown in Figure 2.3, is generally broken into three regions, a initial mixing region where the jet develops, a deflection or impingement region where the jet is deflected, and the radial wall jet region where the flow decays in a self-similar manner.

The evolution of the large scale vortical structures in the impinging jet have been investigated qualitatively using flow visualizations[4][5] and quantitatively with hotwire anemometry[42], LDA anemometry[8] and particle image velocimetry[7]. A sketch of the flow visualization from this investigation is shown in Figure 2.4[5]. It is found that for small jet-to-plate spacing, particularly H/D=2, the large-scale ring vortex structures that develop in the shear layer impinge onto the plate, and spread out radially when they approach the plate, moving out a distance of approximately D/2 above the plate. The vortices induce positive radial velocity in the free stream[7] and adverse pressure gradient on the plate[42]. These ring vortices cause secondary vortices that eventually cause boundary layer separation occurs at r/D≈2. It is generally believed that this separation is responsible for the secondary peak in the local
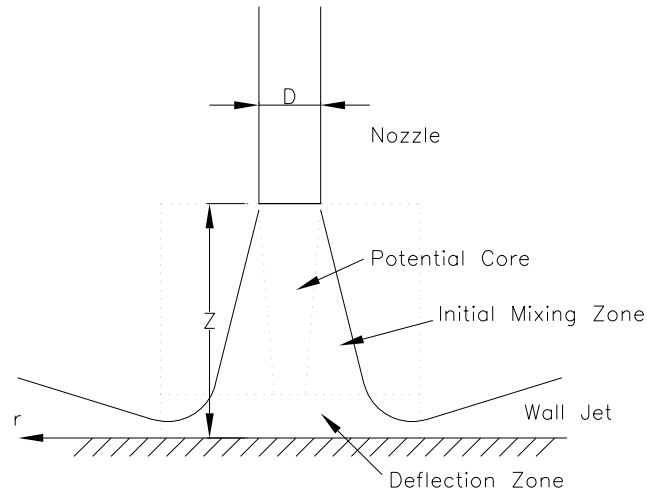
Figure 2.3: Flow zones of a impinging jet in the case of jet-to-plate spacing shorter than the length of the jet potential core
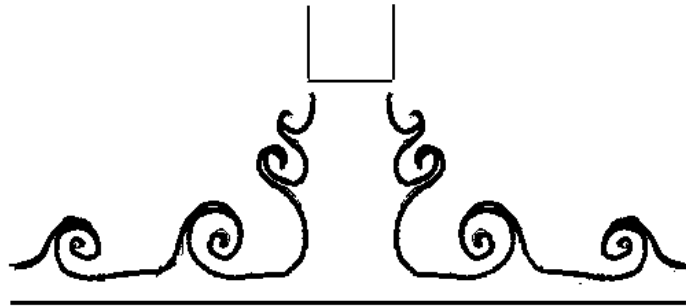
Figure 2.4: Sketch of the flow visualization of confined round impinging jet for a jet-to-plate spacing H/D=2 and Re=3,840.

heat transfer rate at this radial location. The existence of secondary vortices was first observed by Harvey and Perry[9] and was conformed by Didden & Ho[42], Walker *et al.*[4], Popiel and Trass[5], and Landreth and Adrian[7].

2.2 Heat Transfer in Impinging Jet

There have been numerous of investigations of the heat transfer produced by submerged round impinging jet. Reviews of the earlier research on this jet can be found by Martin[10], Jambunatham *et. al*[11], and Viskanta [12]. A summary of the investigations contained in these reviews and more recent investigations are provided in Table 2.1 and 2.2. Despite the seemingly large number of investigations of the round impinging jet, there are still unresolved issues about the characteristics of this flow.

Behnia *et al.*[48] and others noted that the differences in the measurements from different investigations of the same flow far exceed the reported experimental uncertainties. For example, several different measurements of the heat transfer for the impinging jet exiting a long pipe with Re=23,000 and a jet-to-plate spacing of six diameters are shown in Figure 2.7. The investigators used four different measurement techniques, Baughn and Shimizu[26] measured the heat transfer on a heated plate using Liquid Crystal Thermography, Yan [29] used preheated wall transient technique in the same facility, Lytle and Webb[37] used Infrared Thermography, and Huang and El-henk[20] used thermocouples. In all cases, the investigators reported an experimental uncertainty of $4 - 6\%$. It is clear however that the differences far exceed this experimental error. It is generally believed that the Baughn and Shimizu's measurements are, in fact, the correct measurements[71]. The significant variation in the heat transfer results has two significant effects. It reduces confidence in the measurements and makes them less useful for purposes such as validating turbulence

Investigation	Date	Nozzle Geometry	Nozzle diameter-mm	Re	Z/D	Measurement Techniques	Heat Flux	Heat Transfer Correlations
Donaldson et. al.	1971	Contoured	13	30,000~110,000	10~30	Heat flux transducer – Thermocouple differential	Preheated wall	$Nu_5/(Re_5)^{0.8} = f(r/r_5)$, Nu_5, Re_5 are based on half jet width r_5, 32,800<Re_5<111,500; 10<Z/D<30
Hoogendoorn	1977	Contoured & Long Pipe	57	66,000	2~9	Liquid Crystal Thermography	constant temperature water bath	$Nu/Re^{1/2} = 0.65 + 2.03\left(\frac{Tu\,Re^{1/2}}{100}\right) - 2.46\sqrt{\frac{Tu\,Re^{1/2}}{100}}$ $2\times10^4 \le Re \le 9\times10^4$, $9\% \le Tu \le 20\%$, $1 \le Z/D \le 10$
Goldstein and Behbahani	1982	Short pipe L/D=7 & Orifice L/D=1	12.7	35,200~121,000	6 12	Thermocouple	0.0254mm-thick S-S foil heater	
Obot et al.	1982	Contoured ASME	20	18,000~50,100	2,4,6,8	Thermocouple	Heater attached under the plate	
Hrycak	1984	Contoured, lip-equipped	3.18, 6.35, 9.52	14 000, 26 000, 54 000, 67 000	5~20	Thermocouple	0.0254mm-thick S-S foil heater	
Goldstein et al.	1986	ASME elliptical	12.7	61,000~124,000	2~10	Thermocouple	0.0254mm-thick S-S foil heater	
Kataoka et al.	1987	Contoured	28	7,000~50,000	2~10	Thermocouple	0.05mm-thick Fe-Ni alloy foil heater	
Goldstein and Franchett	1988	Orifice L/D=1	10	10,000~30,000	4, 6, 10	Liquid Crystal Thermography	0.025mm-thick S-S foil heater	
Baughn and Shimizu	1989	Long pipe L/D=72	25	23,750	2~14	Liquid Crystal Thermography	Thin gold coating heater	
Goldstein et al.	1990	ASME elliptical	12.7	61,000~124,000	2~12	Thermocouple	0.0254mm-thick S-S foil heater	
Stevens & Webb	1991	Long pipe L/D=50,43	2.2, 4.1, 5.8, 8.1	4,000~52,000	2.2~8.9	Thermocouple	0.0508mm-thick S-S foil heater	$Nu_o = 2.67\,Re^{0.567}\,Pr^{0.4}(Z/D)^{-0.0336}(U_e/D)^{-0.237}$ or $Nu_o = 1.51\,Re^{0.44}\,Pr^{0.4}(Z/D)^{-0.11}$
Baughn et al.	1991	Long pipe L/D=72	25	23,300~55,000	2~10	Liquid Crystal Thermography	Thin gold coating heater	
Pan et al.	1992	Long pipe, contoured orifice, sharp edged orifice with and without screens	10.9	16,500<Re<43,500	1	Infrared Thermography	0.0254mm-thick S-S foil heater	$Nu_o = 0.50\,Re^{0.53}\,G^{0.58}\,Pr^{0.4}$, G is the mean redial velocity gradient, $G = d(u/U)/d(r/d)$
Yan et al.	1992	Long pipe L/D=64	52	23 000, 50 000, 70 000	2, 4, 6, 10	Liquid Crystal Differential Measurement	Preheated Wall	
Mohanty and Tawfek	1993	Contoured	3, 5, 7	6,900~34,500	6.5~58	Heat flux transducer – Thermocouple differential	Preheated wall	D=3mm, Re=4860~15300, Z/D=10~17: $Nu_o = 0.15\,Re^{0.701}(Z/D)^{-0.25}$ Z/D=20~25: $Nu_o = 0.17\,Re^{0.701}(Z/D)^{0.182}$
Hansen and Webb	1993	Long pipe L/D=94, 68	6.91, 13.3	4,700~24,000 8,100~33,000	1~14	Thermocouple	Heater Module under plate	
Womac et al.	1993	Orifice L/D=18, 11, 5.8 and 2.75	0.978, 1.65, 3.11, 6.55	600~54,000	3,4	Thermocouple	Square heat source attached under plate	$\overline{Nu}_L/Pr^{0.4} = 0.516\,Re_{di}^{0.5}\frac{l}{d_i}A_r + 0.49\,lRe_L^{0.532}\frac{l}{L}(1-A_r)$ $d_i = (U_e/U_i)^{0.5}/D$, $L = (r-D)/2$, $A_r = \pi d_i^2/(4l^2)$ l is the size of heat source
Azavedo et al.	1994	Long Pipe L/D=131	6.1	5,200~24,300	6	Infrared thermography	0.051mm-thick S-S foil heater	

Figure 2.5: Summary of investigations on impinging round jet heat transfer

Investigation	Date	Nozzle Geometry	Nozzle diameter-mm	Re	Z/D	Measurement Techniques	Heat Flux	Heat Transfer Correlations
Huber and Viskanta	1994	Square-edged orifice array L/D=1.5	6.35	3,500~20,400	0.25, 1, 6	Liquid Crystal Thermography	0.025mm-thick S-S foil heater	$\overline{Nu} = 0.5 KG \mathrm{Re}^{0.667} \mathrm{Pr}^{0.42}$, $K = \left\{ 1 + \left[\frac{(Z/D)\sqrt{A_f}}{0.6} \right]^{-0.05} \right\}$, $G = 2\sqrt{A_f} \frac{1 - 2.2\sqrt{A_f}}{1 + 0.2(Z/D - 6)\sqrt{A_f}}$, $A_f = (\pi D)(D/X_n)^2$; Re=2000~100,000; A_f=0.004~0.04; Z/D=2~12. X_n is the spacing between jets.
Huang & El-Geng	1994	Long pipe L/D=25.8	6.2	5,927~58,575	1,2,6,10	Thermocouples	0.0508mm-thick S-S foil heater	$\overline{Nu} = \mathrm{Re}^{0.76} \mathrm{Pr}^{0.42} \left\{ a + b \left(\frac{Z}{D} \right) + c \left(\frac{Z}{D} \right)^2 \right\}$; $5927 < \mathrm{Re} < 58575$; a, b, c are polynomial functions of r/D
Lytle and Webb	1994	Long pipe L/D=78,56	7.8, 10.9	3,600~27,600	0.1~1, 6	Infrared thermography	0.051mm-thick S-S foil heater	Re=3700~30000,0.1<Z/D<1 $Nu_o = 0.726 \mathrm{Re}^{0.53} (Z/D)^{-0.191}$ r/D=1: $\overline{Nu} = 0.424 \mathrm{Re}^{0.57} (Z/D)^{-0.33}$ r/D=2: $\overline{Nu} = 0.150 \mathrm{Re}^{0.67} (Z/D)^{-0.36}$
Lee et al.	1994	Long pipe L/D=55 elliptic orifice outlet	D_e=8.8	5 000, 10 000, 20 000	2~10	Liquid Crystal Thermography	Thin gold coating heat	
Meola et al.	1995	Truncate Cone Gardon Nozzle ASME Nozzle	5 5 10	90,000~163,000	1~12	Infrared thermography	0.04mm-thick S-S foil heater	
Lee et al.	1995	Long pipe L/D=55	17.8	4,000~14,400	2, 4, 6, 10	Liquid Crystal Thermography	Thin gold coating heat	
Garimella and Rice	1995	Square-edged orifice L/D=0.25~12	0.79, 1.59, 3.18, 6.35	4,000~23,000	1~14	Thermocouple	0.075mm-thick S-S foil heater	Z/D=1~5: $Nu_o = 0.492 \mathrm{Re}^{0.585} \mathrm{Pr}^{0.4} (Z/D)^{0.024} (L/D)^{0.09}$ $\overline{Nu} = 0.160 \mathrm{Re}^{0.695} \mathrm{Pr}^{0.4} (Z/D)^{-0.11} (L/D)^{-0.11}$ Z/D=6~14: $Nu_o = 0.513 \mathrm{Re}^{0.694} \mathrm{Pr}^{0.4} (Z/D)^{-0.256} (L/D)^{-0.04}$ $\overline{Nu} = 0.164 \mathrm{Re}^{0.775} \mathrm{Pr}^{0.4} (Z/D)^{-0.52} (L/D)^{-0.05}$
Liu and Sullivan	1996	Contoured	12.7	12,270~15,100	1~11	Temperature sensitive fluorescent paint	0.0254mm-thick S-S foil heater	
Colucci and Viskanta	1996	Contoured L/D=1.5 Orifice L/D=1.5	12.7	10,000~50,000	0.125~6	Liquid Crystal Thermography	0.025mm-thick S-S foil heater	
Meola et al.	1996	Truncate Cone L/D=16.7, 10, 10	3, 5, 10	10,000~173,000	2~100	Infrared thermography	0.05mm-thick Cn foil heater	$\overline{Nu} = 0.548 \mathrm{Re}^{0.65} (Z/D)^{-0.714}$, 10,000<Re<100,000; r/D=6, Z/D>10
Seyel-Yagoobi et al.	1998	Short pipe L/D=5.7 & Radial reattachment jet	27	24,300~57,200	0.5~6	Infrared Thermography	0.0254mm-thick Inconel foil heater	
Huang & El-Geng	1998	Long pipe L/D=25.8	6.2	5,927~58,575	1~10	Thermocouples	0.0508mm-thick S-S foil heater	
Haneda et al.	1998	Contoured	15	9,100~10,400	3	Thermocouples	0.02mm-thick S-S foil heater	
Ma et al.	1998	Long pipe L/D=35.5 Orifice	0.987, 3	162~958	4	Thermocouple	0.010mm-thick Constantan foil	$Nu_o = 1.11 \mathrm{Re}^{0.503} \mathrm{Pr}^{1/3}$ at Z/D=4, 162<Re<958
Garrett and Webb	1999	Orifice Array L/D=6	1.6	1100~2500	1~14	Infrared thermography	0.0254mm-thick S-S foil heater	
Sailor et al.	1999	Pipe with pulsation valve L/D=3.64	14	21,000~31,000	4, 6, 8	Thermocouple	Heat module attached under plate	
Brignoni and Garimella	2000	Square-edged orifice L/D=1 with and without chamfer inlet	3.18	5,000~25,000	1, 4	Thermocouple	0.0762mm-thick S-S foil heater	

Figure 2.6: Summary of investigations on impinging round jet heat transfer
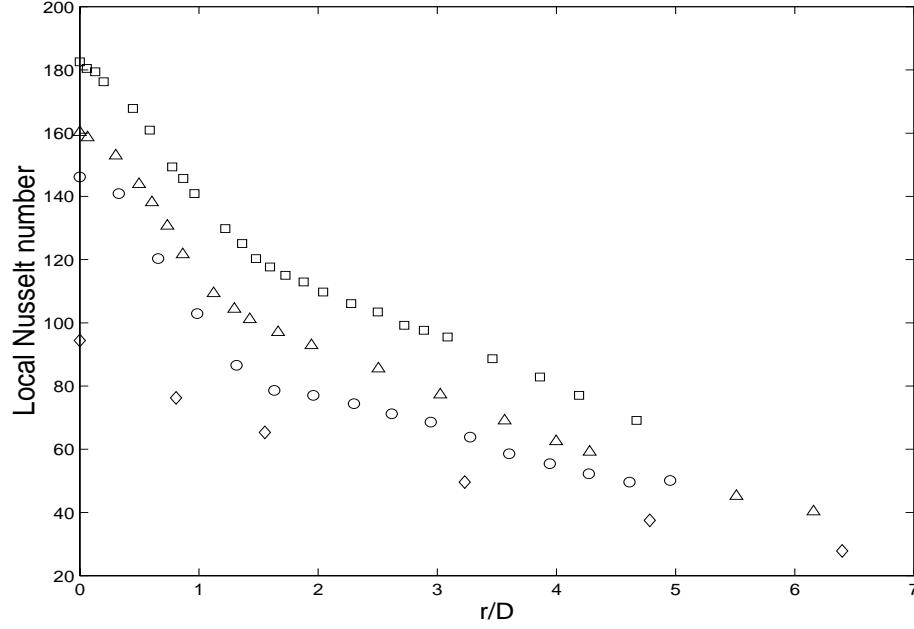
Figure 2.7: Local Nusselt number distribution for H/D=6 for Re_o=23,300 from different experiments using long pipe nozzle, □ Lytle and Webb[37], △ Baughn and Shimizu[26], ◯ Yan *et al.*[29], ◇ Huang and El-henk[20], Re=20,000, rescaled by $(Re_o/Re)^{0.7}$.

models. It also makes it difficult to compare the heat transfer measured for different cases or heat transfer enhancement schemes unless the investigations include a common experiment. The differences in these measurements seem to be the result of the differences in experimental techniques. Thus, it is useful to briefly review the experiment methods and their potential errors before proceeding to discuss the measurements.

2.3   Experimental Methodologies

There are two different approaches used to measure the heat transfer produced by the impinging jet; the differential approach and the direct approach. In the differential approach, the impingement plate is initially heated to a given temperature at which

point the heat source is removed. The surface is then cooled by the impinging jet and the heat transfer from the surface is determined by measuring the change in the plate temperature (or energy stored in the plate). In the direct approach, the surface is heated by uniform external heat source or a thin uniform foil. A constant current is passed through the foil during the experiment so the heat flux at any point in the surface is simply due to the Joulean heating. The latter is the most common technique.

A key assumption in both these approaches is that all the energy removed from the plate is caused by the forced convection from the impinging jet. Actually, the energy transfer by radiation can be easily computed and removed from the total heat flux. Heat transfer by conduction inside the impingement surface or to the surroundings is more difficult to determine and thus should be minimized. Generally, the impingement surfaces used in the differential approach are thicker than those in the direct approach and there are greater errors caused by conduction in the surfaces. Often greater care has been taken in the thin foil experiments to minimize conduction from the surface to the neighboring components, though the level of care does depend on experiments. Thus, the thin foil approach is used more commonly in the recent experiments.

Thermocouple [13]∼[22], liquid crystal [24]∼[33] or infrared camera [34]∼[41] are three major transducers used to measure the surface temperature in impinging jet experiment. The thermocouple is one of the most widely used temperature transducers, particularly in earlier investigations, because it is both inexpensive and relatively accurate. The spatial resolution of thermocouple method is poor. Using thermocouples on a thin foil will cause the local temperature to change, so the accuracy will be significantly lowered. Thermochromic Liquid Crystal exhibits visible colors related to the temperature and can measure the temperature with an accuracy of 0.25^oC[26]. Liquid crystal is commercially available in sheets and micro-encapsulation spray that

can be easily mounted. They add little to the thermal resistance of the heat transfer surface and have negligible heat capacity. The liquid crystal can be challenging to calibrate and they are only sensitive over a limited temperature range. Poor calibration of the liquid crystals or using them out of the range can lead to errors. Infrared thermography is a temperature mapping techniques that detects the energy radiated in the infrared spectral band from the object being measured. This method provides a spatial resolution up to $0.02''$/pixel claimed by the manufacturer. The calibration of the thermal camera only requires the specification of the surface emissivity. This can be difficult to determine for some surfaces, particularly materials composed of multiple components, but it is relatively straight forward in impinging jet measurements where the surface can be painted a uniform candle-soot black. The thermal camera likely provides the most accurate measurements if properly used but it is also by far the most expensive approach so that many investigations rely on liquid crystal.

2.4   Discussion of Previous Measurement Results

A second difficulty with the existing measurements is that many have used different nozzle geometries, such as long-pipe nozzle, square edge orifices, and a wide variety of contoured orifice nozzles. Few studies consider the same nozzles examined elsewhere or make any attempt to document the velocity exiting the nozzle. This approach, combined with the large uncertainty in the measurements, makes it challenging to develop parametric relationships for the change in Nusselt number with jet-to-plate spacing, Reynolds number, or the presence of a confining wall.

Recently, however, there have been a number of investigations of impinging jets formed by a flow exiting a fully developed pipe[20][26][29][37]. The advantage of using the flow from a long pipe is that it ensures the exit conditions of the jets in the different experiments are all the same. Thus, the heat transfer measurements from the

different studies can be compared to assess the accuracy of the different results, and once it is determined they are accurate, they can be used to develop more extensive parametric studies. The results for this case are discussed initially before proceeding to discuss the remaining results.

2.4.1   Heat Transfer from a Jet Exiting from a Fully Developed Pipe Flow

The heat transfer for an unconfined impinging jet for a variety of jet-to-plate distance, ranging from H/D=0.15 to H/D=14, measured by Lytle and Webb[37] and Baughn and Shimizu[26] are shown in Figure 2.8. It is clear that the heat transfer for the unconfined jet is the largest when the jet-to-plate spacing is the smallest. At H/D=0.15, the maximum local heat transfer occurs at an off-axis peak. As the spacing increases the off-axis peak decreases until at a jet-to-plate spacing of 0.25 diameters the largest heat transfer occurs at the stagnation point. There is still a secondary maximum at r/D≈2 that decreases until it is no longer seen for H/D=6. The stagnation heat transfer continually decreased from H/D≈0.15 to H/D≈2 but it begins to increase again and eventually peaks at H/D≈6.

Lytle and Webb[37] argued that the large heat transfer rate near the center of the jet for close spacing, H/D<0.25, is caused by the fact that the flow must be turned rapidly and accelerated through the gap between the pipe exit and the plate. For larger impingement distances the height of the jet after the acceleration region is approximately 0.25D. Thus, for jet-to-plate spacing smaller than H/D=0.25 the jet must pass through a smaller area and so that flow through the region is faster than in the normal wall jet case and the heat transfer is increased. There have been a number of investigations of the cause of the off axis peak[5][7]. As discussed in a previous section on the flow field, this peak is caused by the separation of the large-scale ring
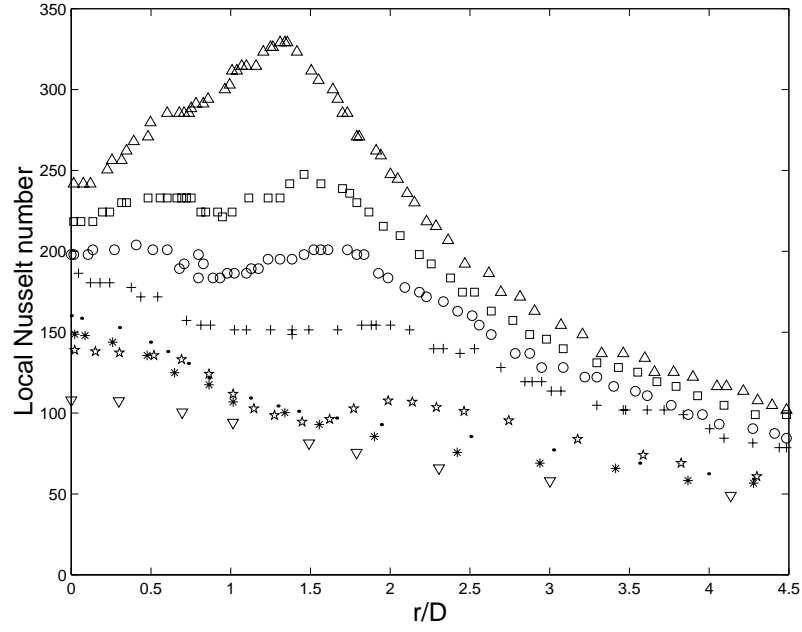
Figure 2.8: Local Nusselt number distributions for Re=23000[37][26] at △ H/D=0.15, □ 0.2, ◯ 0.25, + 0.5, ★ 2, ● 6, ∗ 10, and ▽ 14.
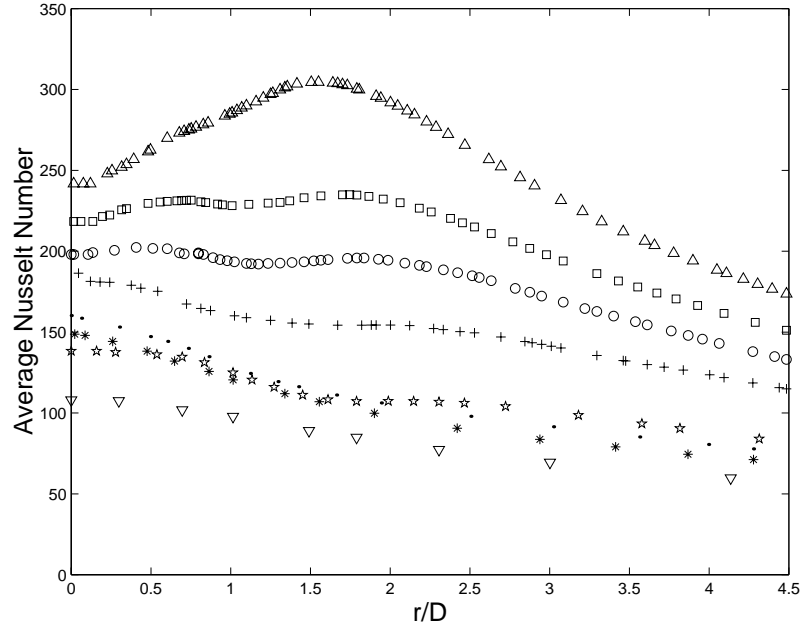
Figure 2.9: Average Nusselt number distributions for Re=23000[37][26] at △ H/D=0.15, □ 0.2, ◯ 0.25, + 0.5, ★ 2, ● 6, ∗ 10, and ▽ 14.

vortices in the flow from the wall.

The increase in the stagnation Nusselt number from H/D=2 to 6 is caused by an increase in the turbulence intensity at the centerline as the shear layers in the jet develop[26][43]. The peak at H/D=6 corresponds to the end of the potential core where the turbulence intensity at the centerline is nearly a maximum due to the intermittency associated with the collapse of the potential core. The centerline velocity and the turbulence intensity of the jet decays after this point causing a decrease in the stagnation Nusselt number as seen from H/D=6 to 14.

It should be noted that the local Nusselt number can be a deceptive measure of the heat transfer from the plate because the flow is axisymmetric. It is useful to look at the average Nusselt number $\overline{Nu}$ given by

$$\overline{Nu} = \frac{2}{R^2} \int_0^R Nu \cdot r \cdot dr = \frac{q_{conv}D}{k_a(\overline{T_w} - T_j)}, \tag{2.1}$$

where the average wall temperature in the area πR^2 is given by

$$\overline{T_w} = \frac{2}{R^2} \int_0^R T_w \cdot r \cdot dr. \tag{2.2}$$

Thus, the average Nusselt number at any radius is a measure of the heat transfer occurring on the circular region inside the radius for a constant temperature wall or inversely related to the local wall temperature for the constant heat flux case.

The average Nusselt number distributions for different jet-to-plate spacings at Re=23,000 are shown in Figure 2.9. It is evident that the impinging jets with small jet-to-plate spacing yield an average Nusselt number that is approximately equal to the stagnation Nusselt number over the region r/D≤3, which is of interest in many practical applications. For larger separation distance H/D>2, the average Nusselt number decreases significantly from r/D=0∼3 indicating the stagnation heat transfer often reported is not a good measure of the heat transfer over this area. In particular, the average Nusselt number at r/D=3 for H/D=2 is actually larger than that for

H/D=6, so that the former provides far more heat transfer over larger areas despite the larger stagnation heat transfer for H/D=6.

One of the important factors in characterizing the heat transfer of the impinging jet is the relationship between the Nusselt number and Reynolds number of the jet that allows the results for a single Reynolds number to be scaled to different numbers. Goldstein and Franchett[25] proposed a correlation between Nusselt number and Reynolds number given by

$$Nu = Ae^{B(r/D)^C}Re^{0.7} \qquad\qquad (2.3)$$

where A, B, C are parameters that are a function of jet-to-plate spacing $4 \leq H/D \leq 10$. Goldstein and Franchett obtained this correlation using data with Reynolds number varying from 10,000 to 30,000 and jet-to-plate spacing ranging from 4D to 10D.

The heat transfer for several different Reynolds number was measured by Lytle and Webb[37]. The local Nusselt number at three different Reynolds number is shown in Figure 2.10. The Nusselt number increases with Reynolds number as expected since the Reynolds number has been increased by increasing the mass flow rate of the jet. The ratio of $Nu/Re^{0.7}$ for the local heat transfer for three different Reynolds numbers is shown in Figure 2.11. The magnitude of the ratios are in reasonable agreement suggesting the correlation predicts the change in the overall heat transfer reasonably well. There are differences in the curves, however, indicating this simple correlation does not include all the information. Lytle and Webb[37] proposed a correlation for averaged Nusselt number at r/D=1 and 2 for $0.1 \leq H/D \leq 1.0$ and $3,600 \leq Re \leq 27,600$, given by

$$\overline{Nu}_{r/D=1} = 0.424Re^{0.57}(H/D)^{-0.33}, \qquad\qquad (2.4)$$

$$\overline{Nu}_{r/D=2} = 0.150Re^{0.67}(H/D)^{-0.36}. \qquad\qquad (2.5)$$

Lytle and Webb[37] also noted that the location of the secondary peak for near impingement cases moved and found that the location of the peak could be approximated by

$$(r/D)_{sec.peak} = 0.188 Re^{0.241}(H/D)^{0.224}. \tag{2.6}$$

for their data with Reynolds number ranging from 11,000< Re <27,600 at 0.1< H/D <4.

Most investigations of the impinging jet were performed for cases where the jet and the ambient air were at the same temperature. When there is temperature difference between the jet and the ambient fluids, entrainment will change the jet temperature and affect the heat transfer from the plate. Baughn et al.[27] proposed that the heat transfer from these jets could be predicted using the heat transfer coefficient computed using the adiabatic wall temperature; i.e.,

$$h = \frac{q_{conv}}{T_w - T_{aw}} \tag{2.7}$$

as is done for compressible impinging jets. Baughn et al.[27] performed measurements in three jets and characterized the variation in temperatures using a non-dimensional jet temperature, T_j^*, given by

$$T_j^* = \frac{T_j^0 - T_\infty}{T_{w0} - T_{aw0}}, \tag{2.8}$$

where T_j^0 is the total temperature of the jet, T_∞ is the ambient air temperature, T_{w0} is the wall temperature at stagnation point, and T_{aw0} is the adiabatic wall temperature at the stagnation point. The Nusselt number distributions for the three jets with T_j^*=0, 0.33, and 1.0 are shown in figure 2.12. There is reasonable agreement between the computed Nusselt numbers indicating that this method is an effective technique for determining the heat transfer coefficient. It should be noted, however, that the adiabatic wall temperature is not easily determined because it would depend on the mixing between the hot jet and the ambient fluid.
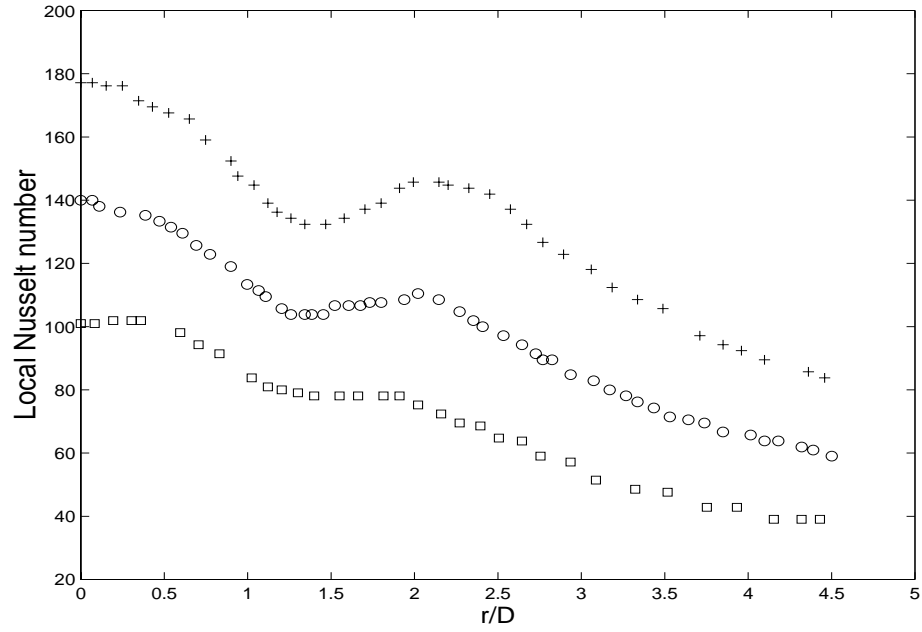
Figure 2.10: Radial variation in Nusselt number for nozzle-plate spacing H/D=1[37] and + Re=27,600, ◯ Re=18,400, □ Re=11,000.
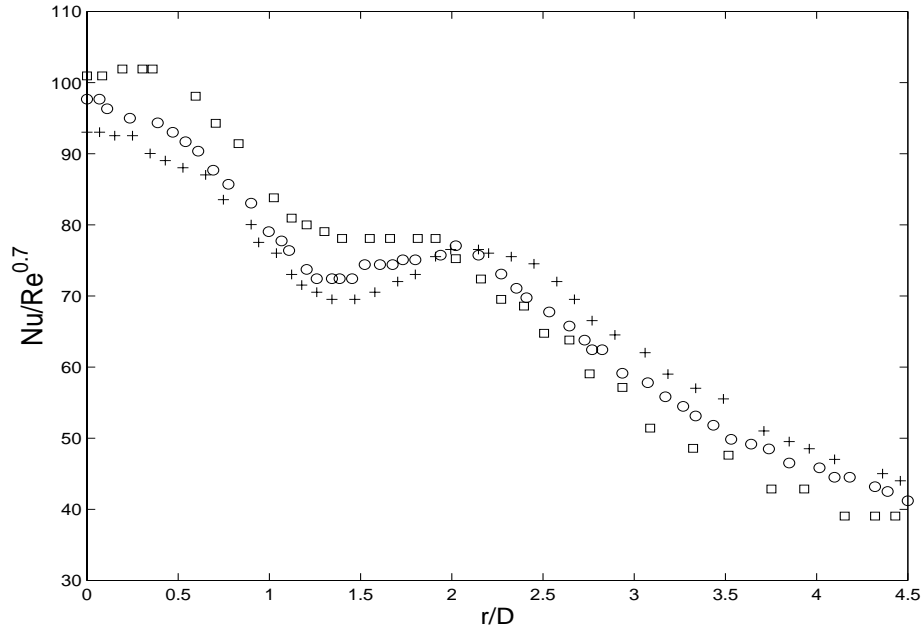
Figure 2.11: Radial variation in Nusselt number for nozzle-plate spacing H/D=1[37], Re_o=11000, + Re=27600, rescaled by $(Re_o/Re)^{0.7}$, ◯ Re=18400, rescaled by $(Re_o/Re)^{0.7}$, □ Re=11000.
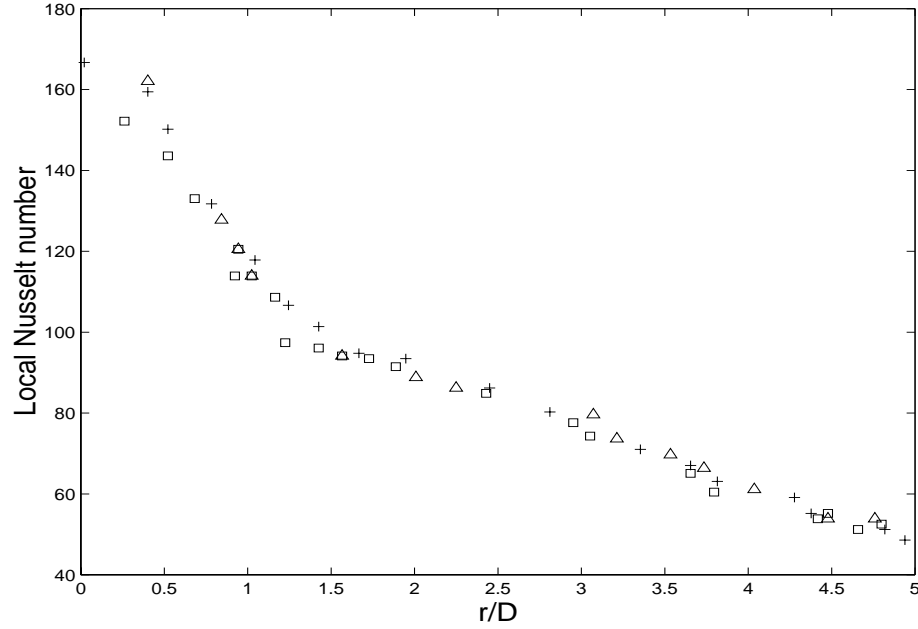
Figure 2.12: Local Nusselt number distribution for H/D=6 and Re=23,300 at different jet temperature[27], $\triangle$ T_j^*=1.0, + T_j^*=0.33, $\square$ T_j^*=0.0.

2.4.2   Heat Transfer for Jets Exiting from Nozzles or Orifices

There have been numerous investigations of the heat transfer produced by imping-ing jets from other nozzles and orifices. For example, a comparison of the Nusselt number distributions for H/D=6 produced by an elliptical nozzle[30], an orifice with a contoured inlet[32] with the results for the long pipe at Re=20,000 is shown in Figure 2.14. The sketch of the geometries of these nozzles are shown in Figure 2.13. It should be noted the Reynolds numbers used in these investigations were not all the same. Following Behnia et al.[48], the results from the Reynolds numbers other than 20,000 have been rescaled using the correlation Nu$\propto Re^{0.7}$. The orifice with the contoured inlet also had a confining plate. However, as will discussed later, measure-ments performed in this investigation and previously have shown confinement has little or no effect on the heat transfer in this region when H/D=6. The heat transfer coefficient on both the major and minor axis of the elliptical nozzle is higher than

the long pipe data within the region r/D≤3 suggesting that the elliptic jet has larger entrainment and mixing. Lee et al.[30] noted that the heat transfer measurements indicate there is a larger spreading rate on minor axis than the major axis. They suggested that this was caused by axis switching of the elliptical jet as the flow evolves downstream. This axis switching has been observed previously in free elliptical jets by Ho and Gutmark[62]. The Nusselt number distribution for the orifice is nearly identical to the results for the long pipe.

A comparison of the Nusselt number distributions for H/D=6 produced by the orifice with contoured inlet and nozzles with contoured outlets[32] at Re=50,000 and 30,000 are shown in Figure 2.16. The geometries of these nozzle are shown in Figure 2.15. The Nusselt number distributions for nozzles A and B shown in Figure 2.16 are nearly identical over the range r/D≤4.5, and both are larger than that for the orifice in the region r/D≤3. This is likely caused by the enhanced entrainment in the near fields of the jets from the contoured outlet nozzles that promote the mixing with the free stream.

Colucci and Viskanta[32] also examined the heat transfer for the orifice and two contoured nozzles when the jet-to-plate spacing was one diameter. In this case, the confinement causes a strong recirculation and has a significant effect on the heat transfer. The Nusselt number distribution for these three nozzles are shown in Figure 2.17. The Nusselt number distribution produced by the jet from nozzle B is larger than the Nusselt number from nozzle A in the region r/D≤4 and both of them are larger than the heat transfer produced by the jet exiting the orifice. The Nusselt number distribution from the three outlet are nearly identical for r/D>4, indicating the effect of nozzle geometry becomes less important in this region.

There have also been investigations on a number of other different nozzles. These include an ASME nozzle[18], long pipe nozzle with contoured outlet[24], contoured

(a)   **(b)**
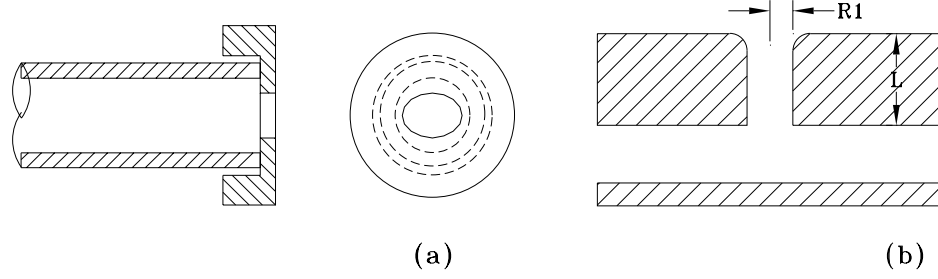
Figure 2.13: (a) Sketch of Lee *et. al*'s[31] nozzle, elliptic orifice aspect ratio=2.14, equivalent diameter D_e=8.8mm, pipe diameter D=17.8mm, L/D=55. (b) Sketch of Colucci and Viskanta's orifice, R_1=0.635cm, $L/R_1 = 3$.
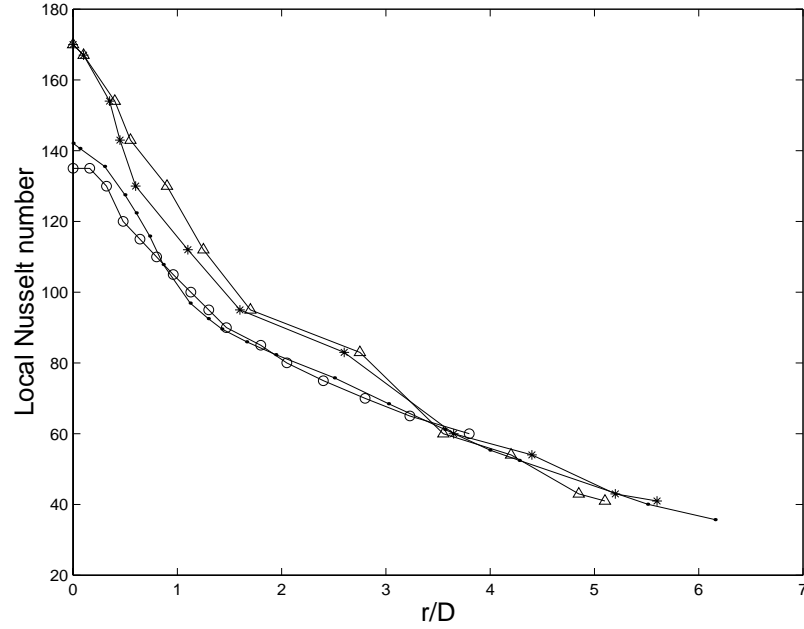
Figure 2.14: Nusselt number distribution for Re_o=20,000 and H/D=6 for different types of nozzles: $\triangle$ elliptical orifice at the exit of long pipe nozzle, major axis[30], Re=20000; $*$ elliptical orifice at the exit of long pipe nozzle, minor axis[30], Re=20000, $\bigcirc$ contoured inlet orifice[32], Re=20000, $-$ long pipe nozzle[26], Re=23750, rescaled by $(Re_o/Re)^{0.7}$.
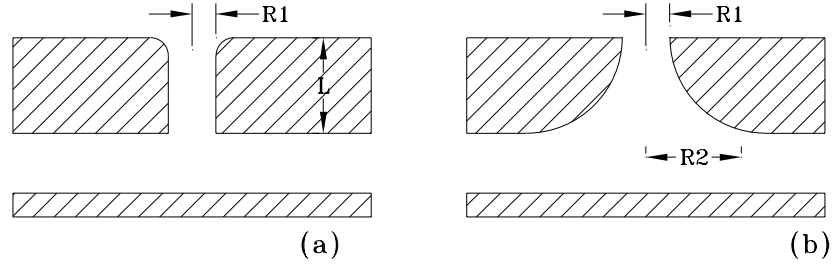
Figure 2.15: Cross section of the orifice investigated by Colucci and Viskanta[32] (a) orifice exit R_1=0.635cm (b) nozzles A and B, for nozzle A, R_1=0.635cm, R_2=1.91cm, for nozzle B, R_1=0.635cm, R_2=2.54cm, L/R_1=3.
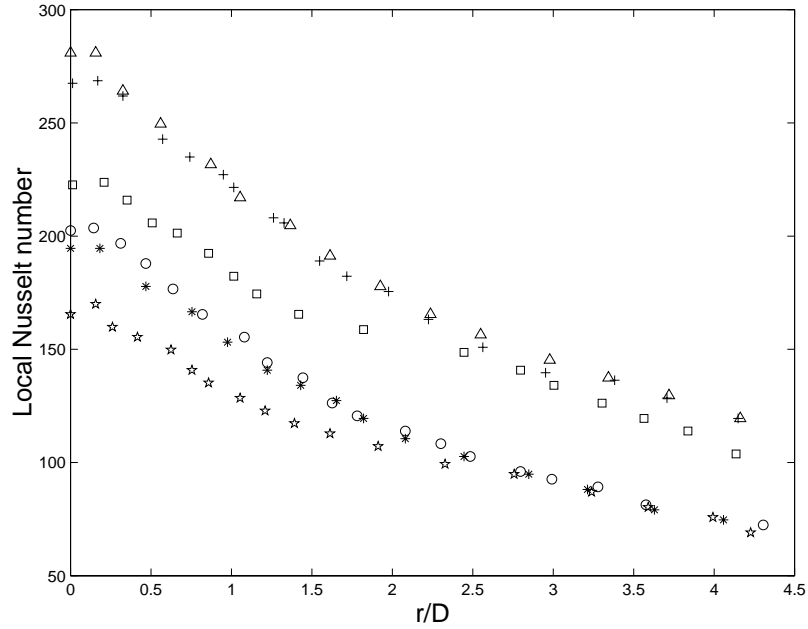
Figure 2.16: Comparison of Nusselt number distribution for nozzle A, B and the orifice at H/D=6 and Re=50000, □ orifice, △ nozzle A, + nozzle B, and Re=30000, ⋆ orifice, ∗ nozzle A, ○ nozzle B. Colucci and Viskanta[32].
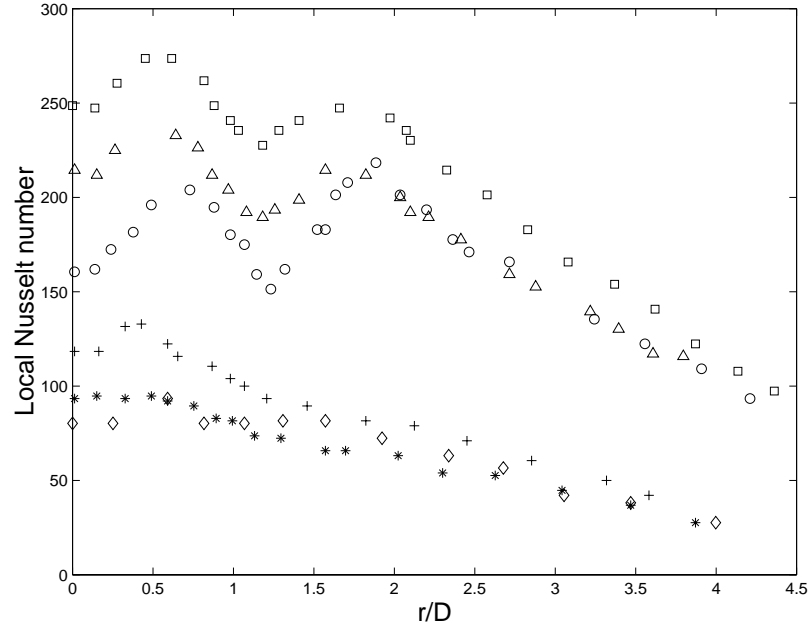
Figure 2.17: Comparison of Nusselt Number distribution for nozzle A, B and the orifice at H/D=1 and Re=50000: ◯ orifice, △ nozzle A, □ nozzle B, and Re=10000, ◇ orifice, ∗ nozzle A, + nozzle B. Colucci and Viskanta[32].

outlet from settling chamber[49], convergent radial re-attachment nozzle[41] and truncated cone[39]. The results of these experiments have many of the same features as the long pipe nozzle and the orifices though there are differences in the magnitude of the heat transfer. The experimental error observed for the long pipe data makes it difficult to assess the relative heat transfer enhancement for the different nozzles. This would be easier if the results (or the experimental procedures) were bench-marked against a common flow, such as the unconfined jet from a long-pipe.

2.4.3   Heat Transfer in Arrays of Jets

Huber and Viskanta[33] measured the heat transfer rate for an array of orifices with the geometry investigated by Colucci and Viskanta[32]. A comparison of the Nusselt number from a single jet in the jet array with the results of Colucci and Viskanta are

shown in Figure 2.18. It is clear that the Nusselt number for the jet in the array is about 10% smaller than that for the single jet in the wall jet region r/D$\geq$1.3 indicating that the interference of the jets in the array reduces the heat transfer rate.
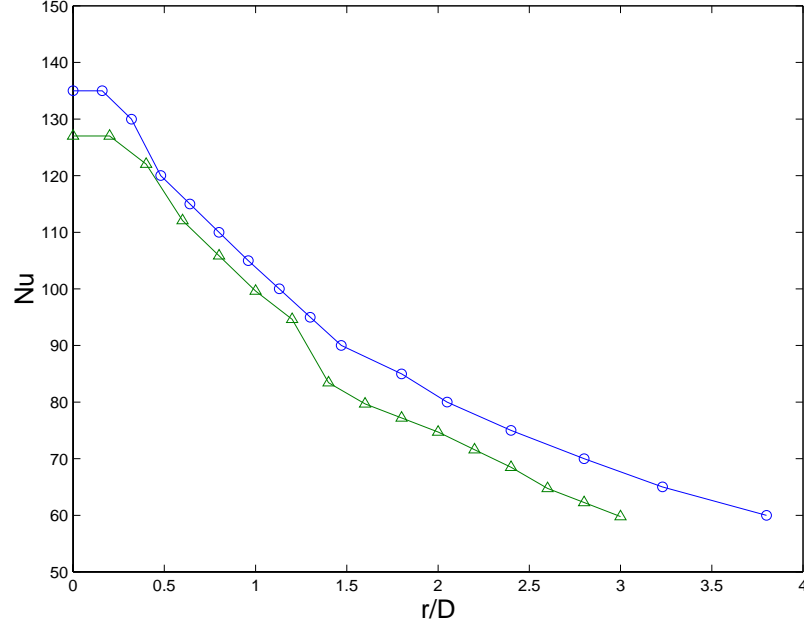
Figure 2.18: Nusselt number distribution for Re_o=20,000 and H/D=6 for ◯ a single orifice[32], Re=20000. △ a orifice in a orifice array[33], Re=17100, rescaled by $(Re_o/Re)^{0.7}$.

2.5 Heat Transfer Enhancement Techniques

In many engineering applications it is desirable to enhance the heat transfer produced by the impinging jet. This can be enhanced using either passive techniques, such as changing the nozzle geometry; adding turbulence promoters on the impingement surface; or by actively modifying the flow at the jet exit. A summary of the investigations that have attempted to enhance the heat transfer are included in Table 2.3. The details of these techniques will be discussed in the following sections. Investigations of the heat transfer enhancement in the slot or 2-D jets have been included

for completeness because many of the strategies that are effective for this flow can also be implemented in the round jet. Investigations which examined relatively simple changes to the jet geometry were discussed previously and will not be discussed again. In considering these approaches, it is useful to consider the strategies that modify the impingement surface separately from those that involve modifications to the jet exit because the former strategies can not be implemented in all applications.

2.5.1 Enhancing the Jet Turbulence

It has long been recognized that the heat transfer caused by a flow impinging on surface can be increased by increasing the turbulence intensity of the flow. For example, Kestin and Wood[53] found the heat transfer at the stagnation point of a cylinder in cross flow was approximately given by

$$\frac{Nu}{Re^{1/2}} = 0.945 + a\left(\frac{TuRe^{1/2}}{100}\right) - b\left(\frac{TuRe^{1/2}}{100}\right)^2, \tag{2.9}$$

where a=3.48 and b=3.99 for $75000 < Re < 125000$, Tu is the ratio of the size of the turbulent fluctuation velocity u' and the mean velocity U, given by

$$Tu = u'/U. \tag{2.10}$$

In one of the earliest attempts to enhance the heat transfer in impinging jets, Gardon and Akfirat[43] mounted a mesh screen slightly upstream from the exit of a plane impinging jet. They found that in the near field (H/D≤3) the turbulence intensity of the flow was increased by 2.5 to 18 percent and there was a corresponding enhancement in the stagnation heat transfer rate for H/D≤5, as shown in Figure 2.20. Hoogendoorn[24]later increased free stream turbulence level in a round jet to approximately 5% using wire grids at the exit of the contoured round nozzle. Using these heat transfer measurements, Hoogendoorn proposed that the effect of the turbulence

Enhancing Techniques	Modification	Investigation	Date	Nozzle Geometry	Re	Z/D	Enhancement Result
Changing Nozzle Orientation	Impingement angel=30,45,60,90°	Goldstein and Franchett	1988	Orifice L/D=1	10,000~30,000	4, 6, 10	Impingement angle θ=60° has the maximum stagnation heat transfer rate at Z/D=6, Re=20000, the correlation for local Nusselt number $Nu/Re^{0.7} = A\exp\{-(B + C\cos\theta)(r/D)^m\}$
	Impingement angel=-40°~90°	Beitelmal et al.	2000	Slot Jet	4,000~12000	4~12	Impingement angle θ=60° has the maximum stagnation heat transfer rate at Z/D=6, Re=7900, θ=90° has the max. Nu at Z/D=10, Re=12,000
Nozzle Modification	Contouring the Orifice Outlet	*Colucci and Viskanta	1996	Contoured nozzle with different outlet & Orifice L/D=1.5	10,000~50,000	0.125 ~6	At r/D<3, both nozzle has higher Nu than the orifice at Z/D=6, Re=30000 ~50000. Nu from nozzle with bigger outlet is higher than the other, both are higher than that of the orifice at Z/D=1, Re=50000
	Chamfering Orifice Inlet	Brignoni and Garimella	2000	1 square-edged orifice L/D=1 with and 2 orifices with chamfered inlet	5,000~25,000	1, 4	At Re=20000, Z/D=1, r/D<2, Nu from wide chamfered orifice is higher than square edged, both are higher than the narrow chamfered one, at Z/D=4, r/D<3, wide chamfered and square-edged are similar, both higher than narrow chamfered
	Elliptical orifice at nozzle exit	*Lee et al.	1994	Long pipe L/D=55 with an elliptical orifice outlet	5 000, 10 000, 20 000	2~10	At Re=20000, Z/D=6, r/D<2, Nu are higher than long pipe data in both major and minor axis. The enhancement could reach 20% at the stagnation point.
	Radial Reattachment Jet	Seyed-Yagoobi et al.	1998	Short pipe L/D=5.7 & Radial reattachment jet	24,300~57,200	0.5~6	30% enhancement in Nu occurs at r/D=2~4, heat transfer rate deteriorate at all other location, the stagnation heat transfer rate is only 40% of long pipe nozzle.
	Swirling jet	Huang & El-Geng	1998	Long pipe L/D=25.8	5,927~58,575	1~10	At Re=88000, Z/D=6, r/D<5,average Nu increase 80%, the researchers achieve this by inserting slotted cylinder into nozzle, the pressure drop increases 500 times
	Mesh at the nozzle exit	*Gardon and Akfirat	1966	Slot jet L/D=96, 48, 24	450~ 50,000	1/3~8 0	The stagnation heat transfer rates at Z/D=6 are increase, when Z/D ≥6 increases are not obvious.
	Mesh at the nozzle exit	*Hoogendoom	1977	Contoured & Long Pipe	66,000	2~9	$Nu/Re^{1/2} = 0.65 + 2.03\left(\frac{Tu Re^{1/2}}{100}\right) - 2.46\left(\frac{Tu Re^{1/2}}{100}\right)$ Pr=0.71, 2x10⁴≤Re≤9x10⁴, 9%≤Tu≤20%, 1≤Z/D≤10
Increasing Jet Turbulence	Cylinder array in flow	Kataoka et al.	1992	Contoured Slot	4,500	2, 4, 6, 8	At Re=57000, Z/D=10, rod width L_1=4mm, rod-plate spacing L_2/L_1=1.5 average Nu increases 35% at r/D<3.
	Square rod array in flow	*Kum et al.	1995	Slot jet	6,300~57,000	2,6,10 .14	At Re=4500, Z/D=6, cylinder d=8mm, cylinder-plate spacing X/d=4~6, Nu increase within r/D<2, and Nu increase 80% at stagnation point
	Pulsation Jet	*Azavedo et al.	1994	Long Pipe L/D=131	5,200~24,300	6	No increase in Nu at the frequency ranged studied (0~183Hz)
	Pulsation Jet	Sailor et al.	1999	Pipe with pulsation valve L/D=3.64	21,000~31,000	4, 6, 8	At Z/D=6, Re=26000, 20% increase in stagnation heat transfer rate is observed at 30Hz, at Re=31000, 50% is observed at 30Hz.
	Spinning blade	*Zumbrunnen and Aziz	1993	Convergent Slot	3,100~20,750		At small Reynolds number Re=9450, Nu increased at higher frequency f=90~130. For Re=16000, heat transfer deteriorates at center r<2, increases r>2 at f=30~130.
	Oscillating Cylinder in flow	Haneda et al.	1998	Contoured	9,100~10,400	3	At Re=9100, Z/D=5, Nu increases at r/D<3, and the max. enhancement occurs at r/D=0.5
	Acoustic excitation	*Liu and Sullivan	1996	Contoured	12,270~15,100	1~11	At Re=12300, 1.125≤Z/D≤2, Nu increase at the frequency around natural frequency f_n, Decreases at 0.6~0.8f_n
	Acoustic excitation	Gau et al.	1997	Contoured slot	2,750~22,000	0~12	At Re=11000, exictation frequency f_e/f_n=0.25, Nu increase at 3≤r/D≤12, the enhancement decreases as Z/D increases. At Z/D=6, no enhancement is observed
Surface Modification	a spike protuberance at the center of plate	Hrycak	1984	Contoured, lip-equipped	14 000, 26 000, 54 000, 67 000	5~20	Re=14,000~26,000, Z/D=4~14, stagnation heat transfer rate increase is observed
	Different type of fins	*Hansen and Webb	1993	Long pipe L/D=94, 68	4,700~24,000 8,100~33,000	1~14	Re=14100, avg Nu from pyramidal fins is larger than short square fins at Z/D<14, both larger than smooth surface, tall square fins is smaller than smooth surface. Re=20 400, averaged Nu from short squ. fins is the largest, next is pyramidal fins. Z/D<5, tall squ. fin larger than smooth surface.

* Details given in this section

Figure 2.19: Summary of impinging jet heat transfer enhancement techniques
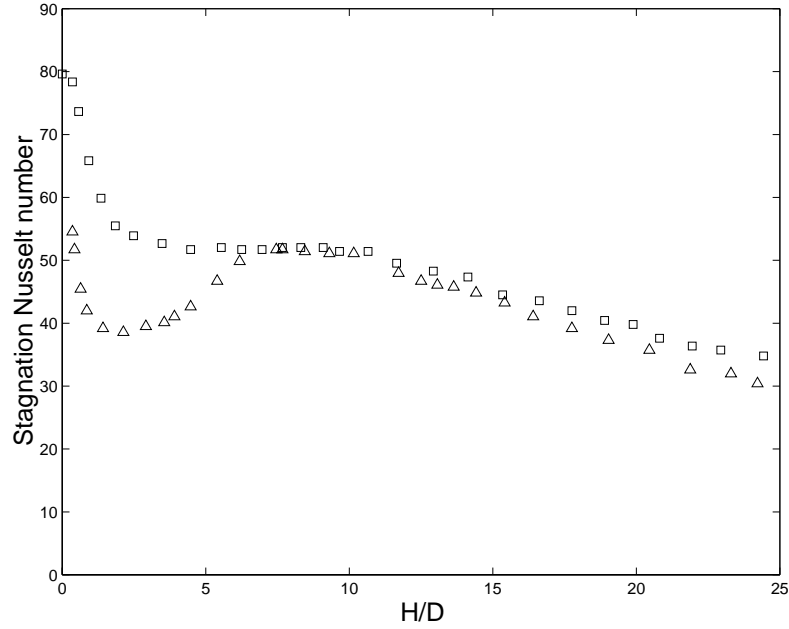
Figure 2.20: The effect of increasing the turbulence intensity on stagnation point Nusselt number as a function of jet to plate spacing for a slot jet with Re=11,000 [43], △ plain nozzle, □ nozzle with turbulence promoter.

of the number of a round impinging jet could be approximated as

$$\frac{Nu}{Re^{1/2}} = 0.65 + 2.03 \left(\frac{TuRe^{1/2}}{100}\right) - 2.46 \left(\frac{TuRe^{1/2}}{100}\right)^2, \qquad (2.11)$$

for the range $20000 < Re < 90000$, $9\% \le Tu \le 20\%$ and $1 \le H/D \le 10$.

Although the turbulence level is an important parameter in determining the mixing in a round jet, it is now recognized that the nature of the underlying structures play an important role in determining the mixing in the jet[70] and hence the heat transfer on the wall. For example, it has long been recognized that the peak in the stagnation heat transfer in an impinging jet at H/D=6 corresponded to the intermittent motion of the end of the potential core in the free jet.

A number of investigators developed devices to enhance the intermittent nature of the jet, and hence increase heat transfer. For example, Azevedo et. al [38] used a rotating valve in a long pipe, 130 diameters upstream, to pulse the jet at the exit.

The variation of the stagnation Nusselt number measured in a jet with a Reynolds number of 15,800 for a range of frequencies are shown in figure 2.21. The Strouhal numbers, St, given by

$$St = \frac{fD}{U_{exit}}, \tag{2.12}$$

range from 0 to 1.116. The stagnation heat transfer rate is actually reduced by more than 25% for all cases relative to the steady case, despite the fact that the turbulence level in the pulsed jet was generally 2-7 times larger than that of the steady jet. The pulsations primarily add energy to large scale ring structures that may act to stabilize the jet impingement rather than increasing the intermittency of the impingement.
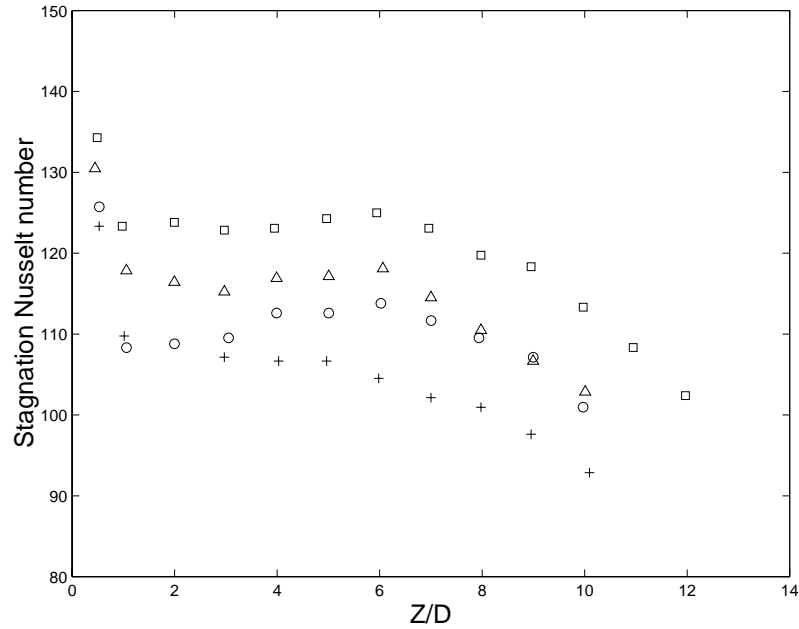
Figure 2.21: Variation of stagnation Nusselt number with nozzle-plate spacing[38], Re=15,800, pulsation frequency f_n: □ 0Hz, ○ 67Hz, St=0.409, △ 133Hz, St=0.817, + 183Hz, St=1.116.

Zumbrunnen and Aziz[22] later attempted to enhance the intermittency by using rotating impeller that passed through the jet as illustrated in Figure 2.22. The blades on the impeller should deflect the flow and increase the intermittency of the flow. A

comparison of Nusselt number for a range of blade passing frequencies for the jet
with Reynolds number 9,450 and 16,000 is shown in Figure 2.23 and 2.24. For the
lower Reynolds number jet, the local Nusselt numbers are smaller than that for the
steady jet when the Strouhal number corresponding to the blade passage frequency
was 0.084 and 0.165. For larger Strouhal numbers, the heat transfer was significantly
enhanced. The stagnation Nusselt number was 200% larger for the steady jet when the
intermittency is at the highest frequency (St=0.365), which is close to the natural
frequency of the free jet. At higher Reynolds number Re=16000, the fixed blade
passage frequencies investigated corresponded to Strouhal numbers less than 0.215.
Enhancement only occurs in the field far from the stagnation point $r/D \geq 2$, which
is identical with the low Reynolds number case.
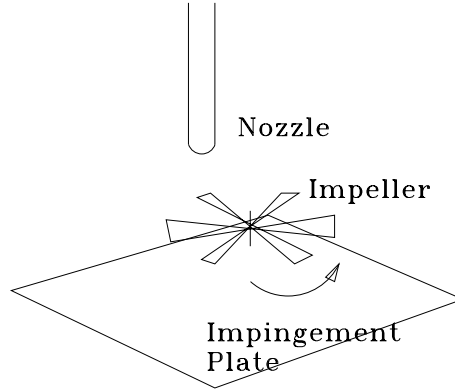
Figure 2.22: Sketch of the rotating impeller enhancement techniques

In many applications, it is not practical to force the jet using a rotating valve or
impeller. Thus, several recent investigations have attempted to enhance the develop-
ment of large-scale structures in the jet using acoustical forcing similar to the forcing
used for the free jet. Liu and Sullivan[46] used a loudspeaker in the settling chamber
to excite the organ-pipe resonance in the chamber and produce plane-wave excitation
at the jet exit. The Strouhal number of the measured natural frequency $St_n \approx 1.23$
when jet-to-plate spacing H/D$\geq$1.3 and as H/D decreases, the natural frequency, or
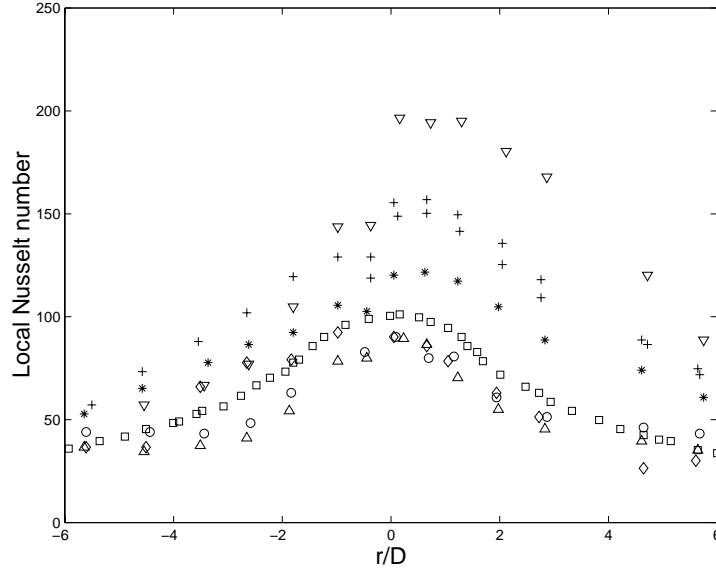
Figure 2.23: Local time-averaged Nusselt number for intermittent jets[22] with Re=9,450 and Pr=5.6 for a blade passage frequency: – steady jet, △ f=30Hz, St=0.084, ◯ f=59Hz, St=0.165, ◇ f=94Hz, St=0.264, + f=104Hz, St=0.292, □ f=117Hz, St=0.326, ▽ f=130Hz, St=0.365.
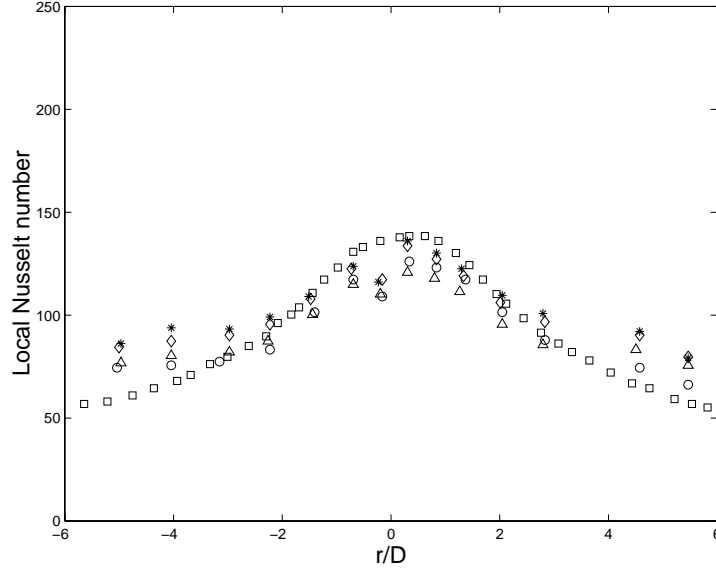
Figure 2.24: Local time-averaged Nusselt number for intermittent jets[22] with Re=16,000 and Pr=5.6 for a blade passage frequency: – steady jet, △ f=31Hz, St=0.057, ◯ f=60Hz, St=0.111, ◇ f=90Hz, St=0.166, □ f=116Hz, St=0.215.
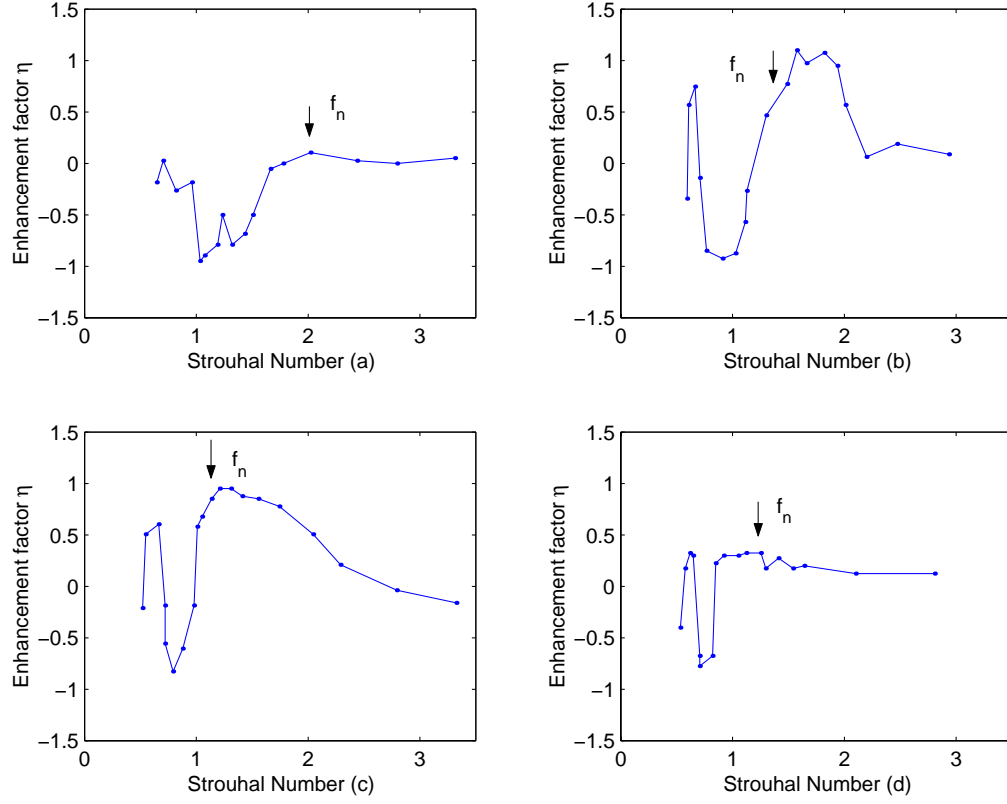
Figure 2.25: Heat transfer enhancement factor as a function of excitation Strouhal number at r/D=1.53[46], Re=12,300, natural frequency $f_n = 1400Hz$, heat transfer enhancement factor $\eta = \frac{h(f_e)}{h(f_e=0)} - 1$, (a) H/D=0.625, (b) 1.125, (c) H/D=1.63, (d) H/D=2.

St_n, increased. A comparison of heat transfer enhancement results for different excitation frequencies at r/D=1.53 and H/D=0.625~2 is shown in Figure 2.25. Here, r/D=1.53 corresponds to the secondary peak of heat transfer rate. The heat transfer at this point is enhanced when the St≈1.2 for H/D≥1.63, St≈1.5 for H/D=1.125 and St≈2 for H/D=0.0625. These correspond to the natural frequencies for each jet-to-plate spacings. When the jet is forced near the subharmonic of the natural frequency a heat transfer reduction is observed.

2.5.2 Surface Modification

Extended surfaces or fins can be added to the surface in order to enhance the area for heat transfer and hence the heat transfer from the surface. Protrusions can also be added to promote turbulence in the radial wall jet enhancing the heat transfer from the surface. The protrusion will increase the surface area somewhat but their primary function is to promote turbulence and enhance heat transfer on the impinging surface.
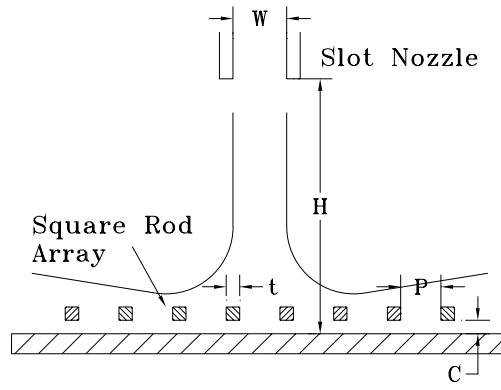
Figure 2.26: Schematic of the test facility of Kum and Kawaguchi[44], W=50mm, t=4mm, P/t=7.5, C/t=0.25, 0.5, 1, 1.5, H/D=2, 10.

Kum and Kawaguchi [44] used a square rod array over the heat transfer surface in a plane jet as shown in Figure 2.26. The rods are above the wall so they will create a fast moving wall jet flow between the rod and the plate and a wake behind the rod. The fast moving wall flow will enhance the heat transfer under the rod and the shear layers on both side of rod will increase the turbulence intensity on the wall and promote heat transfer. The heat transfer rate measured for several different rod-to-plate spacing for a jet-to-plate spacing of 2 slot widths is shown in Figure 2.27. The results for a jet-to-plate spacing of 10 slot widths is shown in Figure 2.28. In both cases, the local Nusselt number has a sawtooth pattern as the heat transfer reaches a maximum under each rod where the flow has been accelerated through the gap between the rod and plate. The effect of the rods are much more pronounced for the

near impingement cases. This is not unexpected since the flow is more fully developed for the large impingement distance and the rods do not act as much as turbulence promoters.

Hansen and Webb [45] examined the heat transfer rate for three different types of extended surfaces, shown in Figure 2.29; short square fins, tall square fins, and pyramidal fins. The average Nusselt number for these three types of fins and smooth surface at Re=14,100 and 20,400 are shown in Figure 2.30 and 2.31. The variation in the Nusselt number for the smooth surface and the modified surface show the similar trend for both Reynolds number as expected[37][26]. The pyramidal fins enhance the average Nusselt number over the entire jet-to-plate spacing considered for both Reynolds number except at large H/D for Re=20400. The short square fins enhance the average Nusselt number for all test conditions. The tall square fins enhance the average Nusselt number at small H/D and large Reynolds number, and reduce the average Nusselt number for all other conditions. Pyramidal fins have more surface exposed to oblique impingement than the short square fins which could explain the difference in the heat transfer enhancement for these two type of fins. The tall fins block the radial development of the wall jet causing the thermal boundary layer to grow faster, so the heat transfer enhancement caused by the increase in the surface area and turbulence cannot offset reduction due to the thickening of the boundary layer. Therefore, the average Nusselt number is likely to be the result of the different turbulence level, flow velocity at the surface and the percentages of total find surface area exposed to normal impingement, oblique impingement and parallel flow.
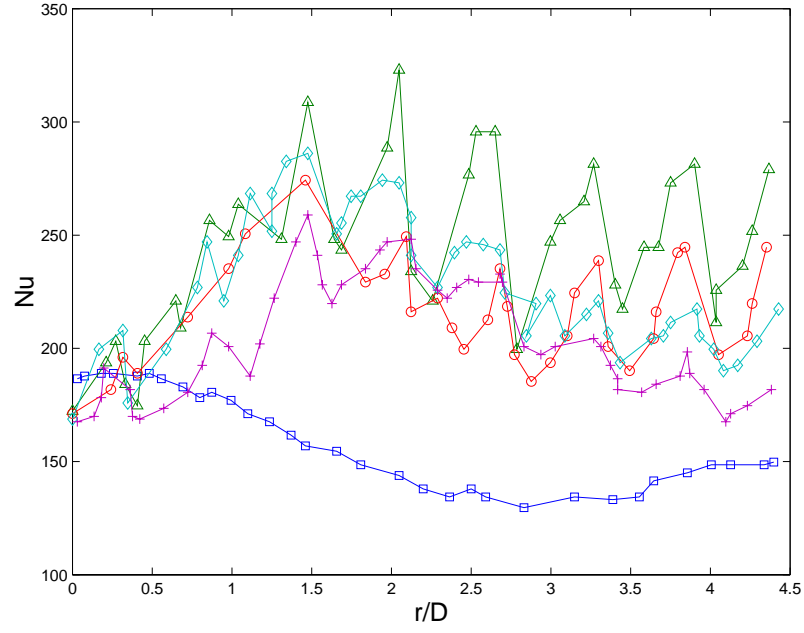
Figure 2.27: Effect of clearance between square rods and plate on the Nusselt number[44], Re=57,000, H/D=2, □ without rods, △ c/t=0.25, ○ c/t=0.5, ◊ c/t=1, + c/t=1.5.
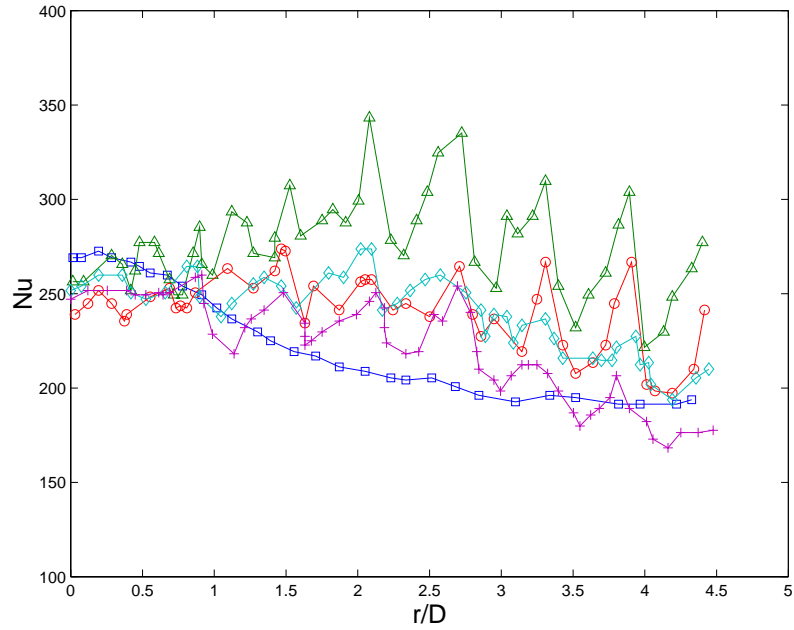
Figure 2.28: Effect of clearance between square rods and plate on the Nusselt number[44], Re=57,000, H/D=10. □ without rods, △ c/t=0.25, ○ c/t=0.5, ◊ c/t=1, + c/t=1.5.
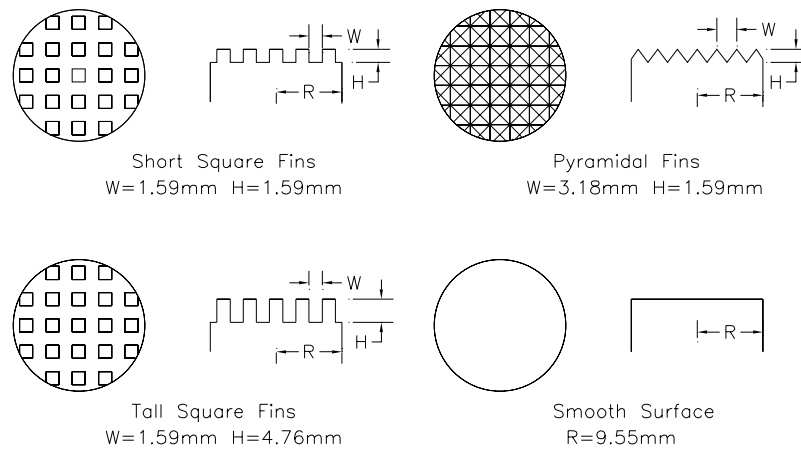
Figure 2.29: Schematic of the modified surfaces used by Hansen and Webb[45], radius R=9.55mm, nozzle diameter D=6.91mm and 13.3mm.
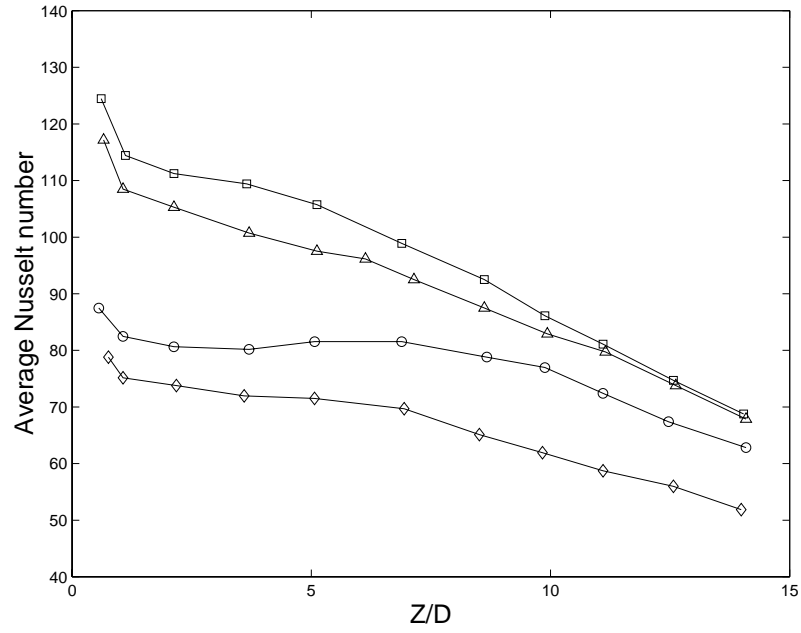
Figure 2.30: Average Nusselt number as a function of H/D[45], nozzle diameter D=6.91mm for Re=14,100(r/D≤ 1.38), □ pyramidal fins, △ short square fins, ◯ smooth surface, ◇ tall square fins.
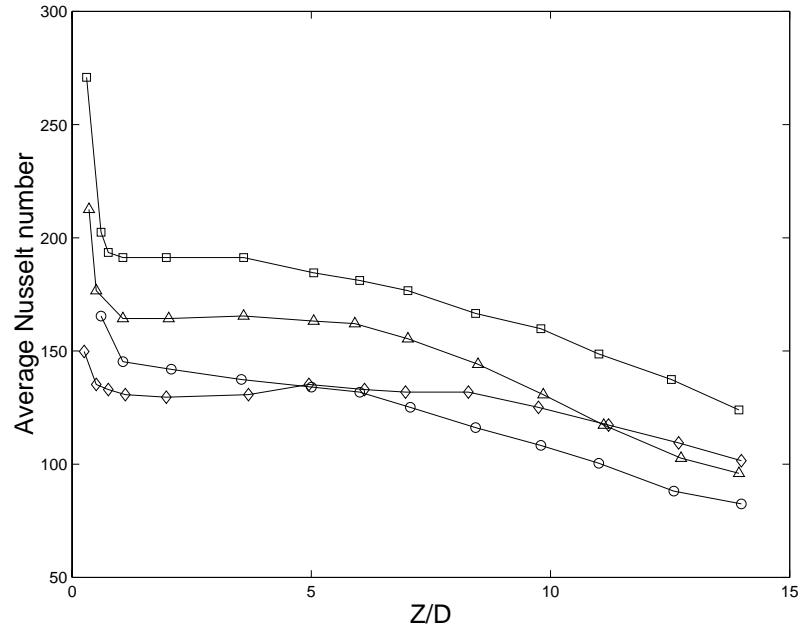
Figure 2.31: Average Nusselt number as a function of H/D, Nozzle diameter D=13.3mm for Re=20 400(r/D≤0.72) Hansen and Webb[45], □ pyramidal fins, △ short square fins, ◯ smooth surface, ◇ tall square fins.

Chapter 3

Experimental Methodology

The heat transfer rate in the impinging jet was measured by examining the flow from a fully developed pipe flow impinging on a thin metal strip. The foil was heated using a regulated power supply and the temperature was measured using an infrared thermal camera. Measurements of the flow field in the impinging jet were performed using a larger flow facility. The details of the experimental setups are discussed in this section and the accuracy of the resulting heat transfer correlations are assessed.

3.1   Heat Transfer Facility

The air jet for the heat transfer experiments was generated using air from the building compressed air line using a configuration shown schematically in Figure 3.1. The flow was initially passed through a pressure regulator that reduced the nominal line pressure from 90 psi down to 75 psi in order to remove the effect of any variations in the line pressure. The flow was also passed through a filter to remove any contaminants. The flow was then passed through a PARKER MB4 flow meter with a control valve to control the flow rate, and flow straighteners were used at the entrance of the pipe to remove any swirling flow caused by the curves in the flexible tubing leading to the

pipe.

A picture of the setup is shown on Figure 3.2. The jet-to-plate spacing was controlled by moving the nozzle up and down using a traversing mechanism that could travel 356mm or 28 diameters. The traverse was mounted at the top of a 50cm×50cm 183cm-tall frame made using 9/16″ Uni-Struct channel. The impingement plate is mounted in the middle of the frame, 100cm above the ground, and the infrared camera is placed below the plate at its minimum focus length of 80cm. The frame was aligned using measurements of the velocity contours at different locations down stream.

The pipe used in this investigation was a 1/2″-inner diameter round steel tube, 48″ or 96 diameters long with a wall thickness of 1/8″. This length is sufficient to yield fully developed turbulent flow at the exit[73]. A 16″ × 16″ 1/4″-thick plexiglas plate was attached to the nozzle to test the confinement effects.

A sketch of the impingement plate is shown in Figure 3.3. The plate consists of a 470mm×57.2mm×0.0254mm stainless steel foil stretched over a 475.2mm×50.8mm 38.1mm-deep air gap in a plexiglas plate. Both ends of the foil were clamped by a pair of 57.2mm-long brass blocks on plexiglas ends that act to hold the foil and serve as electrodes for the foil. One of the plexiglas ends was movable, so the foil could be tensioned.

The electrical resistivity of foil is 0.285Ω. In order to reduce the resistance of the rest of the circuit to minimize the error, heavy gauge copper wires were used to connect the power supply and the electrodes. The contact surfaces of brass electrodes were machined to minimize the contact resistance. The heating was provided using a D-C power supply. Its maximum output current is 20A, corresponding to a maximum heat flux generation of

$$q_t = I^2 R/A \approx 4550 W/m^2. \tag{3.1}$$

The energy added as ohmic heating is primarily lost to forced convection on the top surface, conduction through the bottom surface and the radiation, so that the
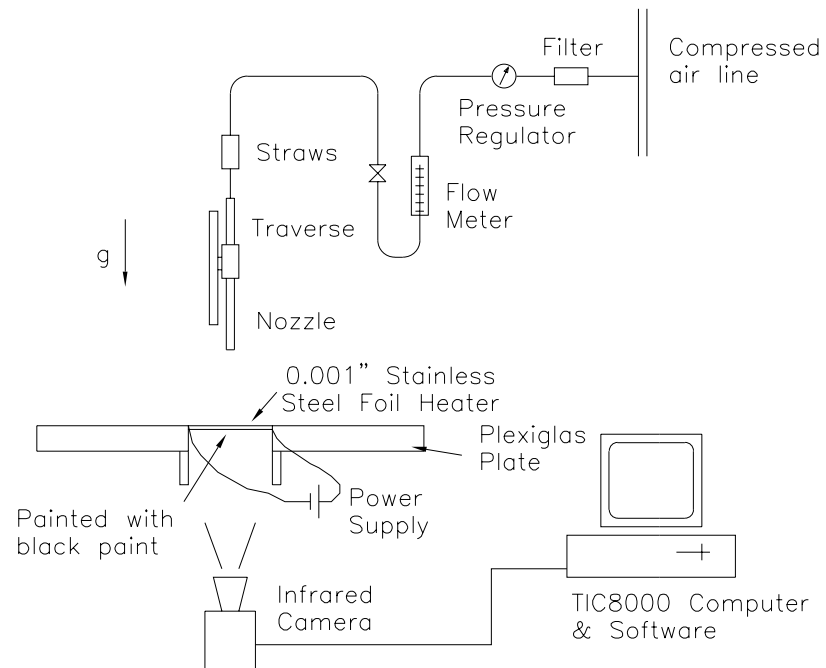
Figure 3.1: Schematic of the flow system

Figure 3.2: Photograph of Uni-Struct frame and traversing mechanism
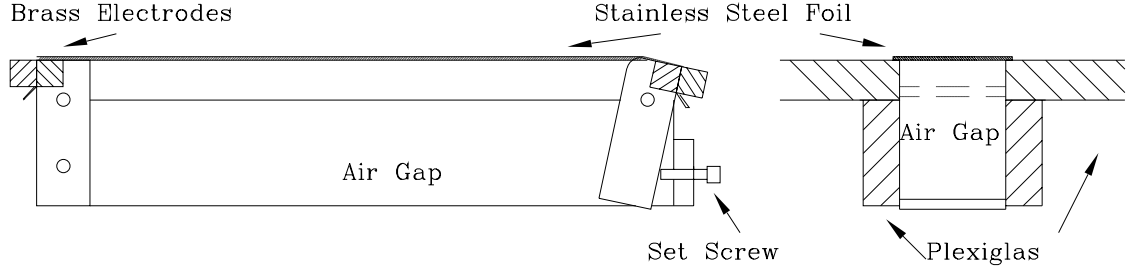
Figure 3.3: Sketch of impingement plate

total energy balance is given by

$$q_t = q_{conv} + q_{cond} + q_r, \tag{3.2}$$

The radiation losses can be estimated by assuming that the plate is a grey body exchanging energy with an ambient surface at 25^oC. The emissivity of the upper surface $\varepsilon_u \approx 0.26$ and the bottom surface $\varepsilon_b \approx 0.99$. It follows that the heat flux from the surface via radiation is approximately

$$q_r = \varepsilon_u \sigma(T_w^4 - T_\infty^4) + \varepsilon_b \sigma(T_w^4 - T_\infty^4) = 210 W/m^2 \tag{3.3}$$

for a maximum wall temperature $T_w \approx 55^oC$ in the region of interest. This is about 5% of total heat flux.

The conduction effects can be broken into two components; conduction losses to the air below the plate, and lateral conduction in the plate. In this investigation, the impingement plate is mounted horizontally, and an air gap with a height of 38.1mm has been created below the plate by putting vertical barriers beside the gap. This air will be stably stratified, suppressing natural convection in this gap. Therefore, the heat loss through conduction can be estimated using a one dimensional approximation. The maximum wall temperature T_w on the foil was approximately 55^oC and the ambient temperature $T_\infty \approx 25^oC$. Thus, it follows the losses through conduction should be smaller than

$$q_{cond} = k_a \frac{T_w - T_\infty}{L_a} \approx 25 W/m^2, \tag{3.4}$$
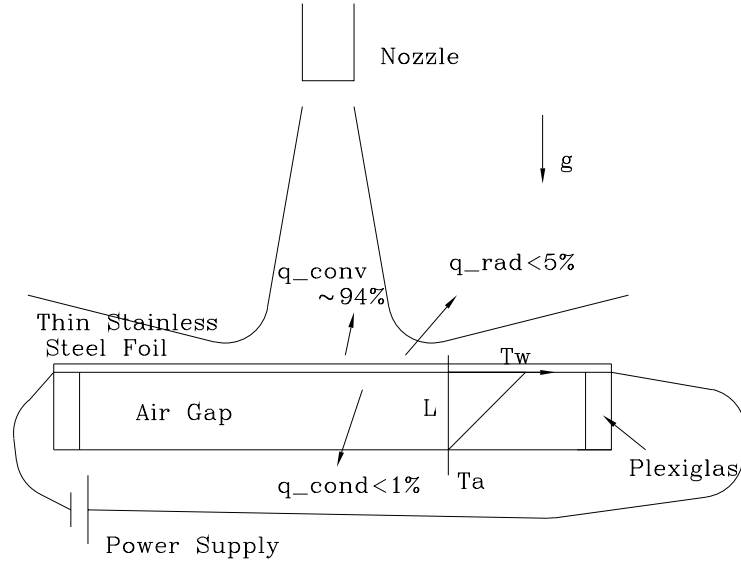
Figure 3.4: Illustration of heat flux distribution

where the thermal conductivity of air has been estimated as $k_a \approx 0.0271 W/mK$ at a film temperature $T_f = 42.5^oC$, and the depth of the air gap $L_a = 38.1mm$. This represents approximately 0.6% of total heat flux. The heat loss through conduction and radiation will not increase the uncertainty of the measurement as they has been considered in estimating the convection heat flux.

The effect of the lateral heat conduction can be estimated by looking at the temperature distribution on the plate shown in Figure 3.5. It is clear that the isotherms form a series of circular rings where the lowest temperature occurs in the center and the temperature grows gradually as r/D increases. The lateral conduction can be estimated by fitting the temperature distribution with a 10th order polynomial, and calculated using a one dimensional finite difference method. The resulting heat flux is shown in Figure 3.6. It is clear the lateral conduction reduces the local maximum in heat transfer and increases the local minimum, smoothing the result. The maximum lateral conduction is about $12W/m^2$, which is 0.3% of the total heat flux, and is neglected here, causing a small increase in the uncertainty of the measurement.
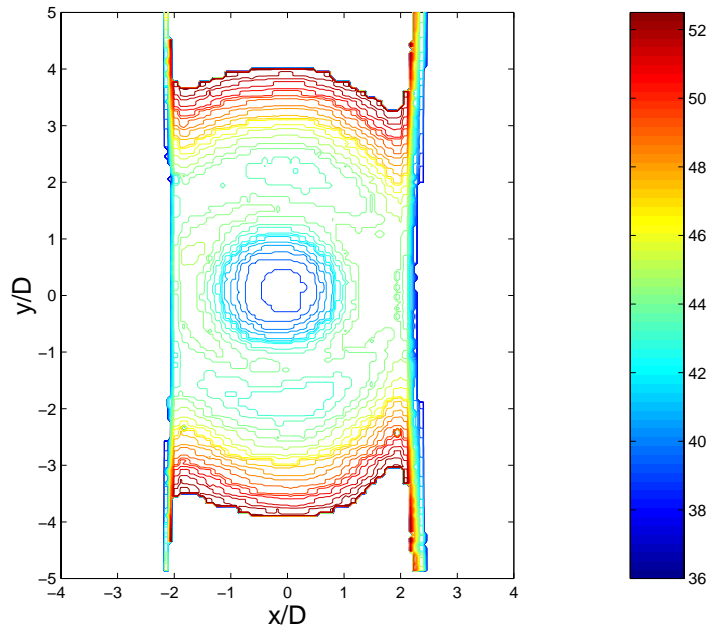
Figure 3.5: Temperature distribution on the foil (^oC), Re=23,000, $q_t = 4550W/m^2$, $T_j = 25^oC$, H/D=2
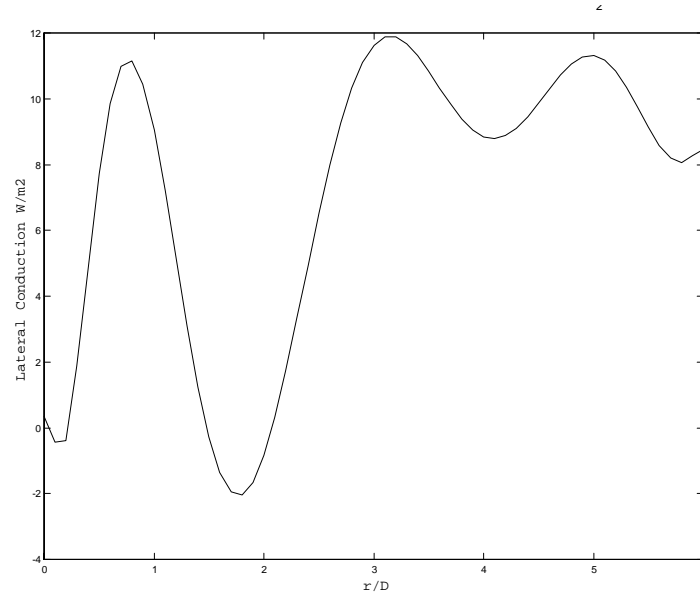
Figure 3.6: Distribution of the lateral conduction heat loss in the foil, Re=23,000 $q_t = 4550W/m^2$, $T_j = 25^oC$, H/D=2

In order to avoid interference between the infrared camera and the impinging jet, the temperature of the foil is measured on the bottom. The typical heat transfer coefficient measured in this investigation is $80W/m^2K \sim 320W/m^2K$[26]. It follows the largest Biot number of the foil is approximately

$$Bi = \frac{ht_f}{k_f} = \frac{320\frac{W}{m^2K}0.0127 \times 10^{-3}m}{15\frac{W}{mK}} = 2.7 \times 10^{-4}, \tag{3.5}$$

where t_f is the half thickness of the foil and k_f is the thermal conductivity of stainless steel. Thus, the temperature difference between the top to the bottom of the foil is negligible[58].

The local heat transfer rate and Nusselt number has been defined in Equation 1.2 and Equation 1.1 on page 3. If the velocity of the jet is considerably larger, the compressibility of the air should be considered, and the local heat transfer coefficient should be defined as

$$h = \frac{q_{conv}}{T_w - T_{aw}}, \tag{3.6}$$

where q_{conv} is convective heat flux, T_w is the wall temperature and T_{aw} is the adiabatic wall temperature. The adiabatic wall temperature can be estimated as

$$T_{aw} = T_j(1 + r_R\frac{\gamma - 1}{2}M^2), \tag{3.7}$$

where T_j is static jet temperature. The maximum jet velocity in this investigation is under 40m/s, thus, the maximum adiabatic temperature for a local recovery factor, r_R of 1 is given by

$$T_{aw} = T_j(r_R\frac{\gamma - 1}{2}M^2) \approx T_j(1 + 1\frac{1.4 - 1}{2}(\frac{40}{343})^2) = 1.0027T_j. \tag{3.8}$$

Therefore, T_{aw} can be approximated by T_j accurately.

The local Nusselt number can be integrated to obtain an average Nusselt number,

$$\overline{Nu} = \frac{2}{R^2} \int_0^R Nu(r)rdr = \frac{q_{conv}D}{k_a(\overline{T_w} - T_j)}, \tag{3.9}$$

where the average wall temperature in the area πR^2 is given by

$$\overline{T_w} = \frac{2}{R^2} \int_0^R T_w r dr. \tag{3.10}$$

3.2 Experimental Procedure

The infrared camera was precisely calibrated by the manufacturer. However, the system still required the following parameters to calculate the temperature maps: the emissivity of the object, the distance between the lens and the plate, the ambient temperature and the ambient emissivity. Ambient temperature was obtained by reading a mercury thermometer. The ratio of foil area to surrounding area is so small that it is reasonable to assume that the ambient emissivity is 1. The bottom of the foil was painted with a thin layer of candle soot black paint to ensure it had a uniform emissivity that was near 1, and it was measured by determining the emissivity of the surface at a known temperature.

It is very difficult to use thermocouples to measure the surface temperature because the foil is so thin that thermocouple would act as a fin. Thus, for calibration process, the foil was mounted on a steel container that could be filled with heated water. The wall was initially sanded to ensure a good contact between the wall and the foil. The container was insulated using Styrofoam except for a $2'' \times 2''$ window, as shown in Figure 3.7. The container was filled with hot water and the temperature of water was measured using a mercury thermometer position at the same depth as the middle of the window. A series of images were taken using the thermal camera as the water cooled down from 80^oC to 50^oC. The images were then used to compute the emissivity of the foil. The cooling process took approximately 10 hours so the temperature change was sufficiently slow enough to ensure there was no concern about any quasi-transient effect. In analyzing the images, it was assumed the foil and box had the same temperature as the hot water. This assumption can be verified using
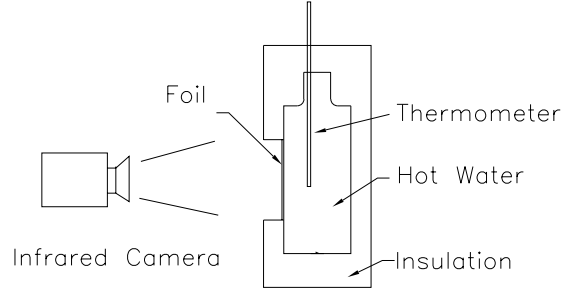
Figure 3.7: Calibration of foil emissivity

a simple one-dimensional heat transfer analysis using correlation from Incropera and Dewitt[58]. It is found the average heat transfer coefficient for the natural convection outside of the window was approximately $18W/m^2K$. The total wall and foil thickness is 0.28mm, so it follows the Biot number is approximately

$$Biot = \frac{hL}{k_a} = \frac{18W/m^2K0.028 \times 10^{-3}m}{15W/mK} = 0.034 \times 10^{-3}. \qquad (3.11)$$

Therefore, the temperature measured by the infrared camera and the thermometer should be same. The emissivity computed from the calibration data was between 0.94 and 0.97. An emissivity value of 0.96 gave the most consistent fit.

E-type thermocouples were used in this investigation to measure the jet temperature and room temperature. They were calibrated in this facility. Thermocouples were placed into water with the thermometer and measurements from the two transducers were recorded as the water cooled gradually from 90^oC to 22^oC. A calibration curve was generated for each thermocouple.

The jet temperature was measured by inserting a E-type thermocouple at the exit of the nozzle. The thermocouple was measured using a 16-channel COMPUTER-BOARDS PCI-CIO-TC data acquisition board connected to a PC. This board was a 16 bit A/D board so the smallest resolution that could be measured with the board was $\pm0.04^oC$ for an E-type thermocouple. A mercury thermometer was used to read the room temperature. In all cases, it was found that the difference between the jet

temperature T_j and room temperature T_∞ was less than $\pm 0.3^oC$, which was approximately 2.5% of minimum difference between jet and wall temperature. This would be considered in estimating the measurement uncertainty.

The AGEMA Thermovision 880 infrared camera was positioned 90cm below the impingement plate. The camera detecting band width was selected to be 20^oC. The CATS software for the camera was capable of determining the temperature of the foil once the ambient temperature, ambient emissivity, plate-camera spacing and foil emissivity were entered into the program running on TIC-8000 computer. The images of the temperature fields were then moved to a Pentium computer by grabbing the image display on the monitor for the TIC-8000 computer using a MATROX Meteor-II/Multi-Channel RGB frame grabber. The images could then be analyzed using a program to determine the local and average Nusselt number.

3.3 Free Jet Flow Field Investigations

The streamwise velocity distribution of the free jet used in the impinging heat transfer study were measured using a DISA 55M hotwire anemometry system. A National Instrument PCI-MIO-16E-4 data acquisition board and Labview were used to acquire data. The sampling frequency was 2KHz. At jet-to-plate spacings H/D=0∼4, 20,000 data points were taken and at H/D=6∼10, where the turbulence intensity was relatively high, 40,000 data points were taken.

The hotwire was calibrated using a pitot tube and manometer in the jet exiting a convergent nozzle that ensured the velocity profile at the jet exit was uniform. The output voltage of the hotwire and velocity from the pitot tube were recorded for different velocities ranging from 0m/s ∼ 40m/s. The data was then fitted using a fourth order polynomial to form the calibration curve for the hotwire. The hotwire was then mounted on a three dimensional traverse that could move the probe through
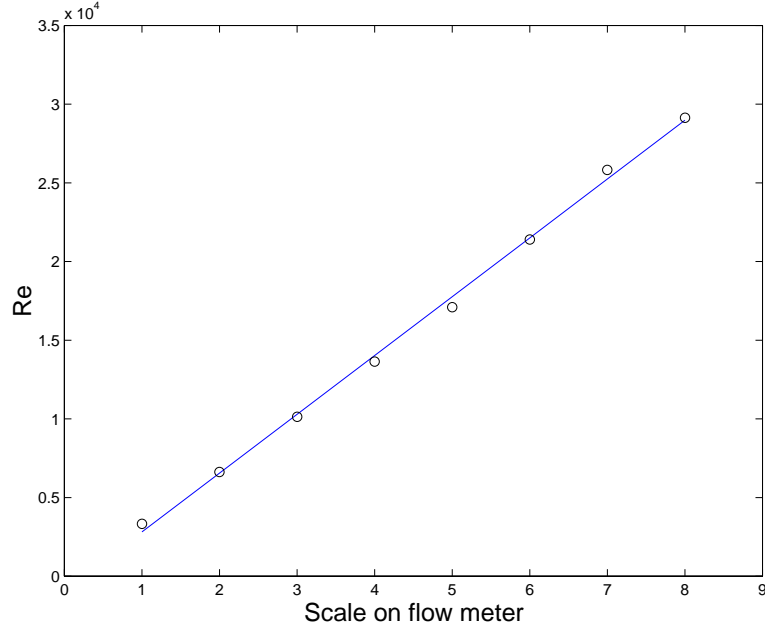
Figure 3.8: Calibration of flowmeter for D=12.7mm nozzle

the jet exiting the long pipe.

The first step in examining the jet velocity field was to ensure that the nozzle was perpendicular to the ground. The center of mean streamwise velocity at jet-to-plate spacing H/D=0 to 16 was obtained by analyzing the symmetry of the mean and fluctuating velocity distributions. It was found the deviation of nozzle axis from the normal to the ground was approximately 0.384^o which was considered sufficiently small.

The PARKER MB4 flow meter used in this investigation was calibrated by measuring the free jet centerline velocity at the exit of the nozzle as the scale on the flow meter was found not to be accurate. The average velocity was calculated by multiplying the centerline velocity with 0.817 [55]. Reynolds number was given by Re=$\overline{U}D/\nu$ and shown in Figure 3.8.

3.4   Impinging Jet Flow Field Investigations

Investigations of the flow field were performed on the impinging jet in order to gain a greater insight into how the heat transfer enhancement schemes modify the turbulent structures in the impinging jet. The investigations of the flow field were carried out in a second facility with a 1.5″ diameter long pipe shown in Figure 3.9. In this case the flow was driven by a blower that empties into a settling chamber. The flow was then conditioned using a stack of 10" diameter air filters. The flow then entered a bell mouth and passed through a second flow conditioning stage consisting of 5″ long 1/8″ diameter straws and a screen. The flow then exited through a 50 diameter long pipe. The impingement plate is a $3' \times 3'$ aluminum plate, with 136 0.0625″ diameter pressure taps on radii shown in Figure 3.10. Sennheiser microphones were mounted on these taps using 1/16″ diameter flexible tubing to measure the dynamic pressure and Validyne DP45 differential pressure transducer was used to measure the mean gauge pressure. The signals from the microphones were sampled using a Microstar 1816 A/D board and analyzed using routines written in Labview.

The pressure spectrum were calculated by Fourier transforming the dynamic pressure

$$F_{pp}(f) = \sum_{i=-N/2}^{N/2} R_{pp}(t_i)e^{-j2\pi t_i f/N},$$

(3.12)

so that the variance of the dynamic pressure was computed by integrating the spectrum

$$\overline{V_p^2} = \int_{-\infty}^{\infty} F_{pp}(f)df.$$

(3.13)

Two microphones were used to measure the azimuthal correlation between various positions on each diameter. The correlations were Fourier transformed to obtained the azimuthal modal energy distribution. If ring shape vortices dominated the flow at the location studied, the results would be more correlated and most of the energy
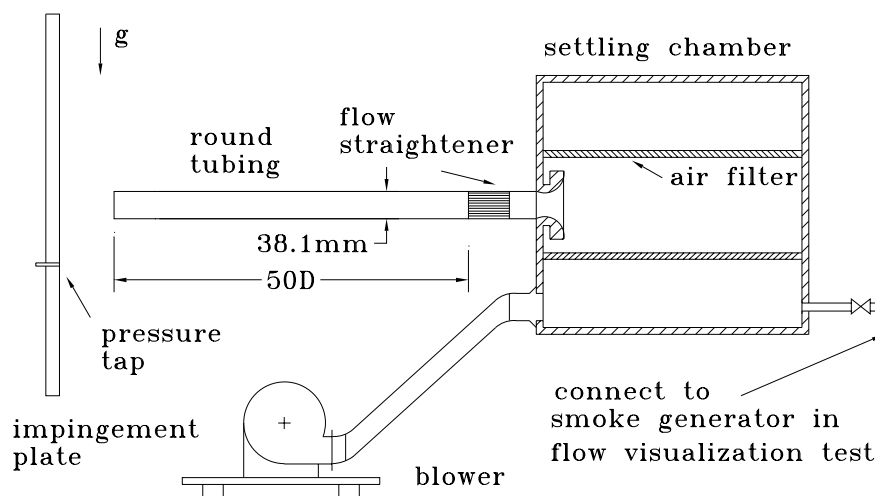
Figure 3.9: Schematic arrangement of the apparatus for pressure measurement on impingement plate
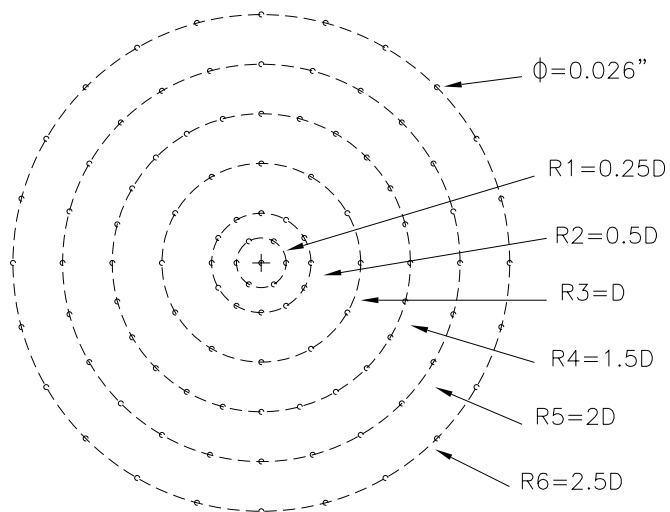
Figure 3.10: Pressure measurement holes in plate
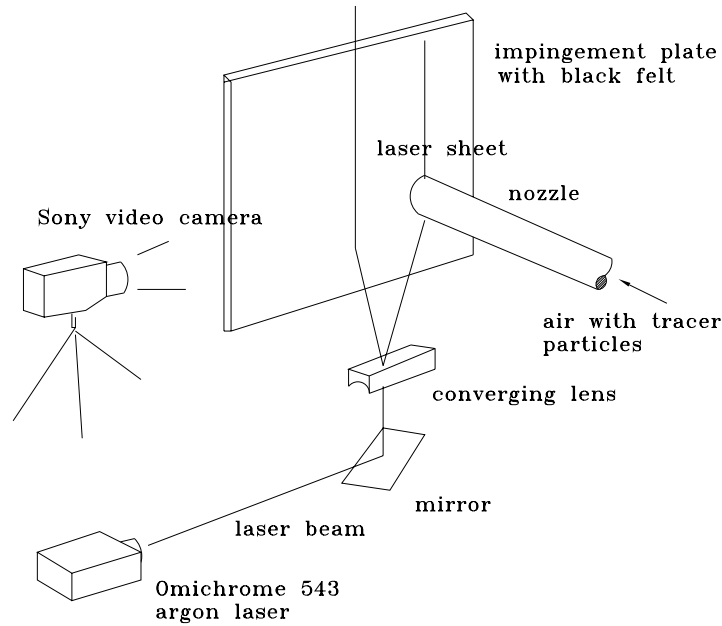
Figure 3.11: Schematic arrangement of the apparatus for flow visualization

would be contained in the zero mode of the energy distribution. Less organized flow would be poorly correlated and less energy would be contained in the zero mode.

The apparatus used in flow visualization is sketched in Figure 3.11. The impingement plate and the end of the pipe nozzle were covered by dark felt to minimize reflection. The tracer particles were the smoke of hydro-carbon oil generated by a ROSCO Alpha 900 fog generator, and were injected directly into the settling chamber. An Omichrome argon laser (model 543) with maximum radiant power of 210mW was used as the light source. A thin light sheet was generated by passing the laser beam through a cylindrical lens and converging lense. Continuous images were recorded using a Sony CCD-V9 video camera and digitized by a ATI All-in-one Wonder frame grabber.

3.5   Error Analysis

The uncertainty of the heat transfer correlations defined in this investigations were evaluated using the method given by Kline and McClintock[57]. In this approach if a variable y is a function of several independent variables, say given by $(x_1, x_2 \ldots x_n)$, each with uncertainty $(u_1, u_2 \ldots u_n)$, then it follows the uncertainty of y

$$u_y = \sqrt{(\frac{\partial y}{\partial x_1}u_1)^2 + (\frac{\partial y}{\partial x_2}u_2)^2 + \ldots (\frac{\partial y}{\partial x_3}u_3)^2}. \tag{3.14}$$

This approach can then be used to estimated the uncertainty in the quantities used to determine the heat transfer and mass flow rate. For example, the heat generated by Joulean heating is given by

$$q_t = \frac{IV}{A}, \tag{3.15}$$

where I is the current, V is the voltage, and A is the area of the foil. The value and uncertainty of each variables is listed in table 3.4. The uncertainty of total heat flux generation q_t is given by

$$u_{q_t} = \sqrt{\sum (\frac{\partial q_t}{\partial x_i}u_i)^2}/q_t = 1.35\%. \tag{3.16}$$

The heat transfer convected from the plate by the impinging jet was computed by subtracting the radiation and conduction heat transfer from the total heat flux, given in Equation 3.2, so the Nusselt number is given by

$$Nu = \frac{hD}{k_a} = \frac{q_t D}{k_a(T_w - T_j)} - \frac{\varepsilon \sigma D}{k_a}(\frac{T_w^4 - T_\infty^4}{T_w - T_j}) - \frac{D}{L_f}. \tag{3.17}$$

The typical values and uncertainties of these five variables at the stagnation point are listed in the Table 3.5 for the case where Re=23,000, H/D=2, $q_t = 4500W/m^2$, and Nu=160. The thermal camera was capable of an accuracy of 0.07^oC, but this only applies to a small temperature measuring band of 2^oC. In this investigation the thermal range of infrared camera was 20^oC. If the temperature of the impingement

		x_i	u_i	$\left|\frac{\partial q_t}{\partial x_i}u_i\right|$
Current (amp)	I	20.0	0.05	0.441
Voltage(Volt)	V	5.7	0.05	1.159
Foil Area(m^2)	A	0.0261	0.00026	1.765

Table 3.4: List of variables and uncertainties for uncertainty of total heat flux

		x_i	u_i	$\left|\frac{\partial Nu}{\partial x_i}u_i\right|$
Heat flux(W/m^2)	q_t	4500	73	2.966
Emissivity	ε	0.96	0.01	0.031
Nozzle Diameter(m)	D	0.0127	0.00005	0.693
Jet Temperature(^oC)	T_∞	25	0.3	4.409
Wall Temperature(^oC)	T_w	32	0.1/0.175	1.472/2.577

Table 3.5: List of variables and uncertainties s for uncertainty of Nusselt number

		x_i	u_i	$\left|\frac{\partial Re}{\partial x_i}u_i\right|$
Flow rate (m^3/s)	$\dot{V}$	0.00359	0.000108	863.4
Nozzle Diameter(m)	D	0.0127	0.00005	115.1

Table 3.6: List of variables and uncertainties for uncertainty of Reynolds number

plate T_w was read manually from the TIC-8000 computer, the accuracy of the temperature was $\pm 0.1^o C$. If the thermal images were acquired with the frame grabber and processed using a Matlab routine, the accuracy drops to $\pm 0.175^o C$. The uncertainty of the total heat flux is estimated to be 1.35%. The lateral conduction heat loss is less than 1%, so the total uncertainty for the heat flux is 1.68%. It follows that the uncertainty in the Nusselt number at the impingement point is given by

$$u_{Nu} = \sqrt{\sum (\frac{\partial Nu}{\partial x_i} u_i)^2} / Nu = 3.30\% \qquad (3.18)$$

for the data obtained manually, and $u_{Nu} = 4.52\%$ for the data computed by image process software. The uncertainty of the other points tends to be lower than the stagnation point. These uncertainties of the Nusselt number are estimated using a 90% confidence level. Thus, the Nusselt number measurement will have errors less than 6.6% and 9% at 95% confidence level.

A nominal Reynolds number 23,000 was used in this investigation, corresponding to a volumetric flow rate of $\dot{V} = 0.00359 m^3/s$. The uncertainty in the flow meter and the nozzle diameter are given in Table 3.5. It follows that the uncertainty of Reynolds number is given by

$$u_{Re} = \sqrt{\sum (\frac{\partial Re}{\partial x_i} u_i)^2} / Re = 3.55\%, \qquad (3.19)$$

so that the Reynolds number is accurate to $\pm 7\%$ at 95% confidence level.

Chapter 4

Results and Discussion

The objective of this investigation was to examine the effectiveness of two different heat transfer enhancement strategies; tabs on the nozzle exit that enhance mixing in the impinging jet and heat transfer on the plate, and trips on the heat transfer surface that promote turbulence in the wall jet flow that in turn promotes heat transfer. The heat transfer enhancement introduced by both these approaches was measured for a jet exiting a fully developed pipe for jet-to-plate spacings ranging from 1 to 10. Flow visualization studies and measurements of the velocity field were also performed to gain insight into the flow mechanisms that caused the heat transfer enhancement. The experimental rig used in this study was first qualified. In this section, measurements of the velocity field and heat transfer for impinging jet data are presented and compared to existing results. Measurements of the heat transfer for the confined jet exiting a long pipe, which have not been examined previously, are also presented and discussed. This is followed by a discussion of heat transfer enhancement in the jet with tabs and flow studies are then discussed. Finally, the heat transfer enhancement caused by the trips on the heat transfer surface are presented.

4.1 Velocity Field Measurement in the Free Jet

The Reynolds number of the jet for most of the heat transfer measurements considered was set to 23,000 to facilitate comparison with the previous measurements of Baughn and Shimizu[26] and Lytle and Webb[38]. The distribution of free jet mean velocity at the nozzle exit Z/D=0 is shown in Figure 4.1. This is compared with a fit for the velocity profile in the core of a fully developed turbulent flow given by[55]

$$U = U_{max}(1 - \frac{r}{R})^{1/7} \tag{4.1}$$

that has been shown to be in good agreement with previous measurement for $2 \times 10^4 < Re < 2 \times 10^5$. There is reasonable agreement between the two profiles indicating the flow at the exit of this nozzle is fully developed turbulent flow.

The symmetry of the jet was checked by measuring both the mean velocity and the turbulence intensity profiles in the jet. For example, the rms value of the streamwise fluctuating velocity at Z/D=4 and 8 are shown in Figure 4.2. The distributions show reasonable symmetry along the centerline.

The evolution of the centerline mean velocity and the half-width of the jet exiting the long pipe in the heat transfer facility are shown in Figure 4.3 and 4.4. Here, the jet half-width is defined as the radius where the mean velocity is half the local centerline velocity. The growth rate downstream become constant and is given by 0.069. The inflection in the growth rate of the jet and the centerline decay occurs at approximately Z/D=6 corresponds to the end of the potential core in the jet.

The evolution of the mean streamwise velocity and the rms value of the streamwise fluctuating velocity are shown in Figure 4.5 and Figure 4.6, normalized using the exit centerline mean velocity. The velocity profile in the near field of the jet exiting the long pipe differs from those in a jet exiting a contoured nozzle that is often studied. In particular, the flow in the pipe is being sheared by the presence of the walls so there is already a region of high mean shear near the edges of the jet exiting the pipe
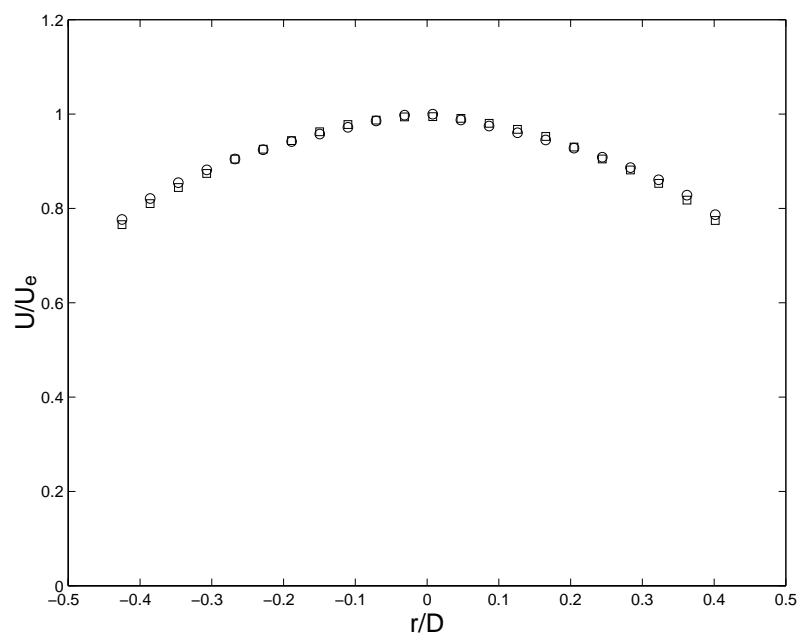
Figure 4.1: The mean streamwise velocity profile at Z/D=0 for Re=23,000, □ measured at the exit of long pipe, ◯ fully developed turbulent flow
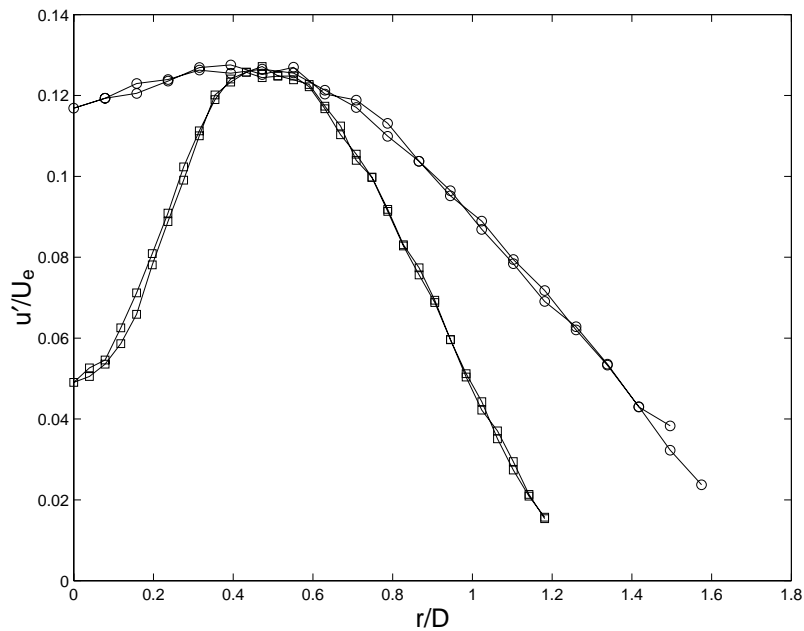
Figure 4.2: The distribution of the rms value of the fluctuating streamwise velocity at □ Z/D=4 and ◯ Z/D=8 for Re=23,000, normalized by centerline exit mean velocity.
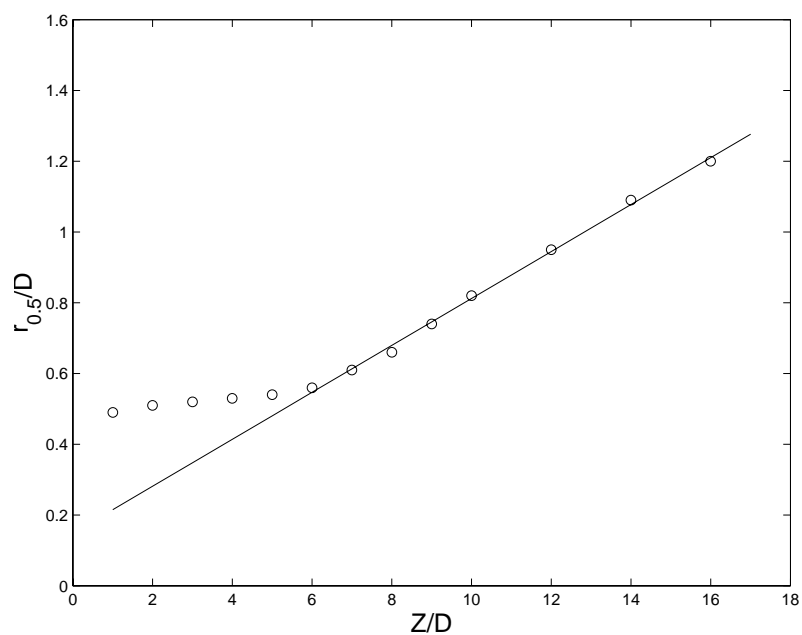
Figure 4.3: Evolution of free jet half-width $r_{0.5}$, where $r_{0.5}$ is the radius $U = U_{0.5}$.
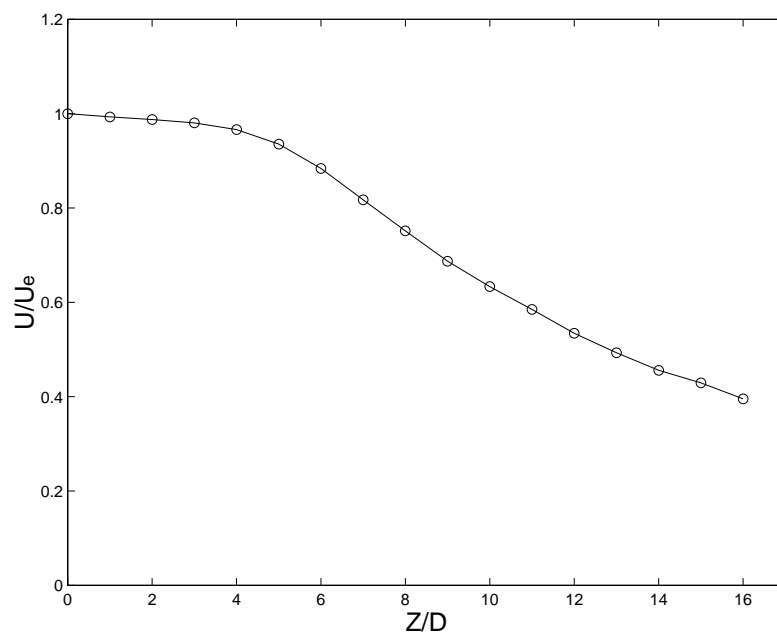
Figure 4.4: Evolution of the centerline mean velocity in the free jet for Re=23,000.
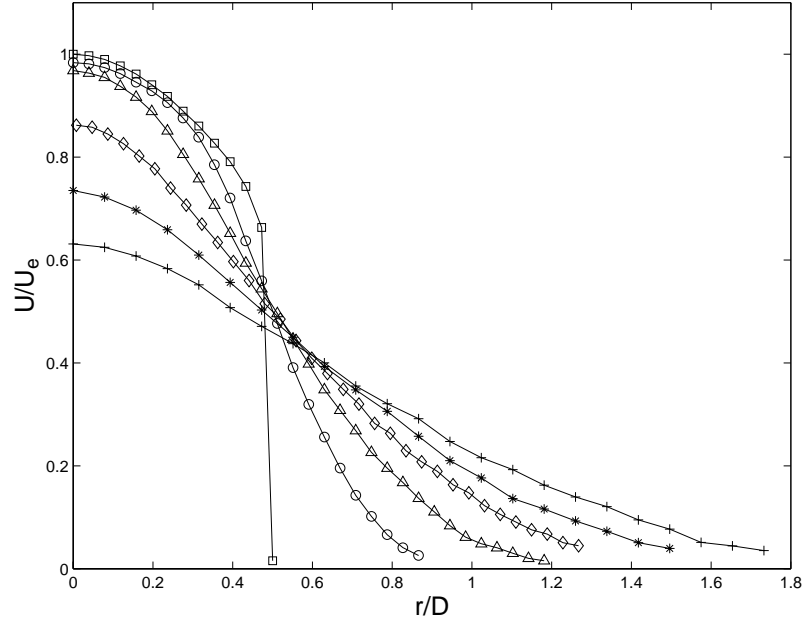
Figure 4.5: Distribution of mean streamwise velocity U, normalized by centerline exit mean velocity for Re=23,000, □ Z/D=0; ◯ Z/D=2; △ Z/D=4; ◇ Z/D=6; ∗ Z/D=8; + Z/D=10
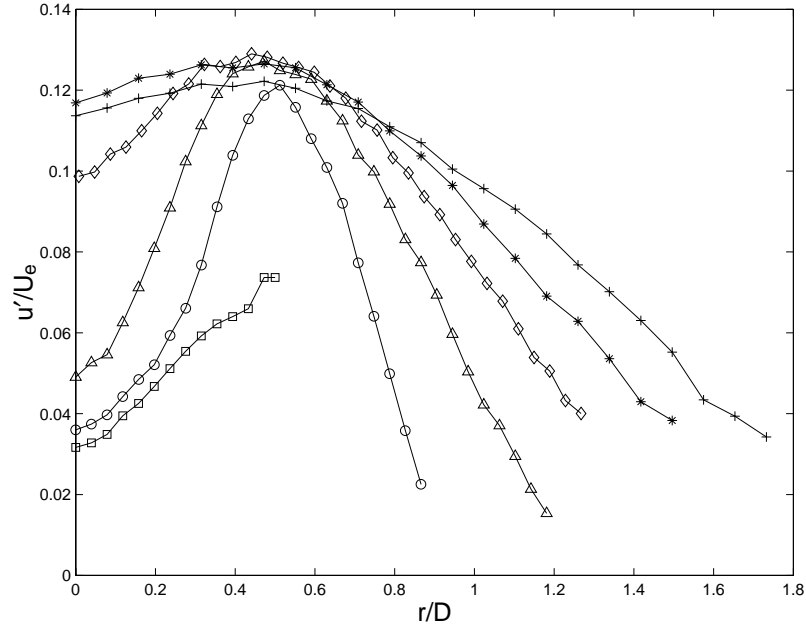
Figure 4.6: Distribution of rms value of the fluctuating streamwise velocity, $u' = (\overline{u^2})^{1/2}$, normalized by centerline exit mean velocity for Re=23,000, the symbols are the same as above.

and the flow in the center has adjusted to this shear. It is clear, however, that the flow adjusts to the change in boundary conditions at its edge in a manner similar to the jet exiting a contoured nozzle. Namely, a new axisymmetric shear layer forms on the outside of the flow where the mean velocity and turbulence fields adjust first and this moves in toward the center of the jet as the flow evolves downstream. The velocity profile in the core of the jet is essentially unaffected until Z/D=6 when the centerline velocity decays. The turbulence levels in the jet begin to rise at Z/D=4 but this is most likely caused by irrotational motions imposed by the axisymmetric shear layer that is also observed in the jet exiting the contoured nozzle. Thus, although the core of the jet exiting a long pipe can not be properly called a potential core, it has many of the same features as the potential core in the jet exiting a contoured nozzle.

The profile of the fluctuating velocity has many of the expected features. In the near field, the peak occurs approximately at the center of the shear layer. As mentioned previously, the turbulence intensity increases from Z/D=2 to 4 because of the irrotational fluctuations caused by the passage of large-scale structures in the shear layer. The significant rise from Z/D=4 to 6 is associated with the collapse of the core of the jet where the large-scale structures in the shear layer penetrate to the center of the jet. It should also be noted that the magnitude of the turbulent fluctuations at the centerline continue to increase in size from Z/D=6 to 8 despite the decay of the centerline velocity in the region.

4.2 Heat Transfer From a Long Pipe Jet

The heat transfer was measured for the unconfined jet with Reynolds number of 23,000. A comparison of the measurements for an impingement distance H/D=6 with the results from Lytle and Webb[38], Baughn and Shimizu[26] and Yan *et al.* [29] are shown in Figure 4.7. It is clear that the results are in good agreement with
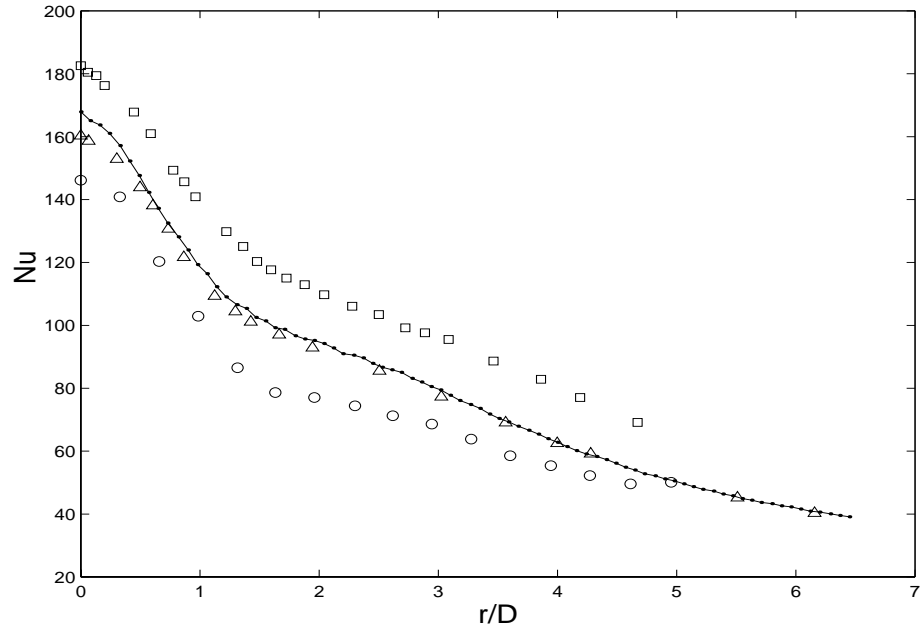
Figure 4.7: Comparison of local Nusselt number distributions for Re=23,000 and H/D=6 measured − in this investigation, □ by Lytle and Webb[37], △ by Baughn and Shimizu[26], ◯ by Yan *et al.*[29].
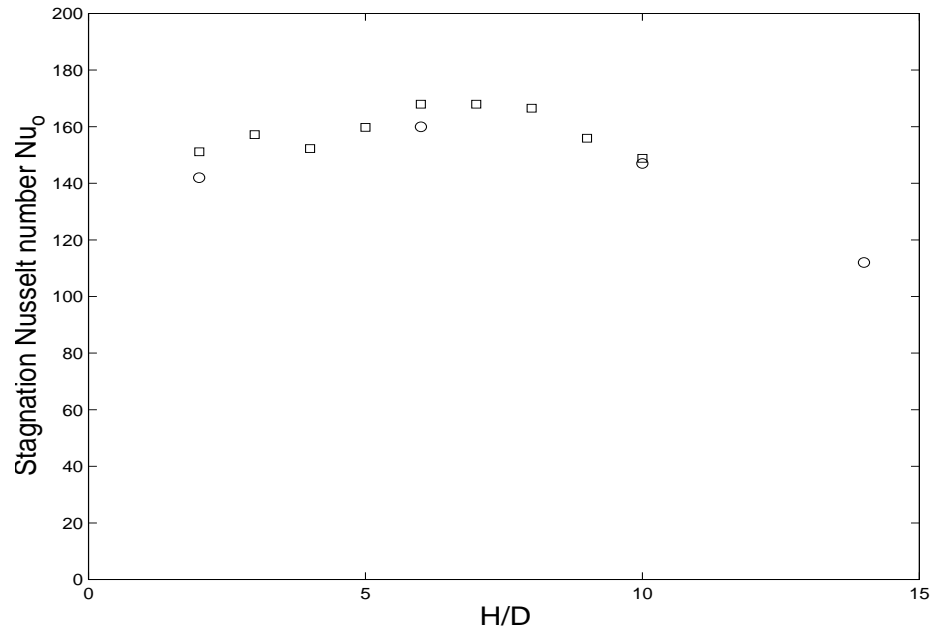
Figure 4.8: The stagnation Nusselt number as a function of jet-to-plate spacings, H/D, for Re=23,000 measured □ in this test, ◯ by Baughn and Shimizu[26].

Baughn and Shimizu's[26] data, which are considered to be accurate over the entire region considered. The largest deviation between the results at the centerline region is the approximately 5%. The deviation elsewhere is considerably smaller. The cause of the large deviation in the impingement region is not known, but it is within the range of the reported experimental uncertainties. The measurements performed here are considerably better than other reported data that often has unexplained deviation that is significantly larger than the reported experimental uncertainties.

A comparison of stagnation Nusselt number, Nu_o, measured for jet-to-plate spacing of $2 \leq H/D \leq 10$ with the results from Baughn and Shimizu[26] is shown on Figure 4.8. The results again are in good agreement with the largest deviation being approximately 6%. The more detailed measurements of the stagnation heat transfer in this investigation also provide further insight how the stagnation heat transfer changes with jet-to-plate spacing. For example, it is clear that the peak in the stagnation heat transfer is broad extending from approximately $6 \leq H/D \leq 8$ before it begins to decay. This is not unexpected since the measurement of the velocity field in the free jet showed that the turbulent fluctuations in the center of the jet continued to increase from Z/D=6 to 8 before beginning to decrease. Thus, the effect of these increasing fluctuations could offset the effect of the decrease in the mean velocity on the centerline. It is also evident that the increase in the centerline heat transfer does not begin until H/D=5. This is, again, consistent with the velocity measurements in the free jet that showed the centerline turbulence intensity increased significantly after Z/D=4.

It should also be noted that the apparent peak at H/D=3 is likely caused by experimental error. Later measurements performed while examining the effect of confinement suggest that the Nusselt number for H/D=3 in this figure is too high and the result for H/D=4 is too low. These results showed the Nusselt number should smoothly transit from H/D=2 to 5.
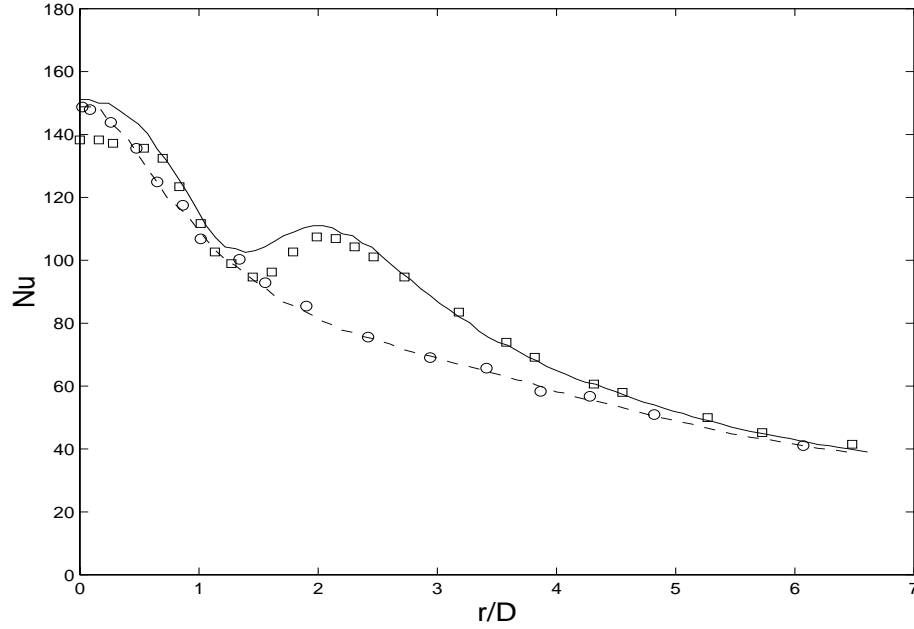
Figure 4.9: Local Nusselt number distribution for Re=23,000 for − H/D=2, - - H/D=10, measured in this investigation; and □ H/D=2, ○ H/D=10, from Baughn and Shimizu[26].

Finally, a comparison of the Nusselt number distributions for jet-to-plate spacing H/D=2 and 10 with the results from Baughn and Shimizu's data[26] are shown in Figure 4.9. The measurements for H/D=10 are in very good agreement. The results for H/D=2 are in fairly good agreement except near the centerline. The location and size of the secondary peak is well predicted. There is a difference between the measurements of the local minimum. The largest deviation between the two sets of measurement is less than 7%. The cause of the deviation for the heat transfer at the centerline is not clear. Both experiments were performed using a constant heat flux foil heater, so the temperature difference between the jet and foil is the smallest at the centerline. Thus, any error in determining either of these temperatures would have the largest effect at this location.

Overall, it is clear that the measurements performed in the heat transfer facility constructed for this investigation are in reasonable agreement with the data of Baughn and Shimizu[26]. This result also gives us further confidence that Baughn and Shimizu's[26] data represents reasonably accurate measurements of the heat transfer in the impinging jet. There are some discrepancies between the measurements but they are within the range of experimental uncertainty and are certainly smaller than those observed in other experiments.

The impinging jet produced by a fully developed pipe flow is an excellent test case to test turbulence models used to predict heat transfer using a computational approach because the exit condition at the jet is well known. Thus, it was felt that it would be useful to expand the existing data for this flow before proceeding to examine the heat transfer enhancement. In particular, more detail measurements were performed to examine how the Nusselt number distributions were affected by changes in jet-to-plate spacing, Reynolds number, and confinement.

Jet to Plate Spacing

Baughn and Shimizu[26] reported heat transfer measurements for jet-to-plate spacings of H/D=2, 6 and 10. Measurements were performed here between jet-to-plate spacings 2 and 10 to examine the changes in the Nusselt number distributions. The Nusselt number distribution in the impinging jet with a Reynolds number 23,000 for jet-to-plate spacings ranging from H/D=2-6 are shown in Figure 4.10, while the results for H/D=6-10 are shown in Figure 4.11. There are a number of interesting features in these results. It is apparent that the Nusselt number distribution between the impingement region and the secondary peak, $0.5 \leq r/D \leq 1.5$ are nearly identical for jet-to-plate spacing between 2 and 8 diameters. The distributions for H/D=6-8 are essentially identical in the impingement region as well. The Nusselt number distribution are significantly different for r/D≥1.5. Pronounced secondary peaks are
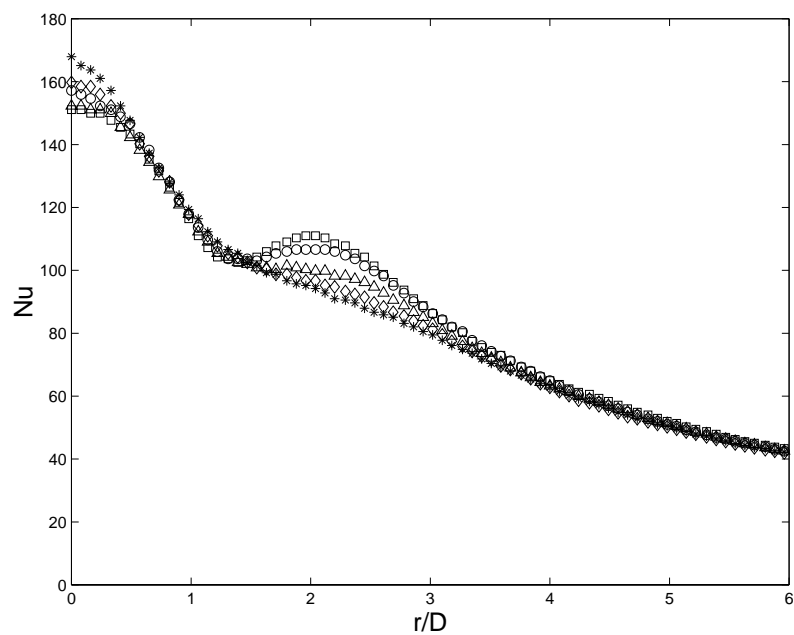
Figure 4.10: Local Nusselt number distribution for Re=23,000 at jet-to-plate spacing □ H/D=2, ◯ 3, △ 4, ◇ 5, and * 6.
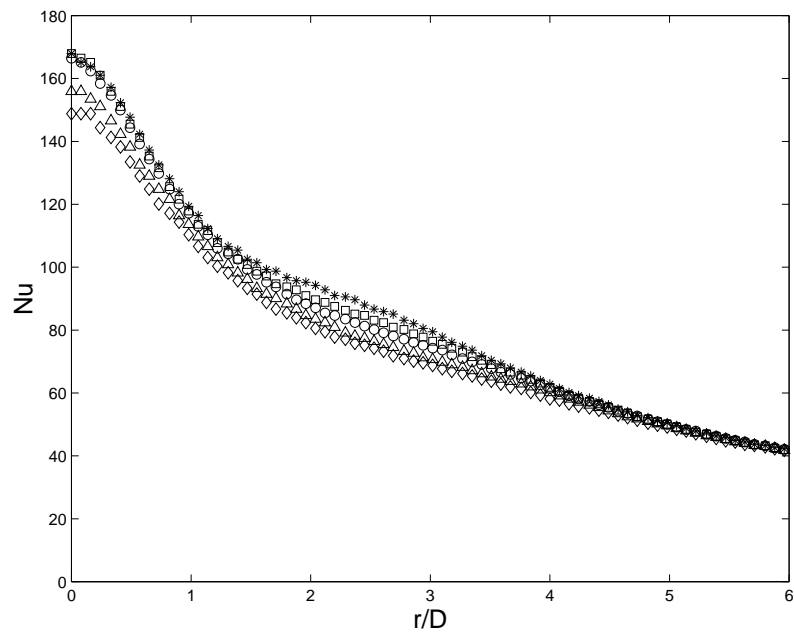
Figure 4.11: Local Nusselt number distribution for Re=23,000 at jet-to-plate spacing * H/D=6, □ 7, ◯ 8, △ 9, and ◇ 10.

observed for jet-to-plate spacings of 2 and 3 diameters. There is a secondary maximum for H/D=4 but is significantly smaller than that for H/D=3 indicating that there has been a change in the development of the radial wall jet when the jet-to-plate spacing was increased. For jet-to-plate spacing greater than 5 diameters there is no longer a local maximum in the heat transfer but there is still an inflection in the heat transfer profile. This inflection in the Nusselt number distribution occurs for H/D=5-8. In fact, the main difference between the profile for H/D=6-8 is the disappearance of the secondary peak.

The presence and decay of the secondary peak in the heat transfer distribution is similar to the results observed for a jet exiting a contoured nozzle. This suggests that the same mechanism, namely vortex separation and break up may be causing the secondary peak in the heat transfer in the jet exiting the long pipe. This, again, suggests that the development of the jet exiting the pipe is dominated by the large-scale ring structures in the shear layer despite the presence of the turbulence in the flow exiting the pipe.

The average Nusselt number distributions at jet-to-plate spacings H/D=2-6 are shown on Figure 4.12. Physically, the average Nusselt number is the measure of the total heat transfer from the region inside of the radius for the constant wall temperature case. In the case of a fixed heat flux, it is inversely related to the average wall temperature over the region; i.e, the larger the average Nusselt number, the lower the average wall temperature. It is clear that the impinging jet with H/D=6 produces the largest average Nusselt number over small areas with radii up to approximately 2 diameters. For larger areas, smaller jet-to-plate spacing, H/D=2 produces a larger average Nusselt number because of the secondary peak in the heat transfer. This becomes particularly pronounced as the jet-to-plate spacing was further decreased[37].

The measurements of the heat transfer showed that the flow mechanism causing the secondary peak in the heat transfer seemed to affect the measurements up to
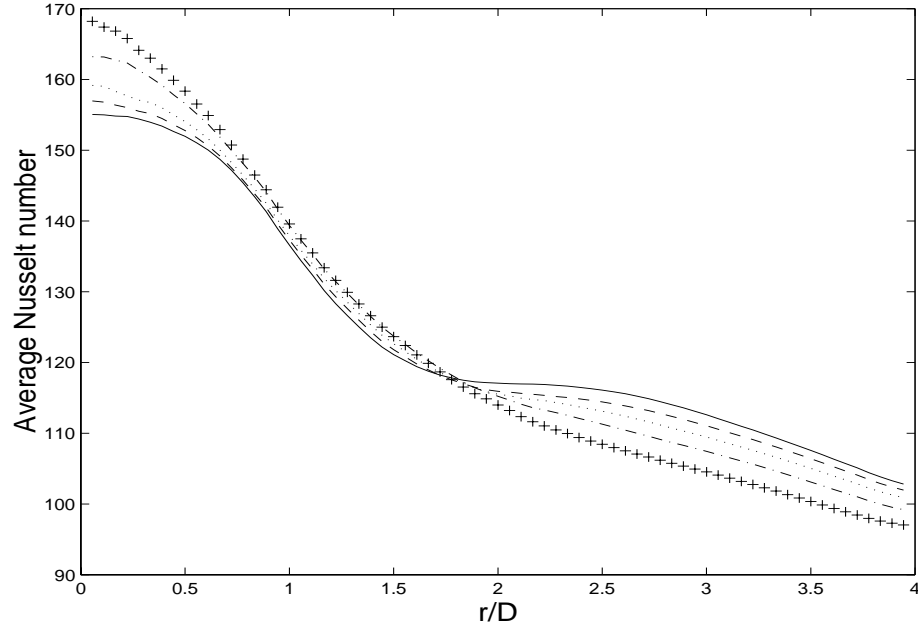
Figure 4.12: Average Nusselt number distribution for Re=23,000 at jet-to-plate spacing − H/D=2, - - 3, ··· 4, -.- 5, and + 6.

H/D≈7. There is a significant change in the size of the effect between H/D=3 and 4. Measurements of the large-scale structures in the radial wall jet were performed at H/D=2 and 4 in order to examine the difference between these two cases. In particular, measurements of the dynamic wall pressure on the impingement surface were performed for r/D=0.25-2.0 in order to examine the dynamics of the turbulent structures.

Measurements were initially performed for H/D=2 to examine if the mechanism causing the secondary peak could be measured using the dynamic pressure. The distribution of pressure spectrum at radial locations r/D=0.5-2.0 for jet-to-plate spacing H/D=2 is shown in Figure 4.13. The pressure spectrum changes between r/D=0.5 and 1, indicating there is a difference in the flow in the deflection or impingement region and the wall jet. The peaks of the spectra for r/D=1 and 1.5 occur at 130Hz which corresponds to a Strouhal number of 0.36 indicating these peaks are associated

Figure 4.13: Spectra of the dynamic wall pressure for jet-to-plate spacing H/D=2 measured at − r/D=0.25, ··· r/D=0.5, -.- r/D=1, - - r/D=1.5, and + r/D=2.

with vortex rings traveling across the plate. The peak in the magnitude increased between r/D=1 and r/D=1.5 caused by vortex stretching as the ring moves out over the plate. Then the peak decreases significantly between r/D=1.5 and r/D=2 and shifts to a lower frequency with broader peak indicating that the vortex has either separated from the wall or broken down.

The previous investigations of vortex separation, including Popiel and Trass[5] and Landreth and Adrian[7], have only reviewed the vortex separation from a two dimensional perspective. The visualization and measurements have not showed the evolution of the structures in the azimuthal direction. Here, the azimuthal correlation of the pressure around the impingement plate at r/D=1, 1.5 and 2 for H/D=2 were measured. The correlations are shown in Figure 4.14 scaled by $\overline{V_p^2}$. It is clear that

Figure 4.14: Azimuthal correlation of dynamic wall pressure for jet-to-plate spacing H/D=2 measured at □ r/D=1, ◯ r/D=1.5, and △ r/D=2.

Figure 4.15: Azimuthal modal energy distribution for jet-to-plate spacing H/D=2, from left to right r/D=1, 1.5 and 2

the correlation decreases much faster for larger diameters, indicating that the length scale of the flow in this direction has decreased or the ring structures have broken down. The Fourier transform of the correlation are given by

$$B_{pp}(m, r)/\overline{V_p^2} = \frac{1}{2\pi} \int_0^{2\pi} R_{pp}(\triangle\theta, r)\cos(m\triangle\theta)d\triangle\theta, \qquad (4.2)$$

was computed at these locations and the results are shown in Figure 4.15. The relative energy in the different azimuthal modes decreases with mode number at all the radii as one would expect. The normalized spectrum is somewhat deceptive because it suggests the energy in the ring mode has decreased. The un-normalized azimuthal spectrum is shown in Figure 4.16. It is clear that the contribution of the ring mode to the fluctuation pressure does increase from r/D=1-1.5 and then drops off significantly. The relative contribution of the lowest modes has decreased significantly from r/D=1-2, suggesting that either the ring has moved a significant distance from the wall or it has broken down. Previous investigations[7] suggest the ring re-attaches, but this is not apparent in the measurements here.

Measurements were also taken for jet-to-plate spacing H/D=4. A comparison of the mean square value of dynamic wall pressure for H/D=2 and 4 are shown in Figure 4.17. There is again an outer peak in the pressure at r/D≈1.5, but is not as large as for H/D=2 case. The larger peak in variance of the dynamic pressure at $r/D \leq 0.5$ for the H/D=4 case is expected because the turbulent levels in the shear layer and core region are considerable larger.

The distribution of pressure spectrum measured at r/D=0.5-2 for jet-to-plate spacing H/D=4 are shown in Figure 4.18. The most significant difference between the pressure spectra and the spectra measured at H/D=2 and 4 occurs at r/D=1. A comparison of the spectrum measured in two cases is shown in Figure 4.19. There is not a peak in the spectrum of H/D=4 corresponding to the passage of the ring vortice. The peak does occur for r/D=1.5 but it is smaller and broader than the peak
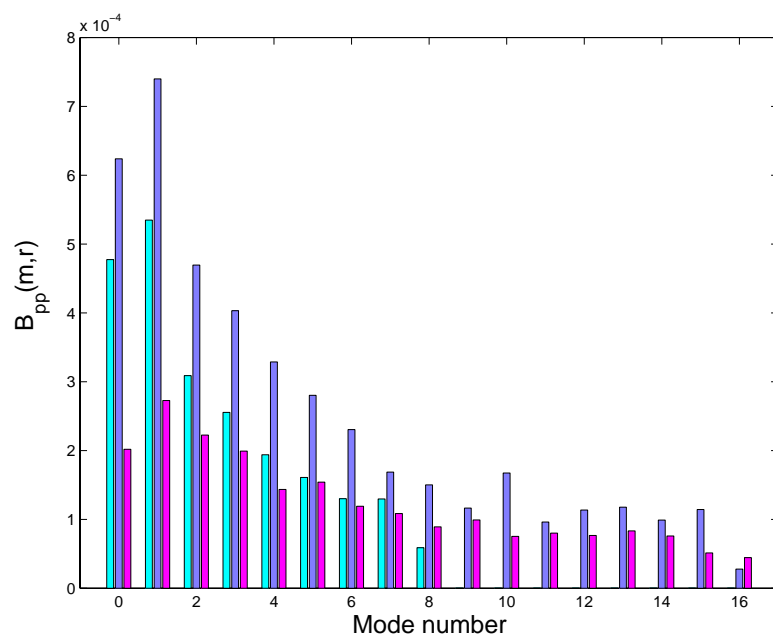
Figure 4.16: Un-normalized azimuthal spectra for jet-to-plate spacing H/D=2, from left to right r/D=1, 1.5 and 2.
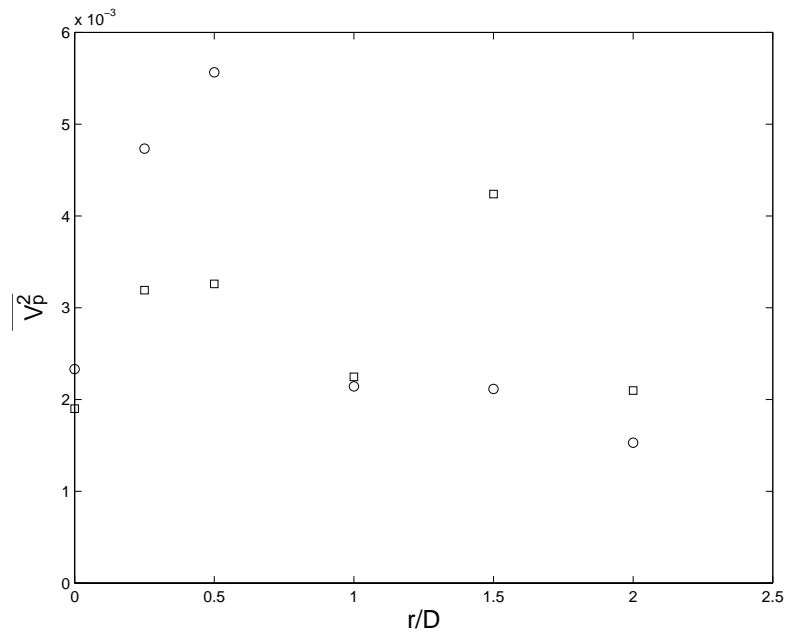
Figure 4.17: The variance of the dynamic wall pressure for jet-to-plate spacing □ H/D=2 and ◯ H/D=4.
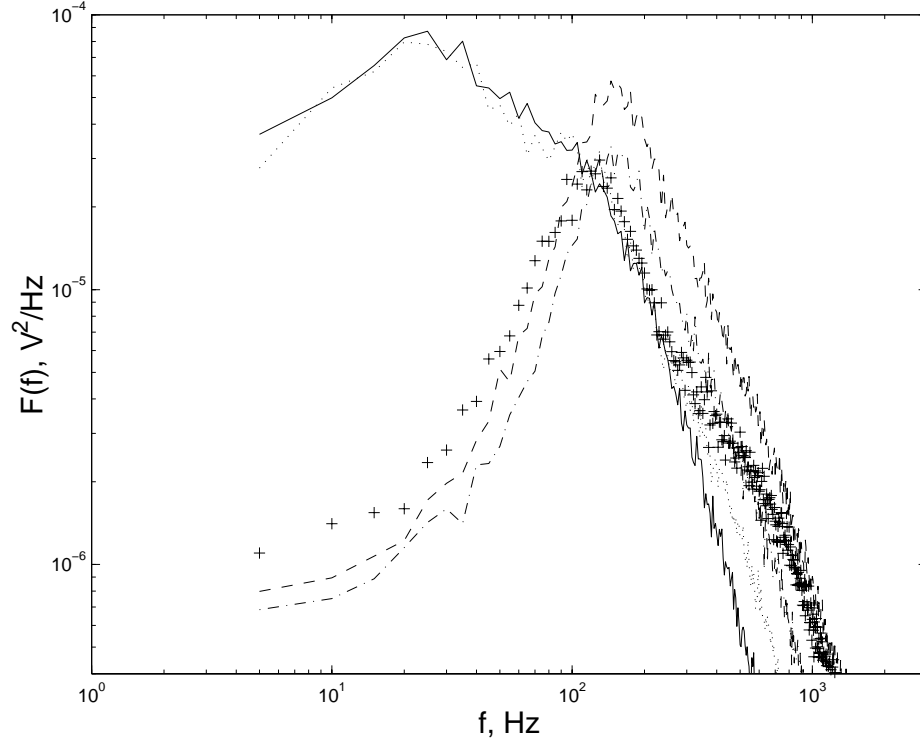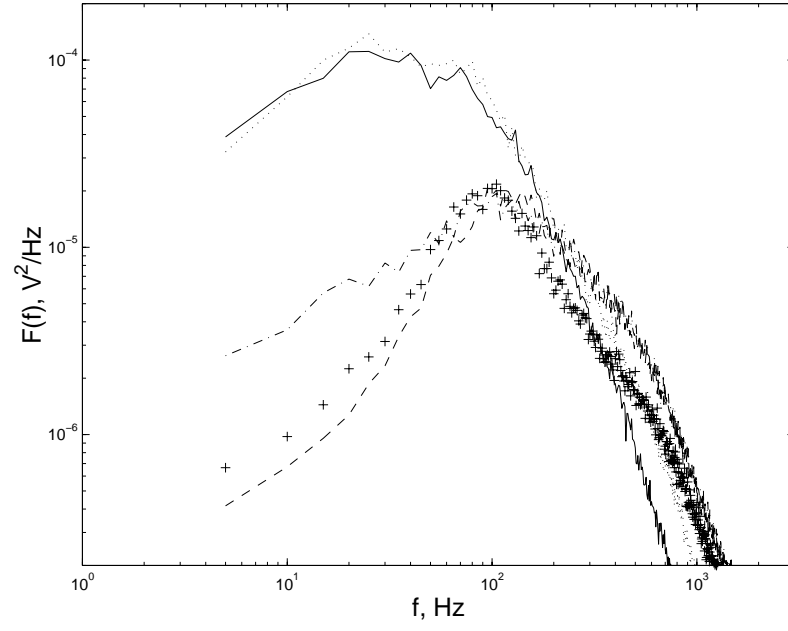
Figure 4.18: Spectra of wall pressure for jet-to-plate spacing H/D=4 measured at $-$ r/D=0.25, $\cdots$ r/D=0.5, -.- r/D=1, - - r/D=1.5, and + r/D=2
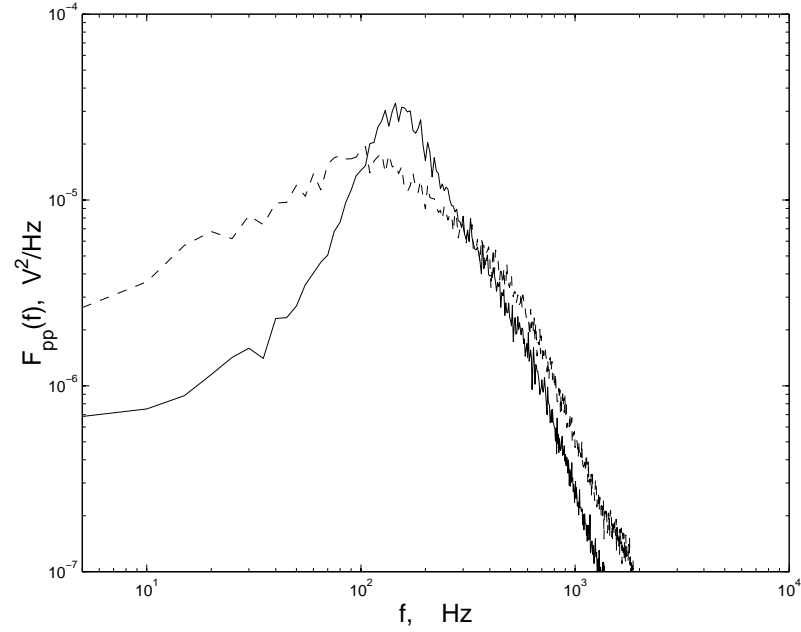
Figure 4.19: Comparison of pressure spectra at r/D=1 for jet-to-plate spacing $-$ H/D=2 and - - H/D=4.

seen in the H/D=2 case. The peak in the frequency spectrum again shifts between r/D=1.5 and r/D=2.0, suggesting that the ring vortices causing the peak at r/D=1.5 has undergone a transition similar to that for H/D=2.

The azimuthal correlation of the pressure measured at r/D=1, 1.5 and 2 for H/D=4 case are shown in Figure 4.20, and the azimuthal spectrum are shown in Figure 4.21. The pressure is correlated over a much smaller distance than for the H/D=2 case, indicating there are more small-scale motions. The azimuthal spectrum shows evidence of a peak at modes 3 and 4 at r/D=1 corresponding to the higher azimuthal mode structures observed in the jet shear layer by Citriniti[74]. A comparison of the azimuthal spectra measured for H/D=2 and H/D=4 shown in Figure 4.22 illustrates that the ring modes are not as dominate a structure for the H/D=4 case. It is clear from the azimuthal spectra that these structures appear to break down as they travel downstream as they do for the H/D=2 case, but this is a less distinct event.

Thus, the measurements indicate that the flow mechanism causing the secondary heat transfer peak for an impinging jet exiting the long pipe is similar to that for jet exiting the contoured nozzle. For larger jet-to-plate spacing a similar mechanism seems to cause the inflection in the heat transfer peak. The vortex rings break down as they evolve in the jet shear layer so this mechanism plays a less dominant role as the jet-to-plate spacing increases and there is a decrease in the secondary peak as H/D increases.

Reynolds Number Effect

The local Nusselt number distribution was measured for jets with Reynolds numbers ranging from 6,300 to 23,000. A comparison of the local Nusselt numbers is shown in Figure 4.23. It is clear that the local Nusselt number increases with Reynolds number, as expected. The secondary peak in Nusselt number becomes more pronounced as
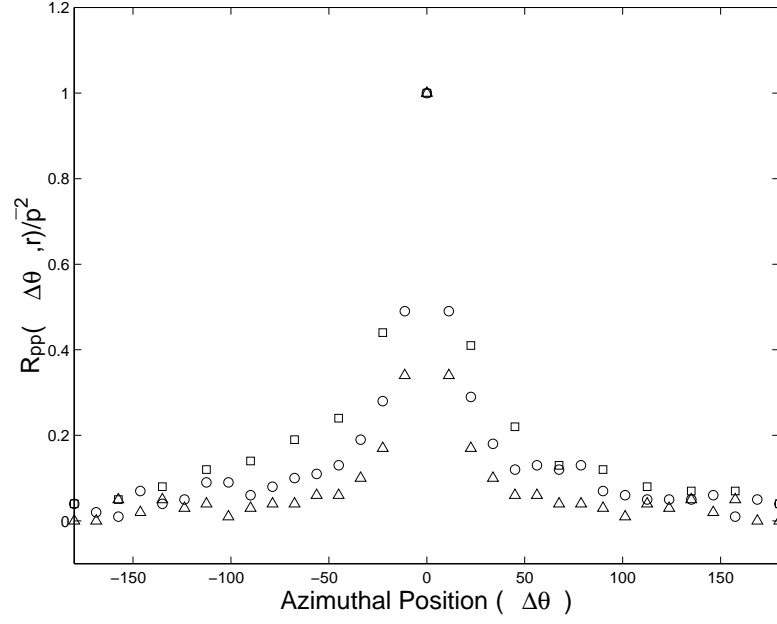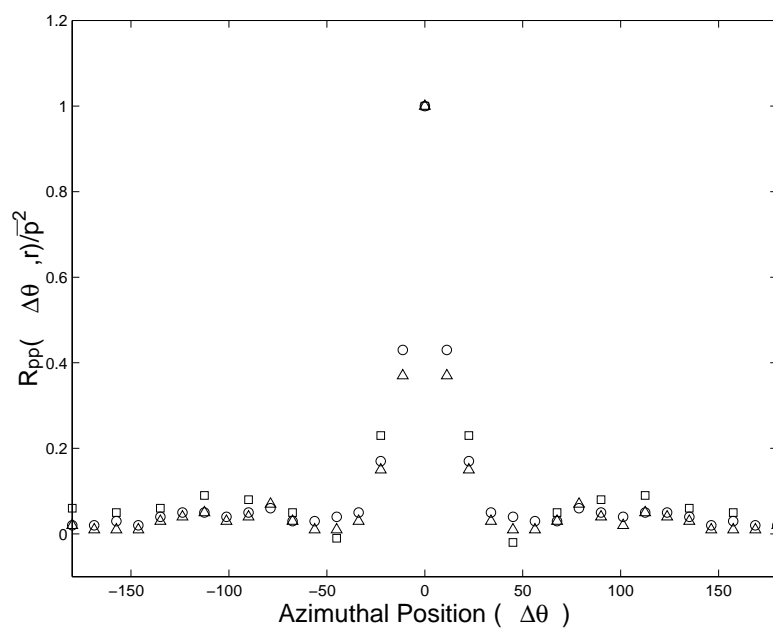
Figure 4.20: Azimuthal correlation of dynamic wall pressure for jet-to-plate spacing H/D=4 measured at □ r/D=1, ◯ r/D=1.5, and △ r/D=2.
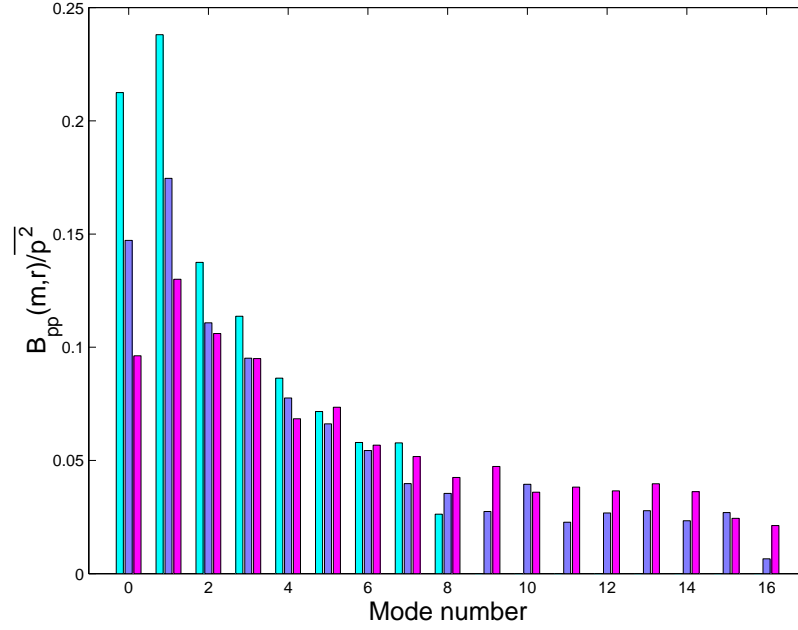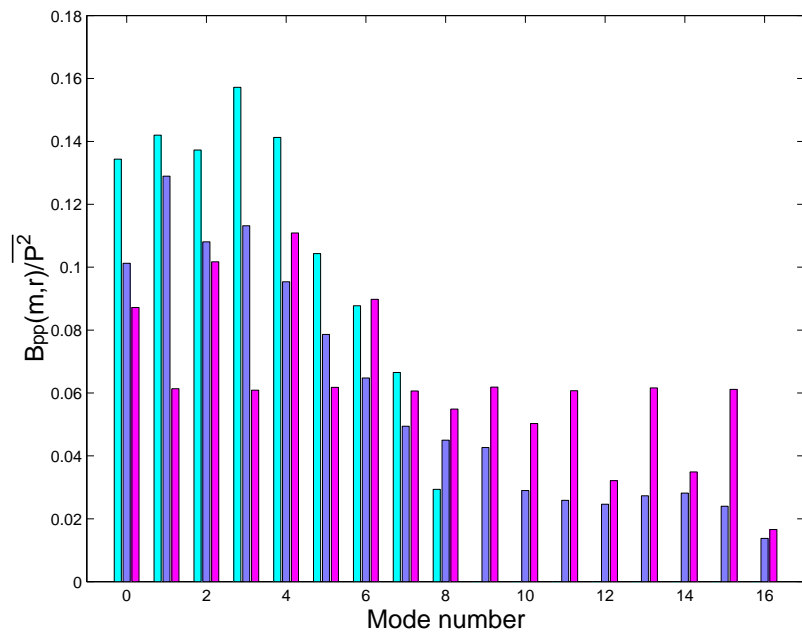

Figure 4.21: Azimuthal modal energy distribution for jet-to-plate spacing H/D=4, from left to right r/D=1, 1.5 and 2.
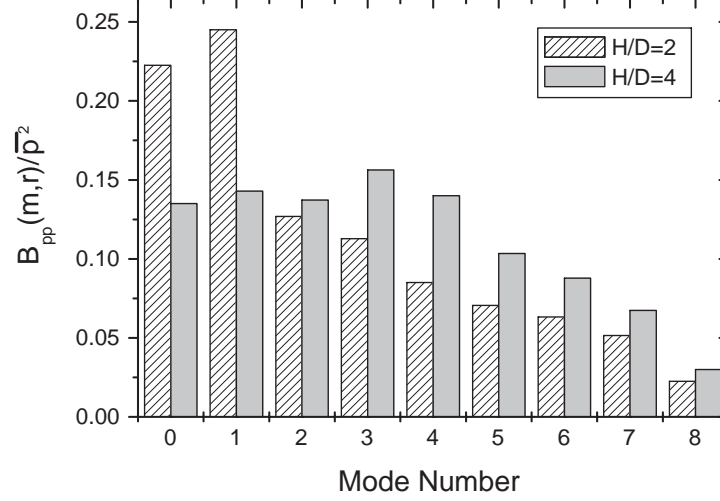
Figure 4.22: Azimuthal modal energy distribution at r/D=1 for jet-to-plate spacing H/D=2 and H/D=4

Reynolds number increases, but the location of the peak does not appear to change with the Reynolds number. This differs from the Nusselt number distribution for H/D=0.1, 0.5 and 1 measured by Lytle and Webb[37], indicating at large jet-to-plate spacing, the change in Reynolds number has little effect on the location of the vortex separation causing the secondary peak.

The local Nusselt number distributions were scaled using the correlation $Nu \propto Re^{0.7}$[25] as shown in Figure 4.24. The scaled results collapse reasonably well for Reynolds number greater than 15,400. There is a deviation near the centerline of the jet but the difference is less than 7%. The scaled results for Re$\leq$12,700 collapse reasonably well for r/D$\leq$1.5. The measurements at Re=12,700 collapse with the higher Reynolds number data for larger radii. The results for the two lower Reynolds number jets follow a different trend for r/D$\geq$1.5. These measurements have a significant smaller secondary peak and smaller heat transfer beyond r/D=2.
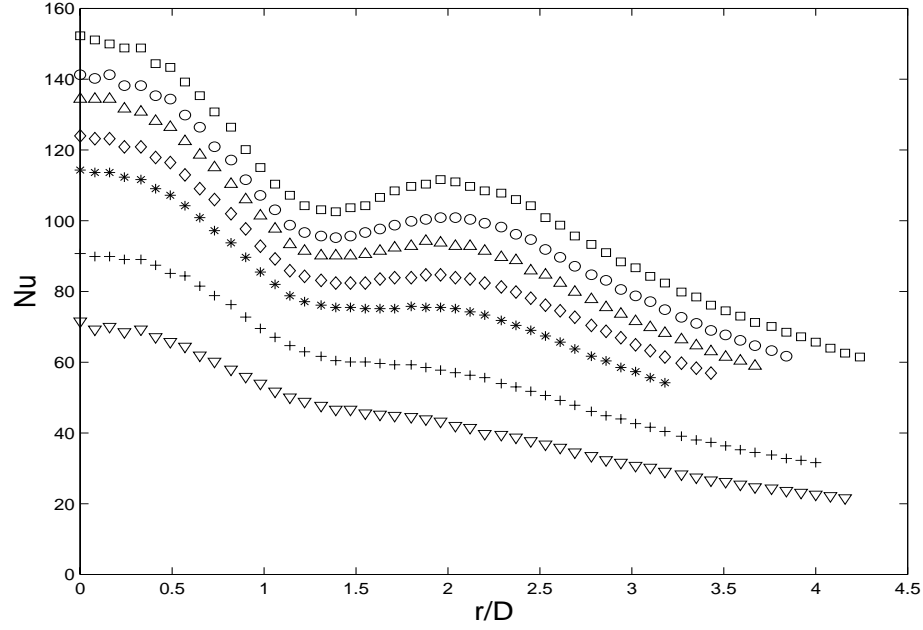
Figure 4.23: Local Nusselt number distribution for a jet-to-plate spacing H/D=2 with a Reynolds number of $\triangledown$ 6,300, $+$ 9,400, $*$ 12,700, $\diamond$ 15,400, $\triangle$ 17,800, $\bigcirc$ 20,300, and $\square$ 23,000.
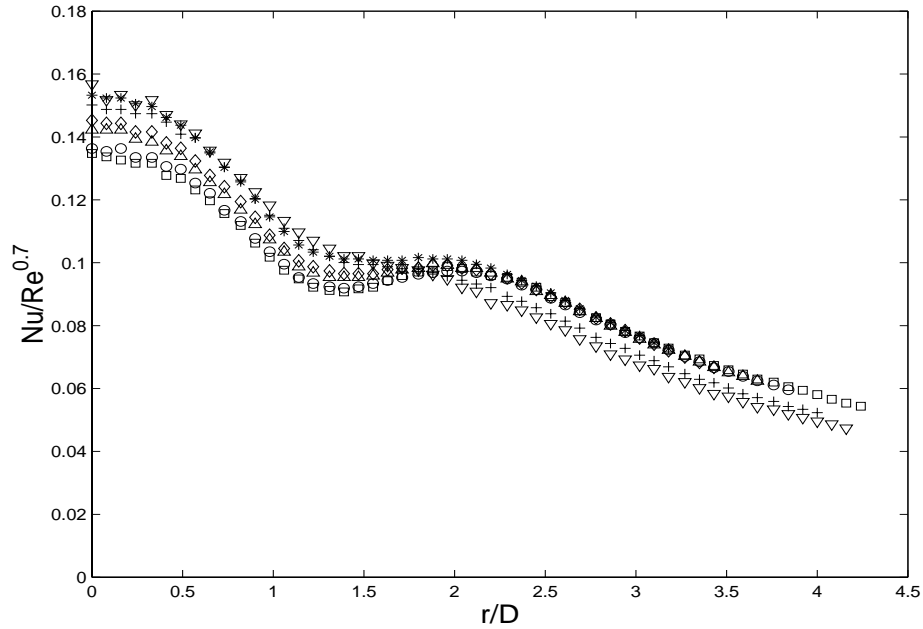
Figure 4.24: Local Nusselt number distribution $(Nu/Re^{0.7})$ at different Reynolds number for a jet-to-plate spacing H/D=2, symbols see the above figure

Effect of Confinement

Heretofore, there have not been any direct measurements of the effect of confinement
on the heat transfer produced by an impinging jet. Measurements have been done
on confined impinging jets but none have directly compared the heat transfer for a
confined and unconfined flow. A comparison of the Nusselt number distributions for
confined and unconfined jets exiting a long pipe with jet-to-plate spacings ranging
from H/D=0.25-4 are shown in Figures 4.25 and 4.26. It should be noted that the
local Nusselt numbers in these figures were computed using images acquired by a
frame grabber which yielded a lower resolution in temperature than the results in the
last section that were acquired manually, as discussed in the experimental procedure.
This results in the discrete steps in the figures, but a curve fit through this data will
be almost as accurate as the data in the previous section. As with all comparisons in
this investigation, the confined and unconfined measurement compared in these figures
were taken from consecutive measurements under the same conditions to ensure the
differences observed are caused by the confinement.

It is clear that the effect of confinement is the largest for the smallest jet-to-plate
spacing, H/D=0.25. In this case, the local Nusselt number was increased by up to
40%. The heat transfer enhancement decreases as the jet-to-plate spacing increases
and was not observed for H/D≥2. The local Nusselt number for small jet-to-plate
spacing was significantly reduced for larger radii r/D>2, with the largest effect being
observed again for H/D=0.25. This is not unexpected since the confinement limits the
entrainment of cold ambient air into the wall jet that would reduce the temperature
of the wall jet. This effect of the confinement also reduces with increasing jet-to-plate
spacing up to H/D=3.

The net effect of the confinement can be deduced by examining the distributions
of the average Nusselt number shown in the figures. It is apparent for all the near
impingement cases, H/D≤2, there is a region where the average Nusselt number

increased. For example, for H/D=0.25, the average Nusselt number increased by 25% for the region r/D≤1.6 while for H/D=2 the average Nusselt number increased by 7% over the region r/D≤1.5.

It is also apparent that the confinement has no significant effect on the heat transfer for larger jet-to-plate spacing of H/D=4 and 6. It should be noted that the plate used to confine the jet had a width of 32 diameters. This should be sufficiently large to ensure the effect of the finite boundary does not affect the development of the jet in the region studied. Thus, the results indicate that the confinement has little effect on the heat transfer from the impinging jet for jet-to-plate spacing greater than approximately 4 diameters.

The flow mechanism that causes the heat transfer enhancement for the small jet-to-plate spacing H/D≤2 is not fully understood. In their investigation, Colucci and Viskanta[32] suggested that the differences in the heat transfer measurements for confined orifices was caused by changes in the flow separation near the jet exit, but they did not perform any measurements of the flow to verify this conjecture. Two approaches were used here to investigate whether this was the cause of the heat transfer enhancement. Initially, flow visualization experiments were performed for the confined and unconfined cases. It was found, however, that the flow visualization technique utilized in this investigation did not yield useful results for the H/D=0.5 case. The results for the H/D=1.0 case did not show substantial difference.

Following this, measurements were taken of the mean and dynamic pressure on the impingement surface of the confined and unconfined jets. In all cases, the maximum difference between the mean pressure occurs at the centerline. The difference between the two case did not exceed 3% of the unconfined stagnation mean pressure, indicating the heat transfer enhancement was not caused by a change in the mean flow.

The variance of dynamic wall pressure for the confined and unconfined case for jet-to-plate spacing H/D=1 are shown in Figure 4.27, while a comparison of the pressure
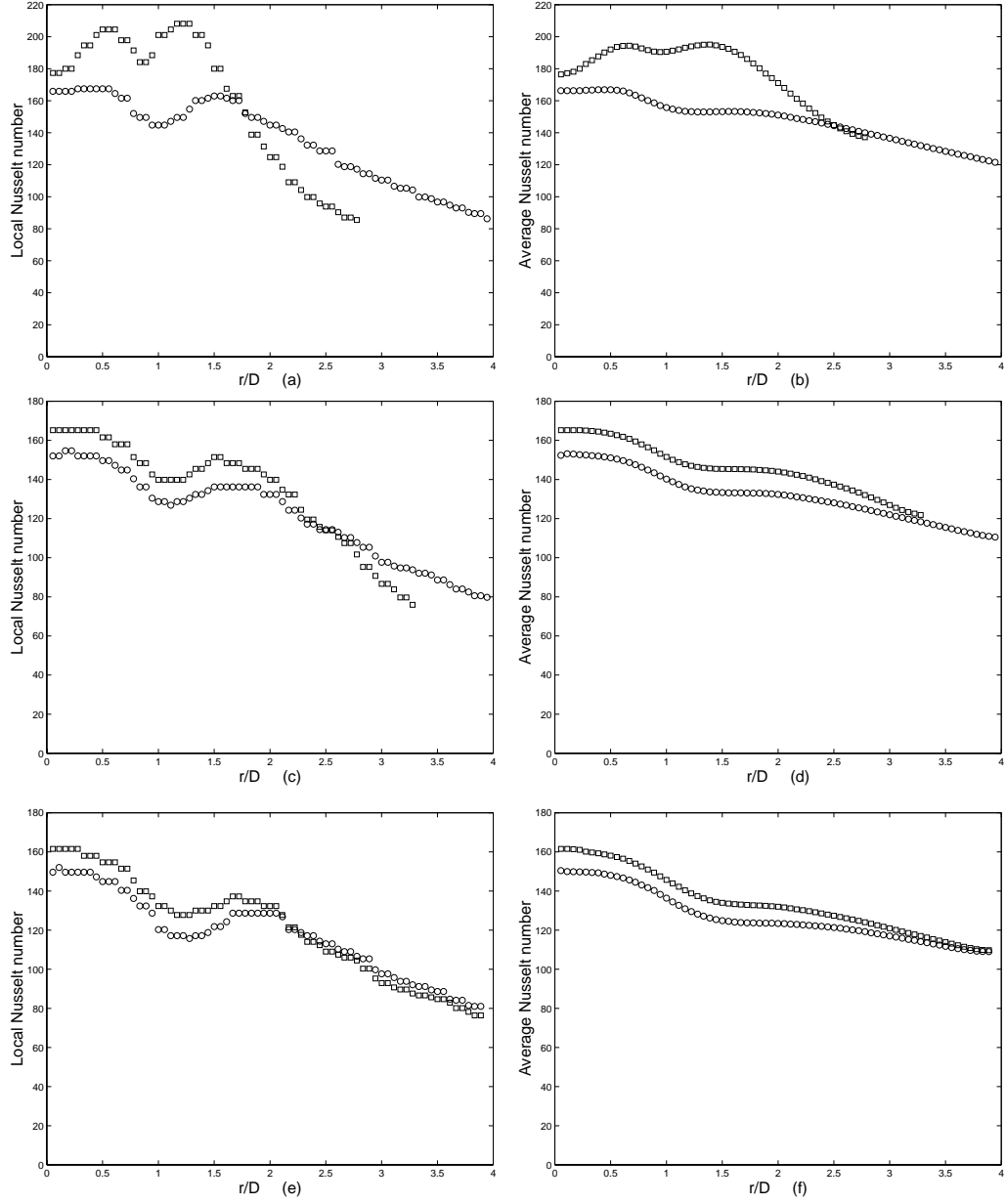
Figure 4.25: The Nusselt number distributions □ with and ◯ no confinement for Re=23,000, (a) the local Nusselt number for H/D=0.25, (b) the average Nusselt number for H/D=0.25, (c) the local Nusselt number for H/D=0.5, (d) the average Nusselt number for H/D=0.5, (e) the local Nusselt number for H/D=1, and (f) the average Nusselt number for H/D=1.
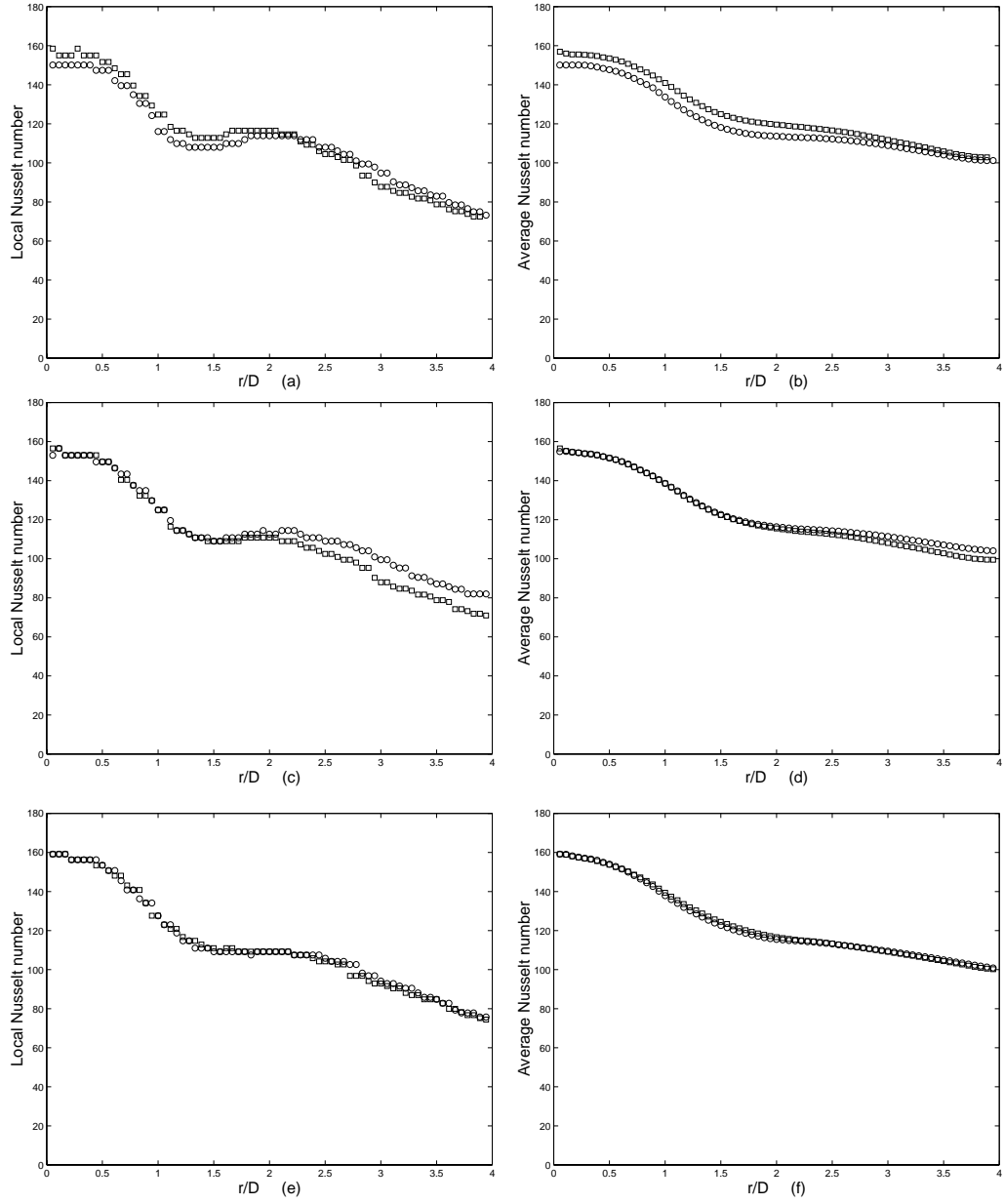
Figure 4.26: The Nusselt number distributions □ with and ◯ no confinement for Re=23,000, (a) the local Nusselt number for H/D=2, (b) the average Nusselt number for H/D=2, (c) the local Nusselt number for H/D=3, (d) the average Nusselt number for H/D=3, (e) the local Nusselt number for H/D=4, and (f) the average Nusselt number for H/D=4.
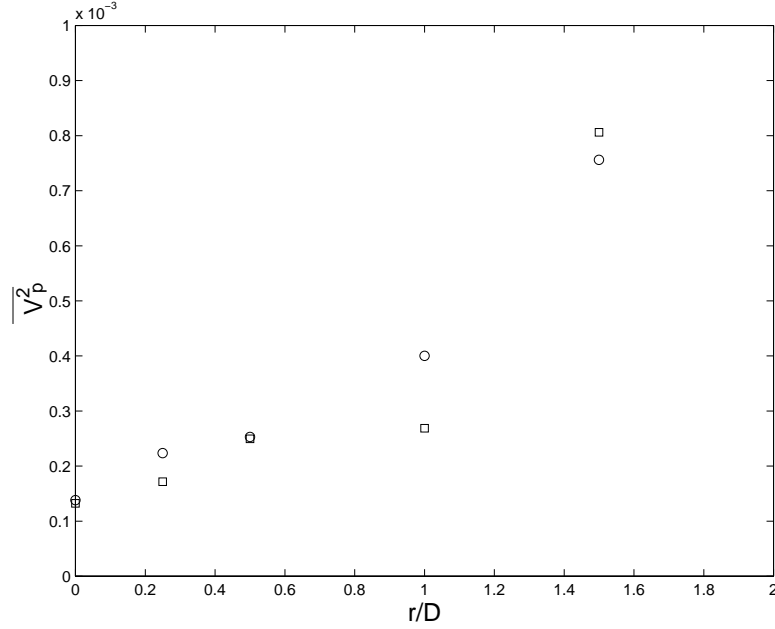
Figure 4.27: Distribution of the dynamic pressure variance measured in □ unconfined and ◯ confined impinging jet for a jet-to-plate spacing H/D=1.

spectra at the radial locations r/D=0-1.5 is shown in Figure 4.28. It is clear that the dynamic pressure fluctuations on the impingement plate surface are significantly increased at certain locations due to the effect of confinement. In particular, there is 30% increase in the mean square dynamic pressure at r/D=0.25 and 50% increase at r/D=1. The location r/D=0.25 is within the potential core of the jet, so the increase in the pressure fluctuations here is most likely caused by an increased intermittency or the oscillation of the large-scale structures in the shear layer. The increase at r/D=1 seems to be associated with an increase in the strength of the ring vortices.

The turbulence level for the confined case drops below the unconfined case at r/D=1.5, the position before the flow separation in the unconfined wall jet. This suggests confinement affects the development of the large-scale ring structure which seems to lead to the heat enhancement in the near stagnation region.
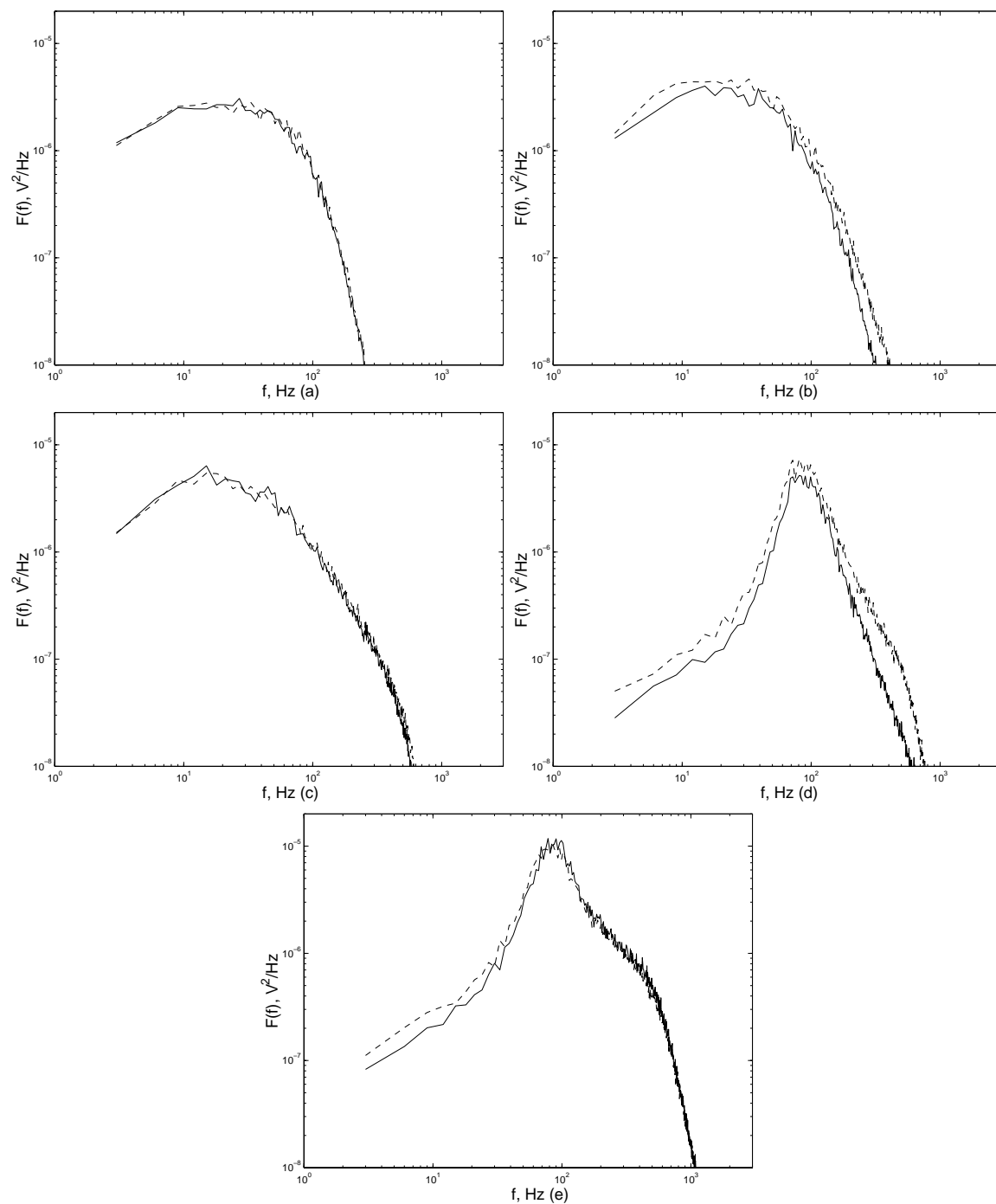
Figure 4.28: Spectra of dynamic wall pressure for − unconfined and - - confined impinging jet for Re=23,000 measured at a jet-to-plate spacing H/D=1, (a)r/D=0, (b)r/D=0.25, (c)r/D=0.5, (d)r/D=1, (e)r/D=1.5.
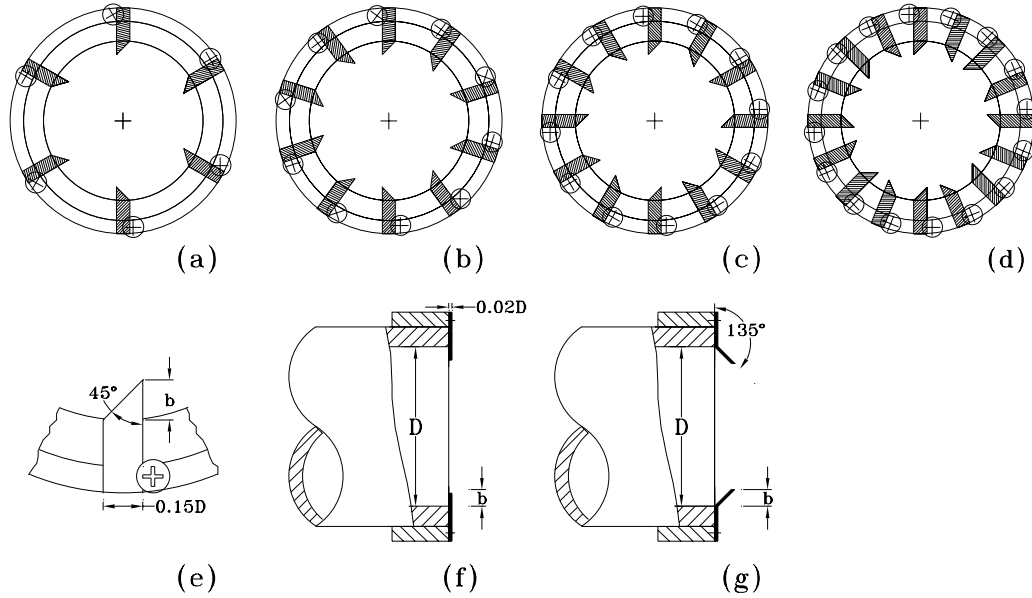
Figure 4.29: Sketch of tabs used in modifying impinging jet flow structure, (a) six tabs, (b) ten tabs, (c) twelve tabs, (d) sixteen tabs, (e) tab geometry, (f) straight tab configuration, (g) 45° bent tab configuration. Tab height b=0.06D, 0.1D and 0.15D.

4.3   Heat Transfer Enhancement Using Tabs

Two different methods of enhancing the heat transfer in the impinging jet were studied. In the first, 45° delta tabs were used to enhance the mixing in the jet in order to enhance the heat transfer on the impingement surface. The tabs in this investigation were constructed using 0.254mm-thick shim stock. The tabs that are 8.5mm long and 1.9mm wide, were held in place using screws on a sleeve that slid over the end of the pipe. The sleeve was designed so that the length of the tabs protruding into the flow could be easily modified from 0.06D to 0.15D. Investigation were performed using six, ten and sixteen tabs as shown in Figure 4.29. The adjacent tabs were positioned in the opposite direction to create a pair of counter rotating vortices. The tabs on a later test were also bent at a 45° angle to the mean flow.

The heat transfer enhancement caused by the tabs was determined by measuring
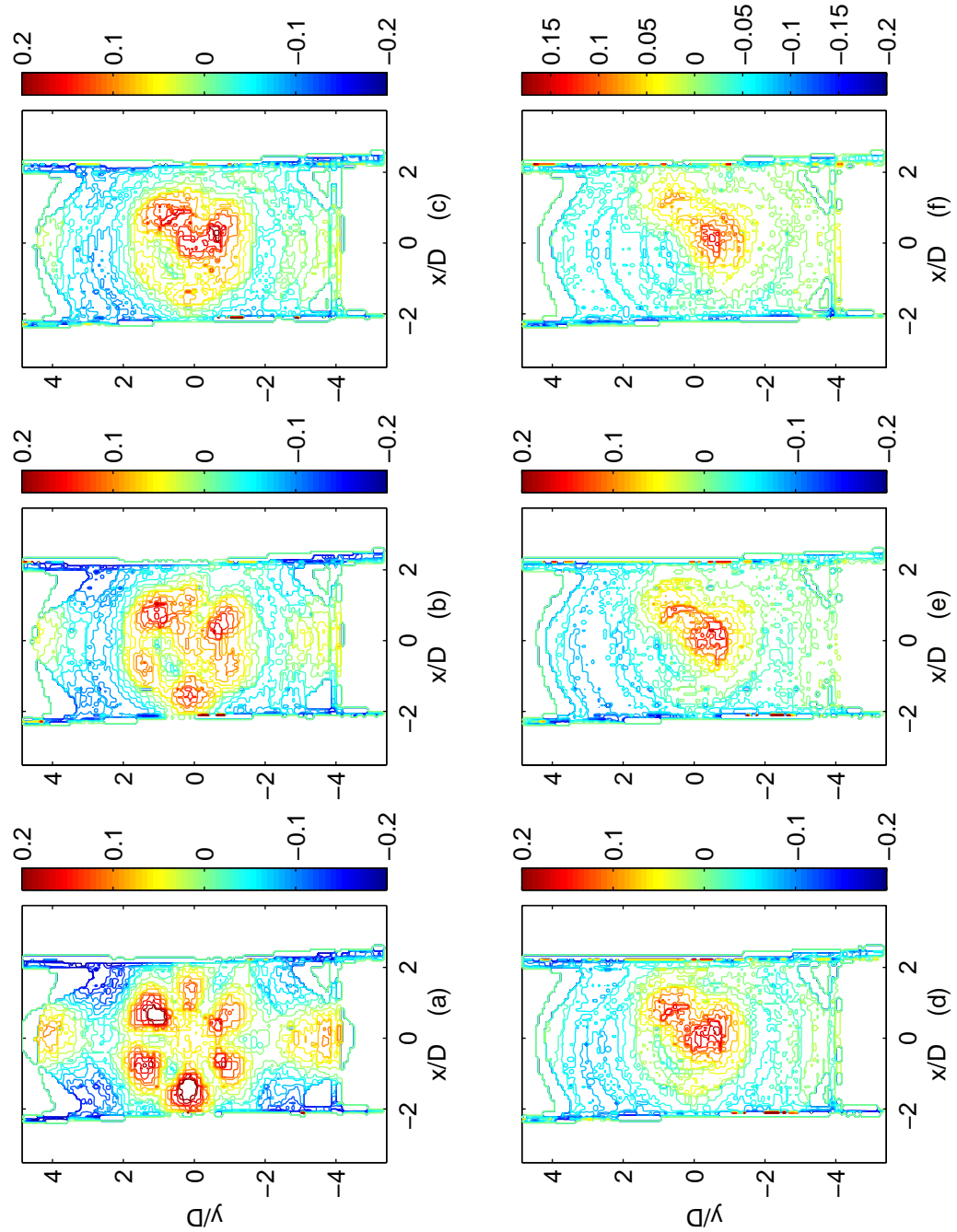
Figure 4.30: Distributions of heat transfer enhancement factor η for the six b=0.1D tabs case for Re=23,000 measured at (a) H/D=2, (b)3, (c)4, (d)5, (e)6, and (f)7. Tab position shown in Figure 4.29(a).

the heat transfer with and without tabs for the same heat flux and jet temperature in consecutive measurements. The enhancement of the heat transfer was characterized using an enhancement factor given by

$$\eta = \frac{Nu_{tab}}{Nu_{no\ tab}} - 1. \tag{4.3}$$

Investigations were performed to examine the effect of changing the number of tabs and different tab geometries. The heat transfer enhancement generated using these tabs is presented first. Following this, flow visualization and velocity measurements of the effect of the tabs is presented.

The distributions of heat transfer enhancement for six tabs inserted 0.1D into the flow at jet-to-plate spacings of $2 \leq H/D \leq 7$ are shown in Figure 4.30. For H/D=2, there are six regions of heat transfer enhancement surrounding the impingement region. Further away from the centerline, there are six alternative regions of heat transfer enhancement and reduction. It will be shown later using velocity measurements that the inner heat transfer regions correspond to the gaps between two adjacent tabs indicating that these regions are caused by the blockage of the tabs. The alternating regions of the heat transfer enhancement and reduction are caused by the effect of the counter rotating vortices, generated by the tabs, traveling along the plate. For large jet-to-plate spacing, there is a large amount of mixing so the effect of the high-speed regions generated by the tabs is not as obvious. There is a slight enhancement in the heat transfer at the centerline for H/D=6 caused by enhanced mixing and turbulence in the core of the jet.

The average Nusselt number computed for these cases is shown in Figure 4.31. The small jet-to-plate spacings have better overall heat transfer rate inside r/D=4. It should also be noted that the peak in the stagnation heat transfer now occurs at H/D=5 not H/D=6. This is not unexpected since the enhanced mixing caused by the tabs will reduce the development length of the jet.
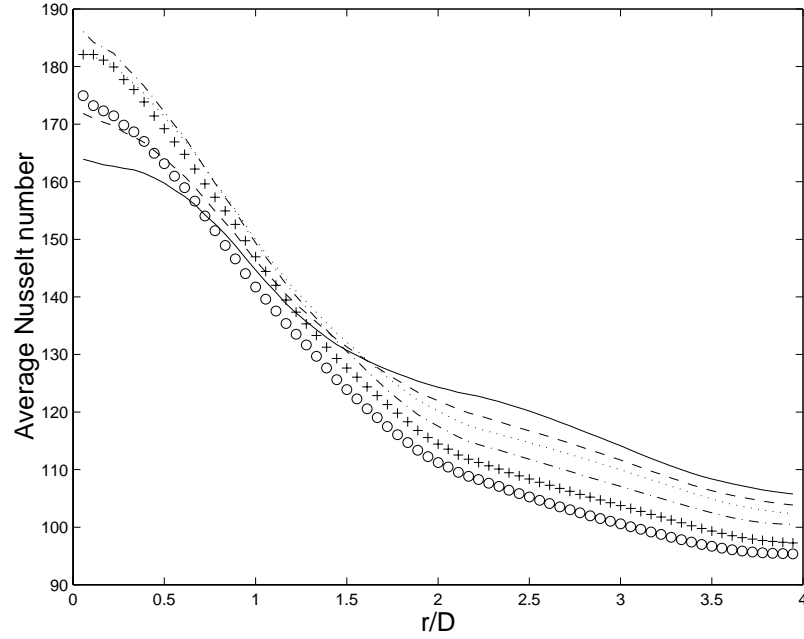
Figure 4.31: Distributions of average Nusselt number with six 0.1D tabs at various jet-to-plate spacings for Re=23,000 measured at − H/D=2, - - 3, ··· 4, -.- 5, + 6, and ⃝ 7.

A comparison of the heat transfer enhancement produced by jets with six, ten and sixteen tabs inserted 0.1D into the flow for jet-to-plate spacings of H/D=2, 4 and 6 are shown in Figure 4.32 and 4.33. For the shortest distance, H/D=2, the heat transfer is significantly enhanced for all three tab arrays. The ten and sixteen tab arrays only create five and eight enhancement regions respectively. This differs from the six tab array that produced six regions of heat transfer enhancement, indicating that the mechanism causing the heat transfer enhancement for the six tab array differs from the ten and sixteen tab arrays. This was confirmed using velocity field measurement discussed later.

For large jet-to-plate spacing, H/D=4 and 6, the heat transfer enhancement for the three sets of tabs are very similar. The regions of heat transfer enhancement in the inner part of the jet, r/D≤2, have merged together forming a region where the
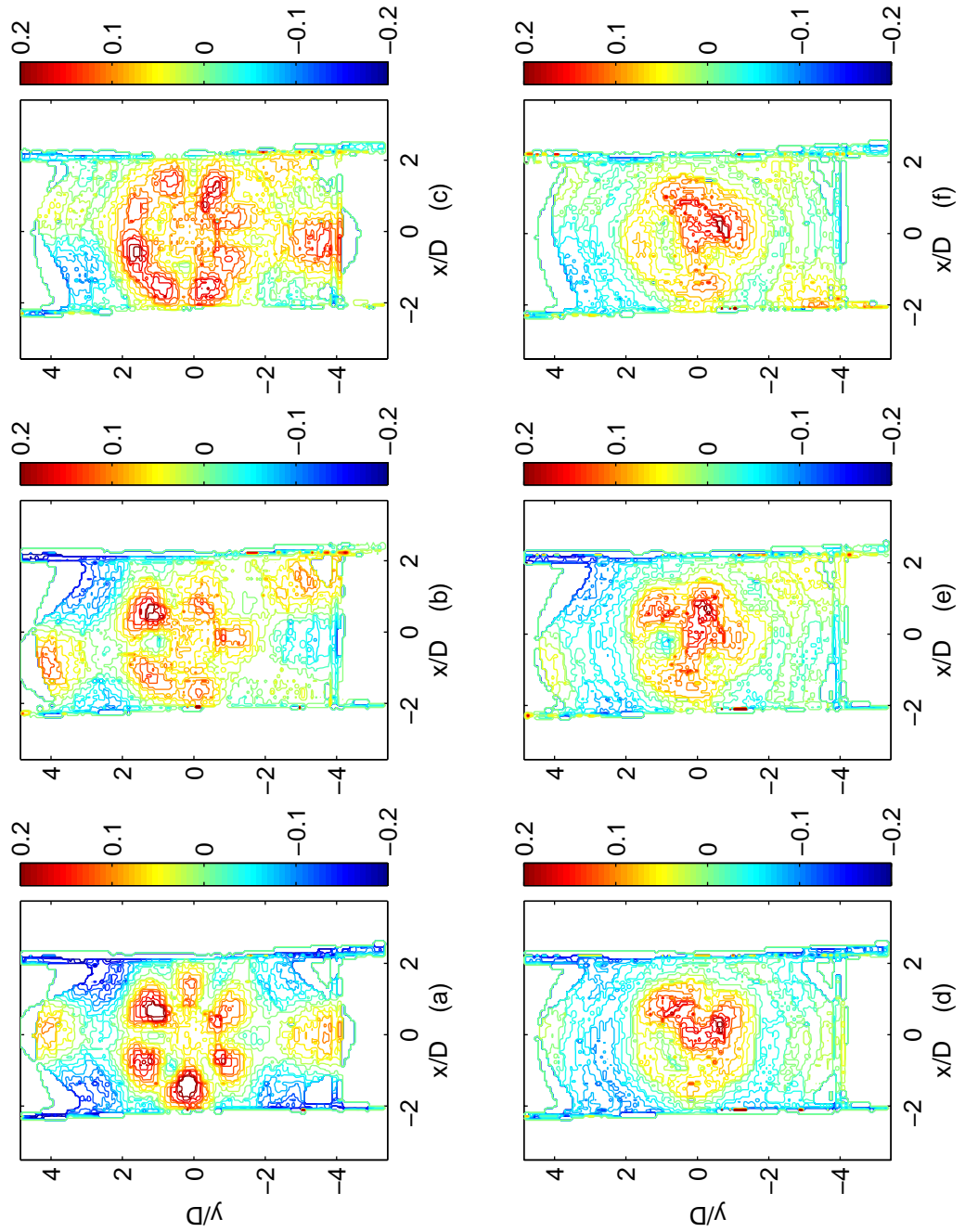
Figure 4.32: Distributions of heat transfer enhancement factor η for Re=23,000, (a) 6 tabs, H/D=2, (b) 10 tabs, H/D=2, (c) 16 tabs H/D=2, (d) 6 tabs H/D=4, (e) 10 tabs H/D=4, and (f) 10 tabs H/D=4. Tab length 0.1D, tab position shown in Figure 4.29.
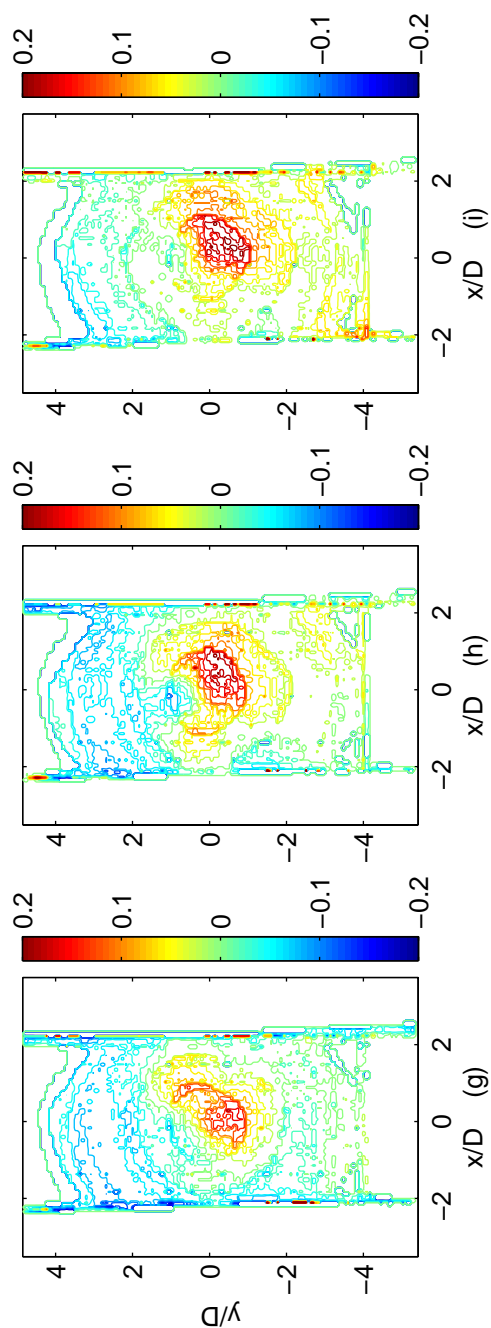
Figure 4.33: Distributions of heat transfer enhancement factor η for Re=23,000, (g) 6 tabs, H/D=6, (h) 10 tabs, H/D=6, (c) 16 tabs, H/D=6. Tab length 0.1D, tab position shown in Figure 4.29.

heat transfer is significantly enhanced by 20% or more. The tabs have a smaller effect outside of this impingement region suggesting that the major effect of the tab is to enhance the mixing in the jet before it impinges on the plate rather than changing the heat transfer on the plate.

A comparison of the average Nusselt numbers for the three different tab arrays for jet-to-plate spacing H/D=2, 4 and 6 are shown in Figure 4.34-4.36. In all cases, the Nusselt number for the sixteen tab array is the largest over almost the entire region. The enhancement in the average Nusselt number is approximately 8-10% over the entire region considered for H/D=2. For the larger impingement distance, there is an over 10% increase in the heat transfer in the stagnation region but this decreases significantly so that the enhancement for an area with a radius of three diameters is only 4-5%. Thus, for applications with large jet-to-plate spacings, the tabs are most effective over small regions around stagnation point.
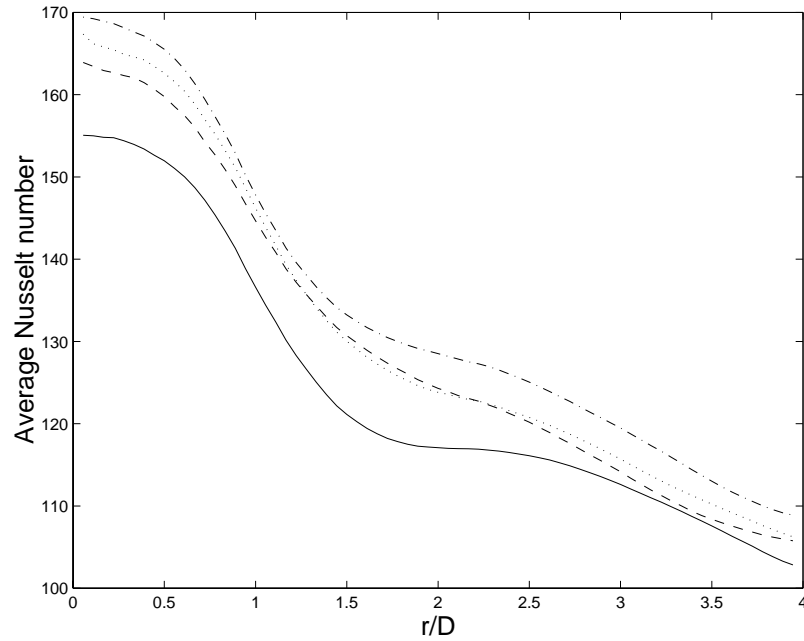
Figure 4.34: Distributions of average Nusselt number for Re=23,000 measure at H/D=2 − without tab, - - 6 0.1D tabs, ··· 10 0.1D tabs, -··- 16 0.1D tabs.
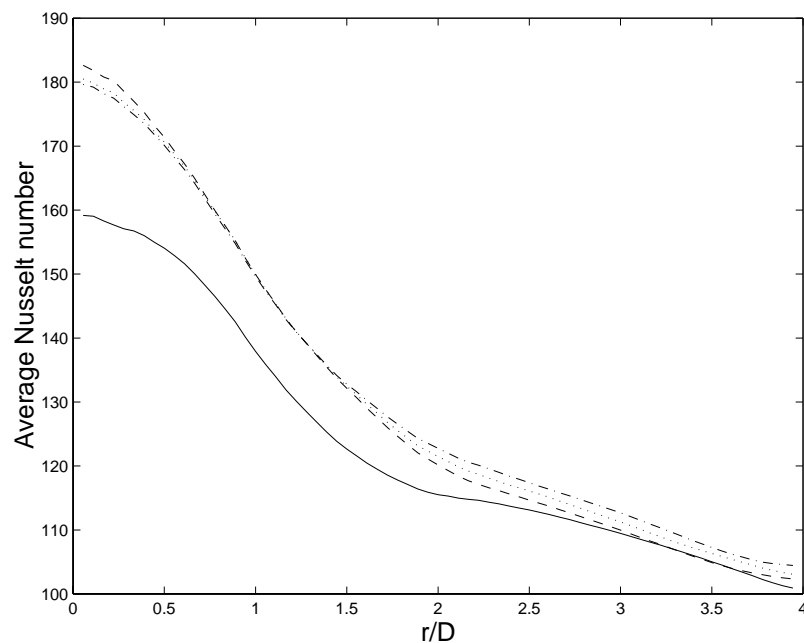
Figure 4.35: Distributions of average Nusselt number for Re=23,000 measure at H/D=4 − without tab, - - 6 0.1D tabs, ⋯ 10 0.1D tabs, -·- 16 0.1D tabs.
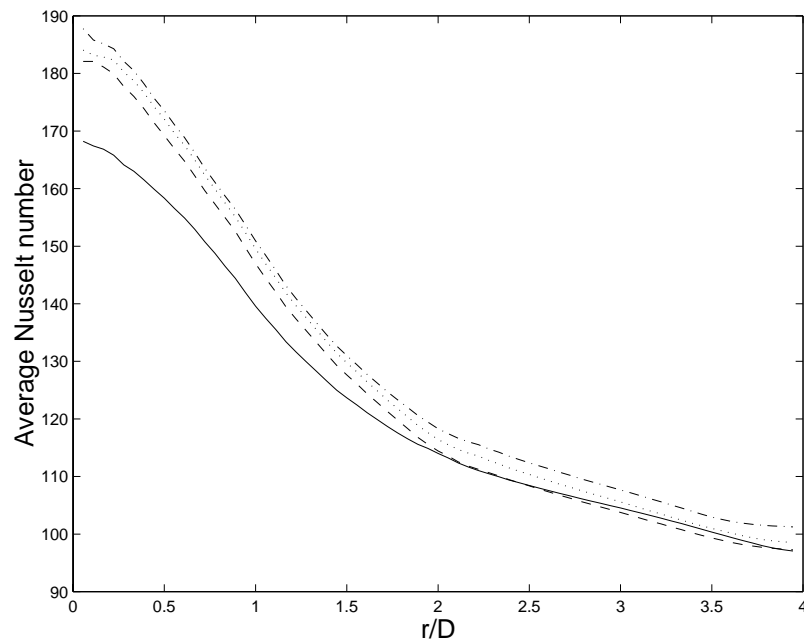
Figure 4.36: Distributions of average Nusselt number for Re=23,000 measure at H/D=6 − without tab, - - 6 0.1D tabs, ⋯ 10 0.1D tabs, -·- 16 0.1D tabs.

Figure 4.37: Evolution of stagnation Nusselt number with jet-to-plate spacings. □ plain nozzle, ◯ six 0.1D tab array, △ ten 0.1D tab array, and ◊ sixteen 0.1D tab array

It should be noted that one of the effects of utilizing the tabs is to enhance the mixing and reduce the length of the potential core of the impinging jet. The stagnation heat transfer as a function of H/D for the three different tabs is shown in Figure 4.37. In all cases the peak in the heat transfer associated with the end of the jet potential core has shifted to smaller H/D. This effect is most significant for the six tab array, where the peak has move to H/D=4-5. For sixteen tab array the peak only moves to H/D=5-6. Thus, it is not clear whether comparing the heat transfer from the different tab arrays at a fixed H/D is the most appropriate because this is comparing jets at different stages of development. This question should be examined in more detail in the future.

The height of the tabs in the flow will change the magnitude of their effect on the flow and hence heat transfer enhancement. The heat transfer enhancement produced by the ten tab array with tab heights of b/D=0.06, 0.10, and 0.15 was examined here.

Note that for this Reynolds number the ratio of the inner length scale in the pipe, η^+, to the diameter is 7.67×10^{-3}. Thus, the length of these tabs in wall units are $b^+ = b/\eta^+ = 7.8$, 13.0, and 19.6 respectively. The distribution of the heat transfer enhancement characterized using heat transfer enhancement factor, η, for H/D=2 and H/D=4 is shown in Figure 4.38. It is clear that the heat transfer enhancement is largest for the longest tabs. This is not unexpected since these tabs produce the largest streamwise vortices and largest blockage effects so these tabs would have the most significant effect on the development of the jet. Increasing the tab height seems to be the most pronounced effect for the near impingement case. This can be better characterized using the distributions of the average Nusselt number shown in Figure 4.39 - 4.41. It is clear that for the small distance, H/D=2, the largest tab height b/D=0.15 yields the highest overall Nusselt number in the entire region studied here. Increasing the tab height from 0.10D to 0.15D has produced an additional 5-10% heat transfer enhancement so that the enhancement over the plain jet is 10-15% over the region considered. The further enhancement in the heat transfer is caused by the stronger vortices shed from the larger tabs and somewhat by the larger tabs increasing the blockage. The larger tabs would increase the blockage which leads to a 3.4% average velocity increase for b/D=0.10 and 8.0% for b/D=0.15.

For the intermediate impingement distance, H/D=4, the largest tab array b/D=0.15 yields the highest average Nusselt number, as expected. Near the centerline, the heat transfer is enhanced 9.0% compared to the b/D=0.1 tab array and 21.8% compared to the plain jet. This is caused by the enhanced mixing from the streamwise vortices shortening the length of the potential core to 4∼5 diameters and increasing the turbulence intensity in the core of the jet. The average Nusselt number distribution for b/D=0.06 tab array is very similar to that from the plain nozzle, suggesting that they have not had a significant effect on the development of the shear layer.

The effect of the tab arrays is less pronounced for the jet-to-plate spacing H/D=6,
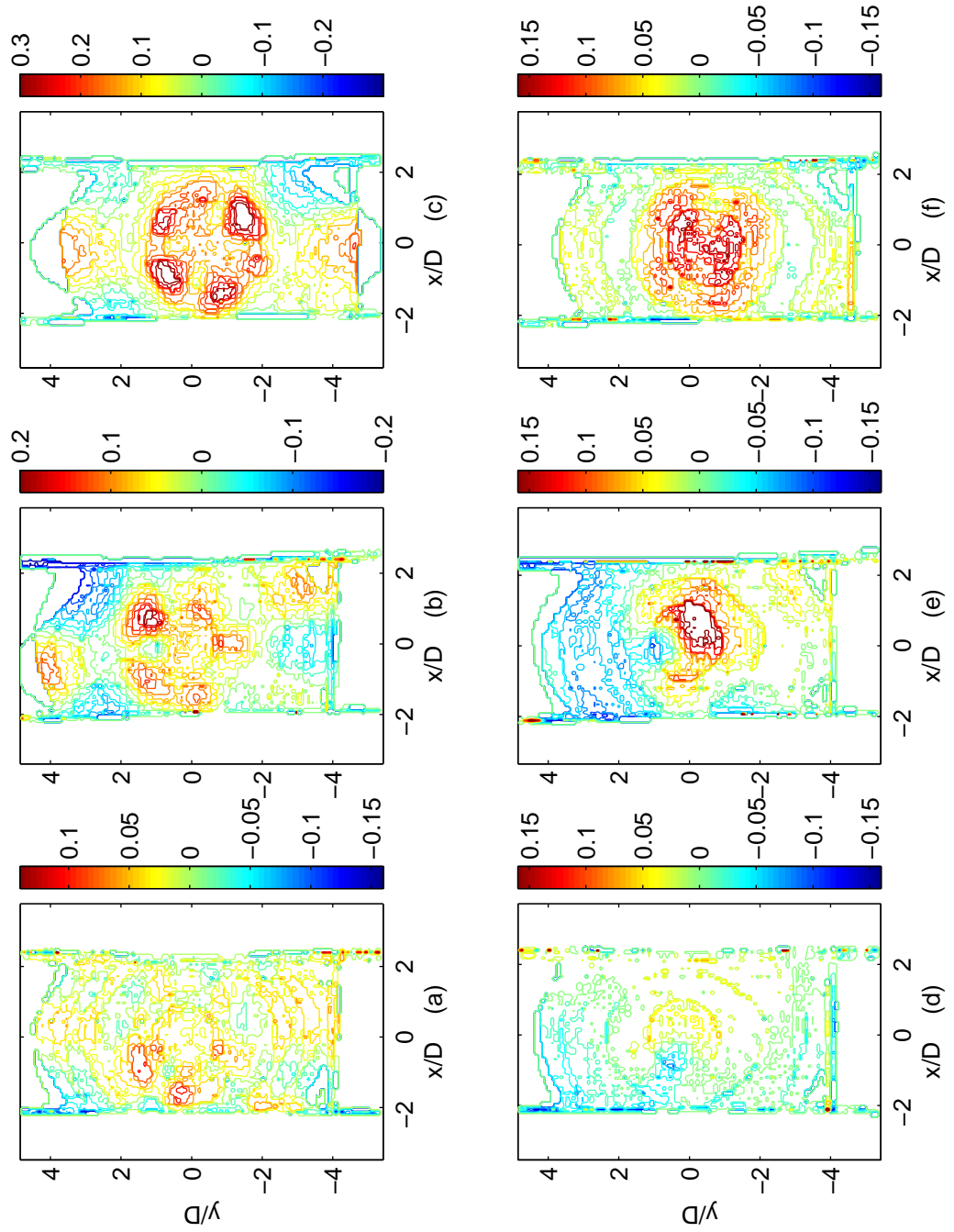
Figure 4.38: Distributions of heat transfer enhancement factor η for ten straight tab array for Re=23,000, (a) b/D=0.06, H/D=2, (b) b/D=0.1, H/D=2, (c) b/D=0.15 H/D=2, (d) b/D=0.06, H/D=6, (e) b/D=0.1, H/D=6, (f) b/D=0.15, H/D=6. Tab position shown in Figure 4.29(b).
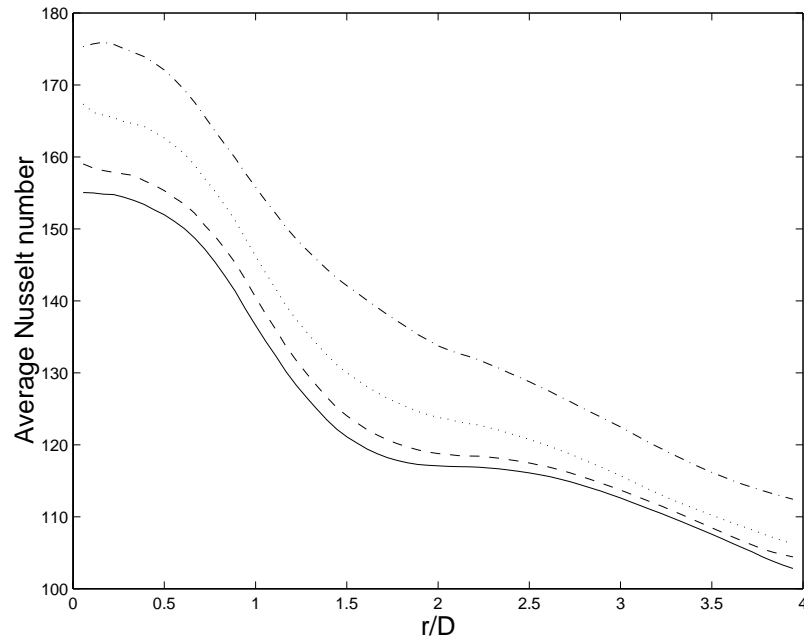
Figure 4.39: Distributions of average Nusselt number at H/D=2 with ten tab array of various height for Re=23,000, − without tab, - - b/D=0.06, ⋯ b/D=0.1, -·-b/D=0.15.
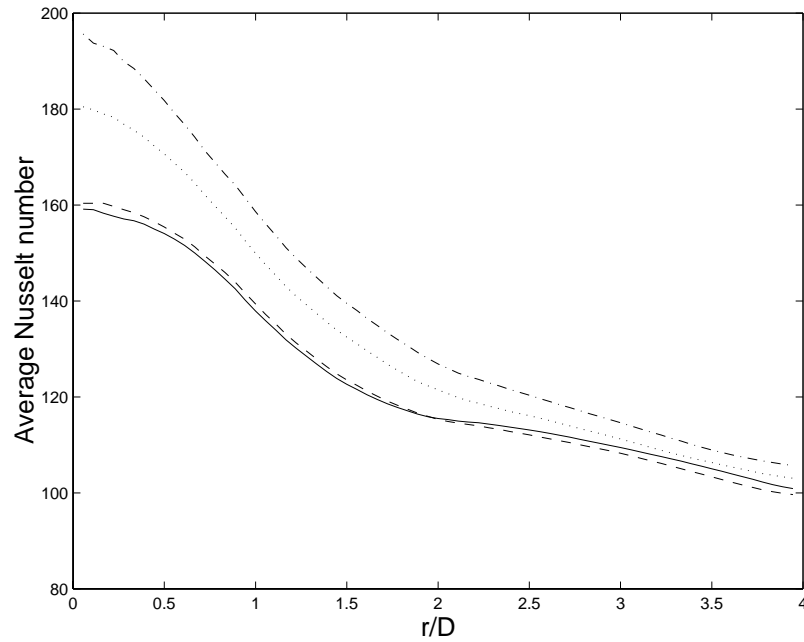
Figure 4.40: Distributions of average Nusselt number at H/D=4 with ten tab array of various height for Re=23,000, − without tab, - - b/D=0.06, ⋯ b/D=0.1, -·-b/D=0.15.
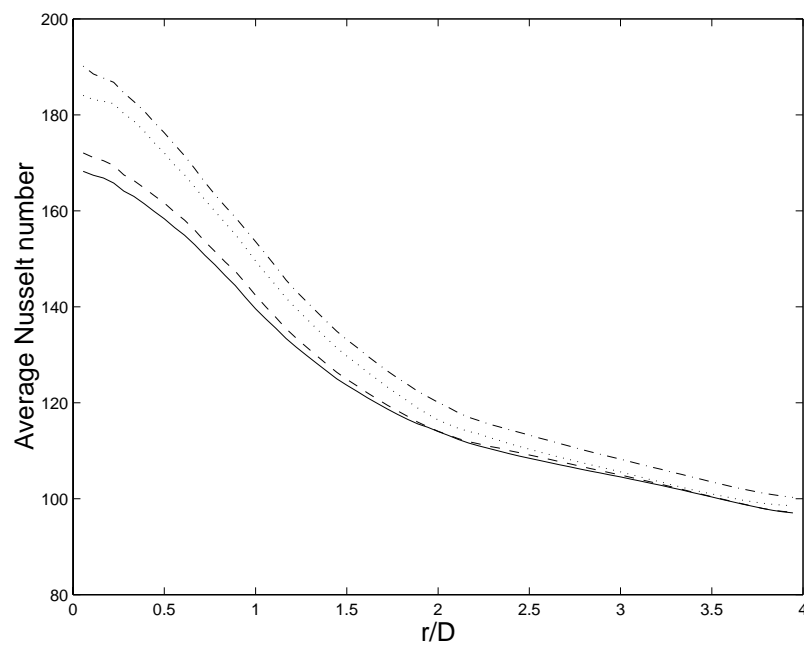
Figure 4.41: Distributions of average Nusselt number at H/D=6 with ten tab array of various height for Re=23,000, − without tab, - - b/D=0.06, ··· b/D=0.1, -·-b/D=0.15.
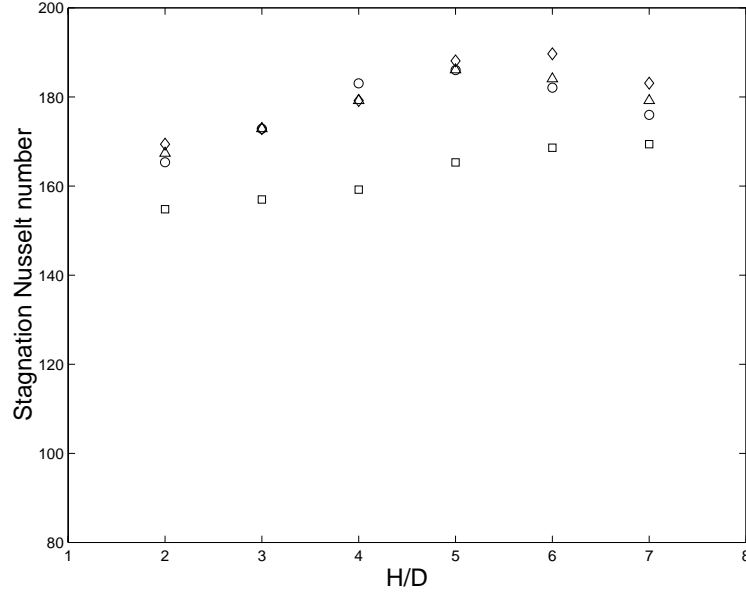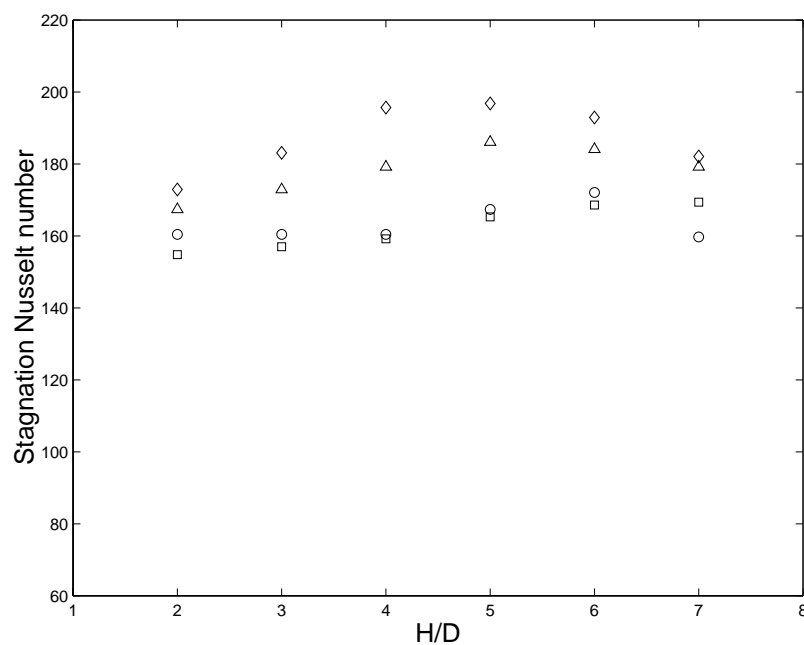

Figure 4.42: Evolution of stagnation Nusselt number with jet-to-plate spacings. □ plain nozzle, ◯ ten 0.06D tab array, △ ten 0.1D tab array, ◇ ten 0.15D tab array.

in part because the tabs have significantly shortened the development length of the jet. Thus, while the impingement distance H/D=6 corresponds to the end of the potential core in the plain jet, it now corresponds to a point beyond the potential core for the jets with tabs. This can be clearly seen in Figure 4.42 that includes the stagnation heat transfer as a function of impingement distance for the three tab heights. This is similar to the results deduced for the different number of tabs in the array but it is clear that the shortening of the potential core becomes more pronounced with tab height.

The strength of the vortices shed by the tabs can also be changed by angling the tabs relative to the flow. The effect of angling the tabs was examined for a base case of b/D=0.1 for the ten tab array. A comparison between the average Nusselt number for tabs angled at 45° relative to the flow and the straight tabs for H/D=2, 4 and 6 are shown in Figure 4.43. The angled tabs produce a 3-4% increase in the heat transfer for the near impingement cases. For the larger impingement cases, the angled tabs produce a smaller enhancement in the heat transfer.

Flow Measurement

The measurement of the heat transfer enhancement caused by the six, ten, and sixteen tab arrays suggested that the six tab array affected the flow differently than the ten and sixteen tab arrays. In particular, the shortest impingement distance measurements showed six regions of heat transfer enhancement for the six tab case but only five and eight regions of heat transfer enhancement for the ten and sixteen tab arrays. Thus, there is a heat transfer enhancement region associated with each tab for the small number of tabs and one region for every two tabs for the larger arrays. The flow field produced by an array of six tabs and twelve tabs was investigated on the larger scale impinging jet facility. Although it may be better to perform experiments with a tab array documented more completely in the heat transfer measurement, twelve
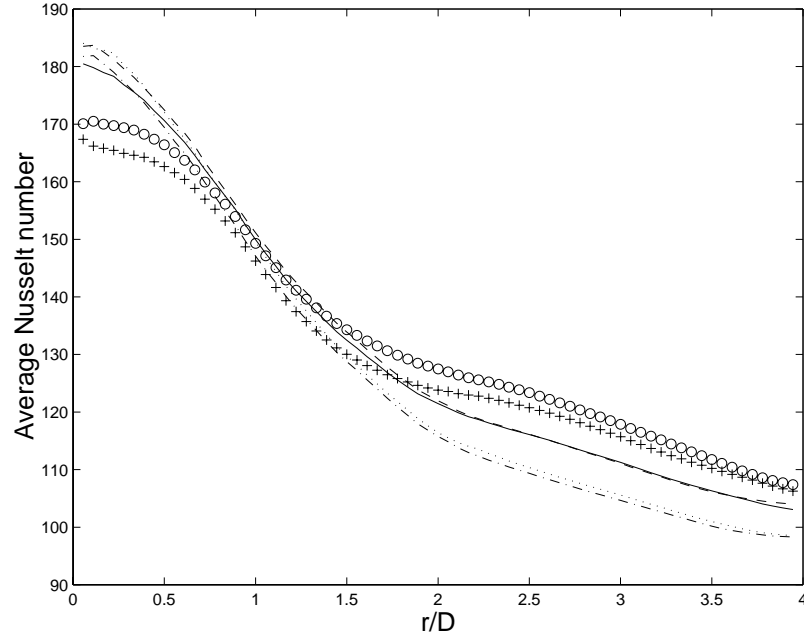
Figure 4.43: Comparisons of the average Nusselt number of ten b/D=0.1 45° angled tab array and straight tab array for H/D=2, 4 and 6 for Re=23,000, + H/D=2 straight, ◯ H/D=2 angled, − H/D=4 straight, - - H/D=4 angled, ⋯ H/D=6 straight, -·· H/D=6 angled.

tabs was chosen so a single tab array holder could be constructed for the two cases. Preliminary measurements of the twelve tab array not presented in the thesis showed that the twelve tab array did produce six regions of heat transfer enhancement.

Initially, flow visualization experiments were performed in the plain impinging jet and the impinging jet with the six and twelve tab arrays for a jet-to-plate distance of H/D=2. Images of the flow field on the plane Z/D=0.5 downstream of the jet exit are shown in Figure 4.44 and 4.45 for a Reynolds number of 9,300. Although the Reynolds number is considerably lower than the Reynolds number used in the heat transfer studies, the images should give a qualitative understanding of the effect of the tabs. In these images, the jet is fully seeded with smoke so that the light regions are the fluid that has exited the jet.

It is clear that in both cases the tabs cause strong azimuthal variations in the shear
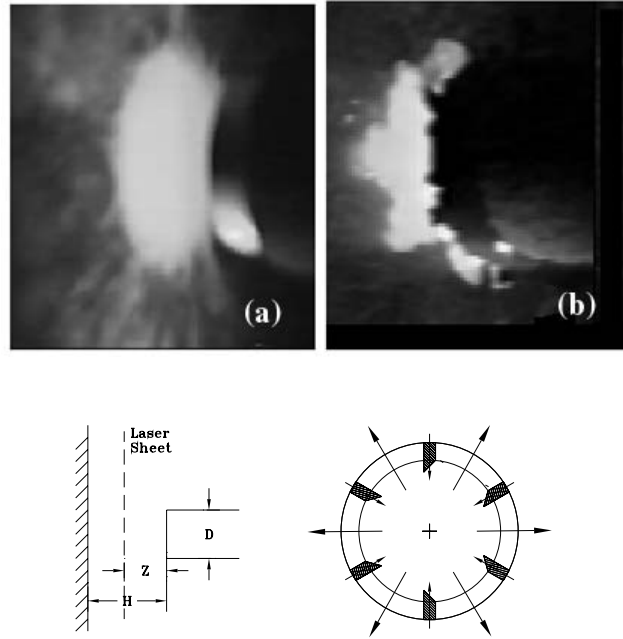
Figure 4.44: Cross-sectional view of (a) plain nozzle case and (b) six tab array case for Re=9,300 at H/D=2, Z/D=0.5, .
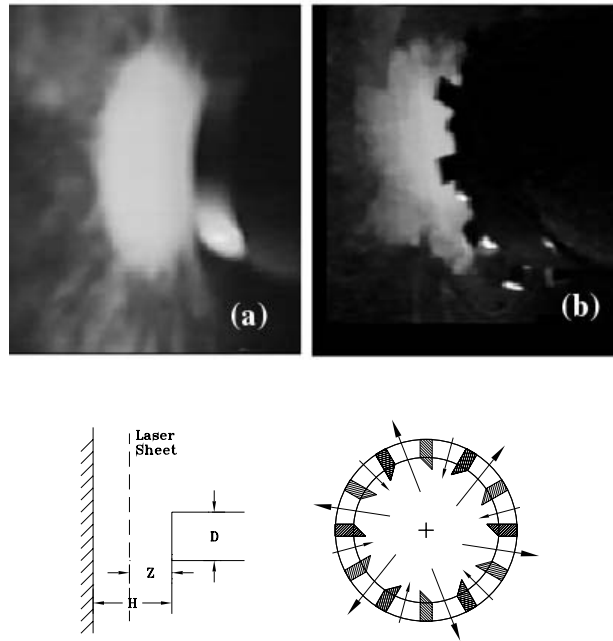
Figure 4.45: Cross-sectional view of (a) plain nozzle case, (b) twelve tab array case for Re=9,300 at H/D=2, Z/D=0.5.

layer between the jet and the ambient air indicating that the tabs are enhancing the mixing between the jet and ambient. The mechanism causing the mixing is clearly different, because each tab array is creating roughly the same number of azimuthal undulations. Although the other side of the shear layer is not visible in these images, it was clear during the visualization that both devices produced six azimuthal undulations. The outflow of fluid for the six tab array seems to be associated with gaps between two adjacent tabs. The outflow of jet fluid for the 12 tabs array seems to only occur at the six larger gaps. This is not unexpected since the undulations near the nozzle exit are caused primarily by the blockage of the tabs.

Images of the flow field at distance Z/D=1.5 downstream of the jet exit with the six tab array for jet-to-plate spacing H/D=2 and Re=9,300 are shown in Figures 4.46. There are again six alternative regions of more and less flow rate in the far field
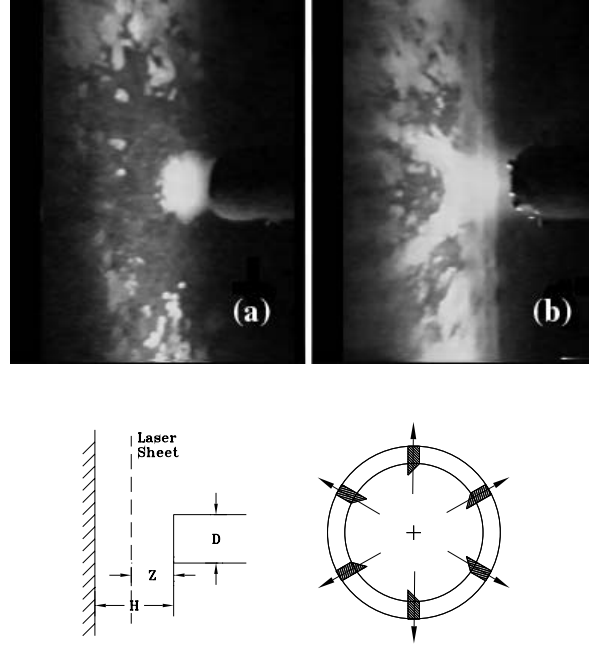
Figure 4.46: Cross-sectional view of (a) plain nozzle case, (b) six tab array case for H/D=2, Z/D=1.5, Re=9300.

from the centerline in the images, but the directions of these undulations seem to

be different from those at Z/D=0.5. Thus, the six fast moving regions of flow will cause six regions of enhancement of heat transfer. This agrees well with the heat transfer measurements. The image for the 12 tab array case does not show the flow distribution on the impingement plate, so it was not included here.

Measurements of the velocity field were performed in the free jet with tabs using a hot wire anemometer to confirm the results of the flow visualization. The velocity for six tab array was measured on a grid at Z/D=0.5, 1.5, and 3.0. The contours of the measured velocity normalized by the centerline velocity in the jet without the tabs are shown in Figures 4.47, 4.48 and 4.49.

The measurements of the mean velocity at Z/D=0.5 and Z/D=1.5 show evidence of six regions of high speed flow that correspond to the locations observed in the heat transfer measurements. The size of these regions and strength of peak decreases as the flow evolves downstream, indicating the effect of the tabs would likely be more pronounced for nearer impingement distance. The measurements show that the peaks are positioned between the tabs suggesting these regions of high-speed flow are associated with blockage caused by the tabs.

A comparison of the velocity measurements for the six tab array and the twelve tab array at Z/D=0.5 is shown in Figures 4.47 and 4.50. It is clear that the twelve tab array does produce six high speed regions around the jet. The size of the deviations are not as large as those caused by the six tab array. This explains why the peaks in the heat transfer are not as distinct for this case.
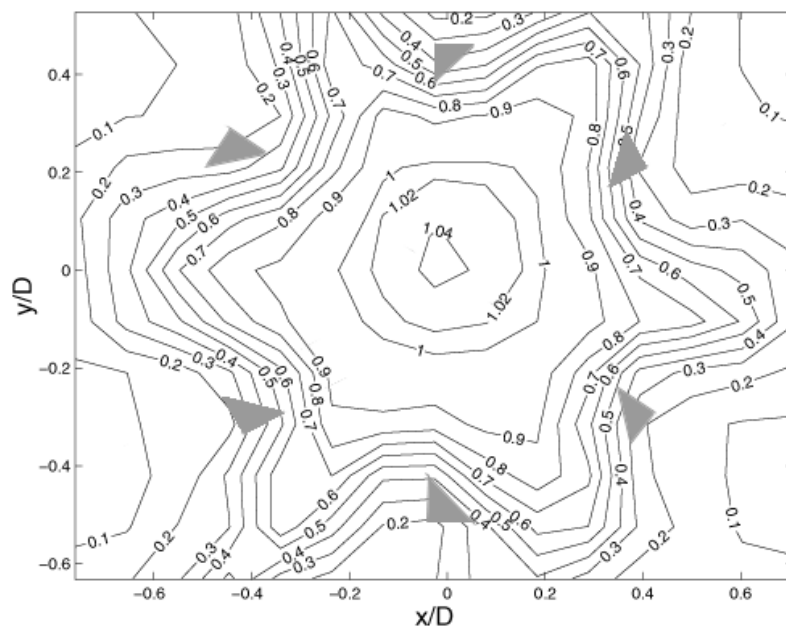
Figure 4.47: Mean streamwise velocity distribution with six tab array at Z/D=0.5 for Re=23,500, normalized by the centerline mean velocity at exit of the plain nozzle, tab arrangement (a) in Figure 4.29, b=0.1D.
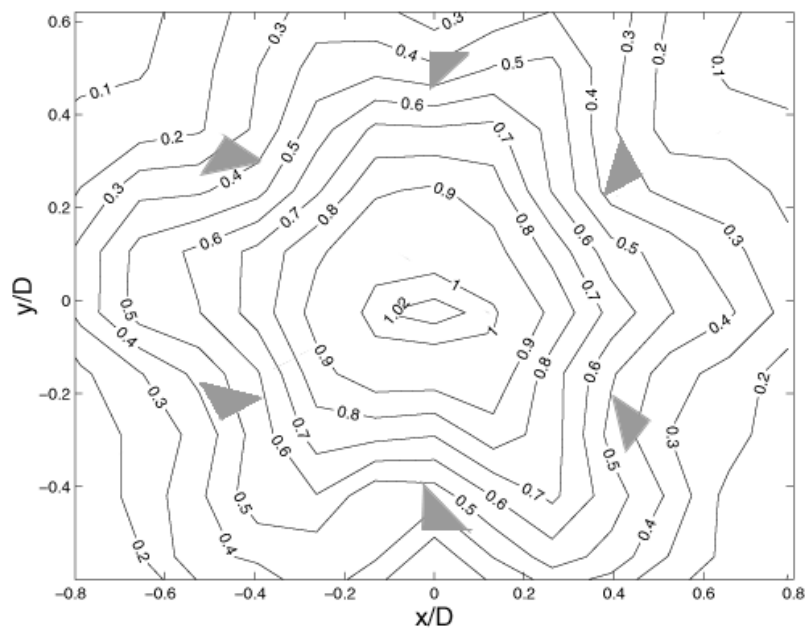
Figure 4.48: Mean streamwise velocity distribution with six tab array at Z/D=1.5 for Re=23,500, normalized by the centerline mean velocity at exit of the plain nozzle, tab arrangement (a) in Figure 4.29, b=0.1D
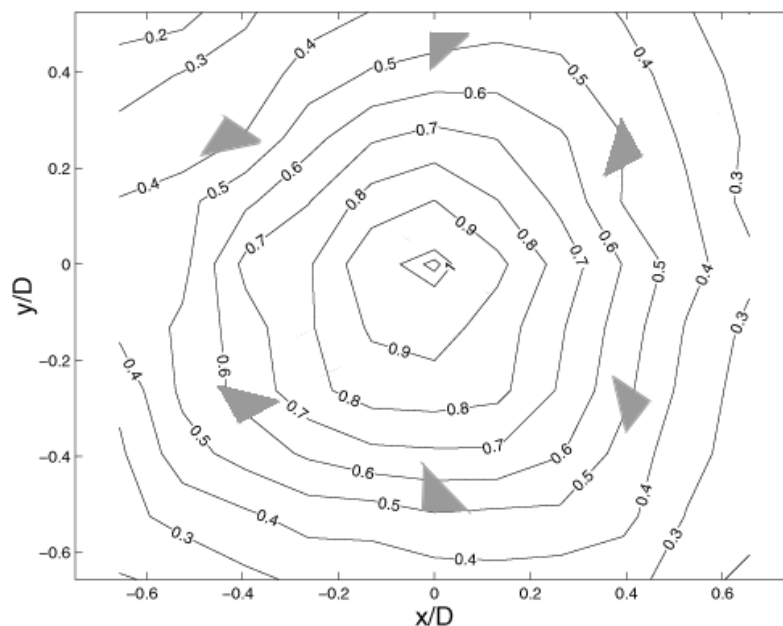
Figure 4.49: Mean streamwise velocity distribution with six tab array at Z/D=3 for Re=23,500, normalized by the centerline mean velocity at exit of the plain nozzle, tab arrangement (a) in Figure 4.29, b=0.1D.
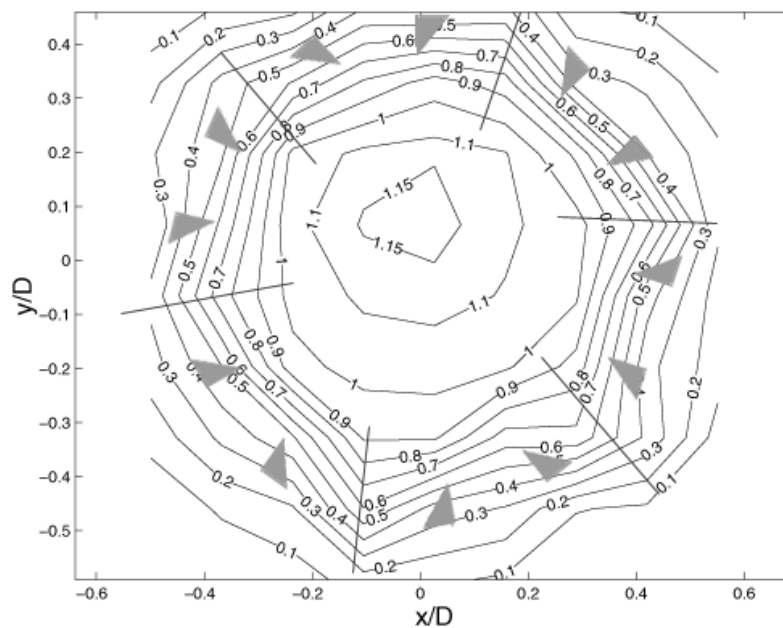
Figure 4.50: Mean streamwise velocity distribution with twelve tab array at Z/D=0.5 for Re=23,500, normalized by the centerline mean velocity at exit of the plain nozzle, tab arrangement (a) in Figure 4.29, b=0.1D.

4.4 Heat Transfer Enhancement Using Concentric Trip Array

In the second case, an array of trips over the impingement surface was used to enhance the heat transfer. The geometry and arrangements of the trip array are shown in Figure 4.51. The trip array consists of four concentric rings with inner diameter
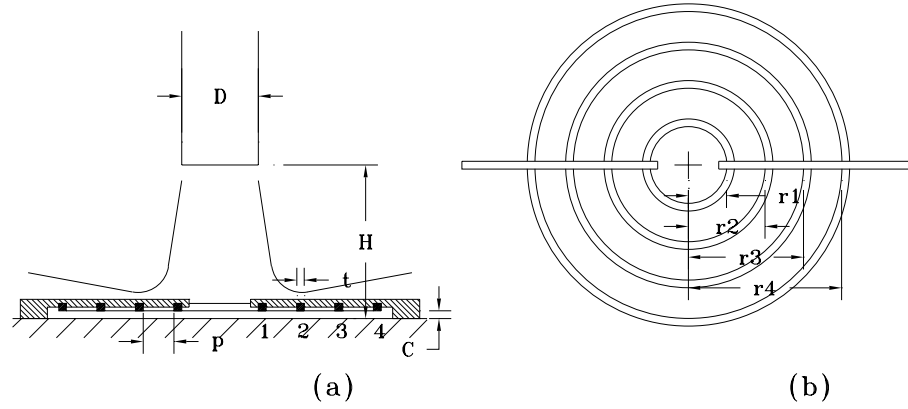
Figure 4.51: Sketch of concentric trips array, (a): side view, (b): top view; t/D=0.1, C/t=0.50, 1.14 and 1.62; r_1/D=0.5, r_2/D=1, r_3/D=1.5, r_4/D=2

$d_1 = 12.7mm$, $d_2 = 25.4mm$, $d_3 = 38.1mm$, and $d_4 = 50.8mm$, that correspond to radii of r_1 =0.5D, r_2 =1D, r_3 =1.5D, and r_4 =2D. The cross section of the rings was square with a dimension t=1.27mm(0.1D). The rings were held in place using a thin piece of sheet metal designed so that tests could be performed using any or all of the rings. The foil deflected slightly when the jet impinged on the plate so it was difficult to perform test with the rings directly on the plate. Thus, small clearance of C/t=0.5, 1.14 and 1.62, or C/D=0.05, 0.114, and 0.162 were investigated here.

Hansen and Webb[45] previously argued that the heat transfer could be enhanced by adding fins on the surface to act as extended surfaces similar to the trips investigated here. It should be noted that the trips examined here were constructed from plexiglas and they would not act as a fin. Thus, the devices are designed to

act as turbulence promoters near the wall similar to the devices used by Kum and Kawaguchi[44] for plane jets.

The heat transfer enhancement was measured for trips at a number of different locations shown in Table 4.7. The local Nusselt number and average Nusselt number measured for these test cases for impinging jets with H/D=2, 4 and 6 are shown in Figure 4.52-4.54. It is clear that the heat transfer is significantly enhanced over some regions of the impingement surface by the trips. The initial test that included all of the trips suggested that only the first one or two trips was causing a heat transfer enhancement and the later trips were not having a significant effect. In fact, the average Nusselt number was reduced for regions where r/D>2.

	Trip 1	Trip 2	Trip 3	Trip 4
Test 1	√	√	√	√
Test 2	√		√	
Test 3		√		√
Test 4	√			

Table 4.7: Trip combinations used in test, trip 1 at r/D=0.5, trip 2 at r/D=1, trip 3 at r/D=1.5, trip 4 at r/D=2

It was conjectured that the trips may have been positioned too close together and were promoting a growth in the wall jet without a corresponding growth in the turbulence intensity near the wall. Thus, tests were performed using only two trips, one set with the trips in the first and third position and the second set with trips in the second and fourth location. It was observed that the heat transfer characteristics of the first case showed a peak in the heat transfer that was similar to the results from the initial test. The measurements with the trips at the second and fourth location showed a peak in the heat transfer after the second ring. Thus, these results seem to indicate that most of the heat transfer enhancement was caused by the first trip used in the experiment.
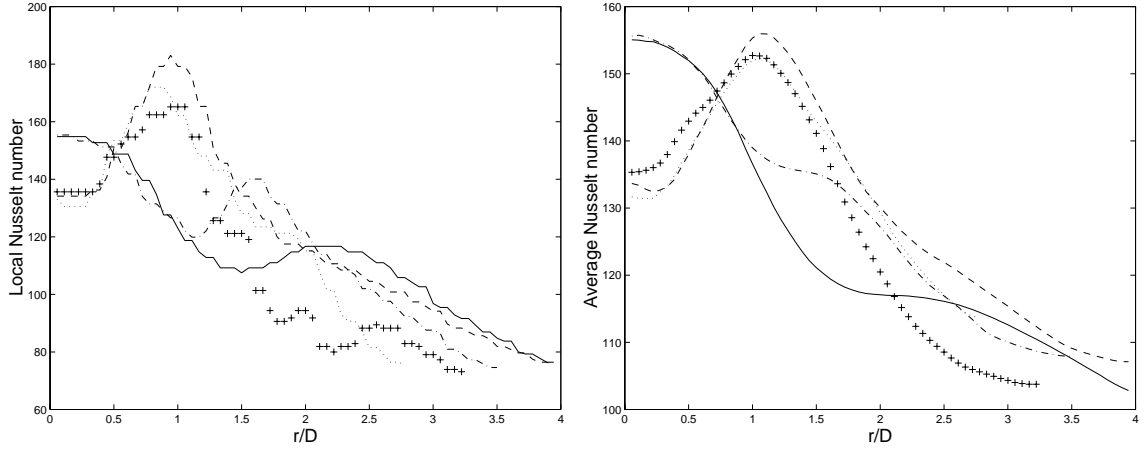
Figure 4.52: Distributions of local and average Nusselt number for Re=23,000, C/t=0.5 at H/D=2, − no trip, - - trip 1, ··· trip 1 & 3, -·- trip 2 & 4, and + trip 1, 2, 3 & 4.

Figure 4.53: Distributions of local and average Nusselt number for Re=23,000, C/t=0.5 at H/D=4, symbols same as above

Figure 4.54: Distributions of local and average Nusselt number for Re=23,000, C/t=0.5 at H/D=6, symbols same as above

This was confirmed by performing heat transfer measurements with only a single trip at r/D=0.5. It is clear that in this case the peak in the heat transfer associated with the separated flow after the first trip is larger than any of the other experiments for all three jet-to-plate spacings. It is also interesting to note that the heat transfer at the centerline is suppressed for this case and all three cases that used a trip at the first location. It is conjectured that it is caused in part because there is an adverse pressure gradient upstream of the trip that reduces the velocity of the flow near the wall in the impingement region. The trip may also act to stabilized the potential core, suppressing any oscillation that would promote heat transfer. This reduction of heat transfer is not observed when the ring is located at the second position.

It should be noted that for small and intermediate impingement distances. H/D=2 and 4, the heat transfer seems to be relatively independent of jet-to-plate spacing. Thus, the results suggest that the heat transfer enhancement is mainly a function of how the trips affect the wall jet. This is not that unexpected since the results from the investigation of the flow in the wall jet suggests that the mechanism causing the heat transfer in the wall jet portion of the impinging jet is the same for the two cases.

The effects of the distance between the trip and the plate on heat transfer were studied for the case where trips were located in the second and the fourth locations. This combination gives the highest overall heat transfer rate in the region r/D≤3 for jet-to-plate spacing H/D=6. The local and average Nusselt number for trip-to-plate spacings of C/D=0.50, 1.14, and 1.62 and jet-to-plate spacing of H/D=2, 4 and 6 are shown in Figures 4.55 - 4.57. The smaller trip-to-plate distances generally yield higher local Nusselt number in the region $1 < r/D < 2$ and lower local Nusselt number in the far field region $r > 2$, indicating smaller clearance between the trip and the plate yields larger effect on the development of the wall jet, hence changes the pattern of heat transfer. The trip array produces heat transfer enhancement within the region $1 < r/D < 3$ in all these cases. The average Nusselt number is below the baseline
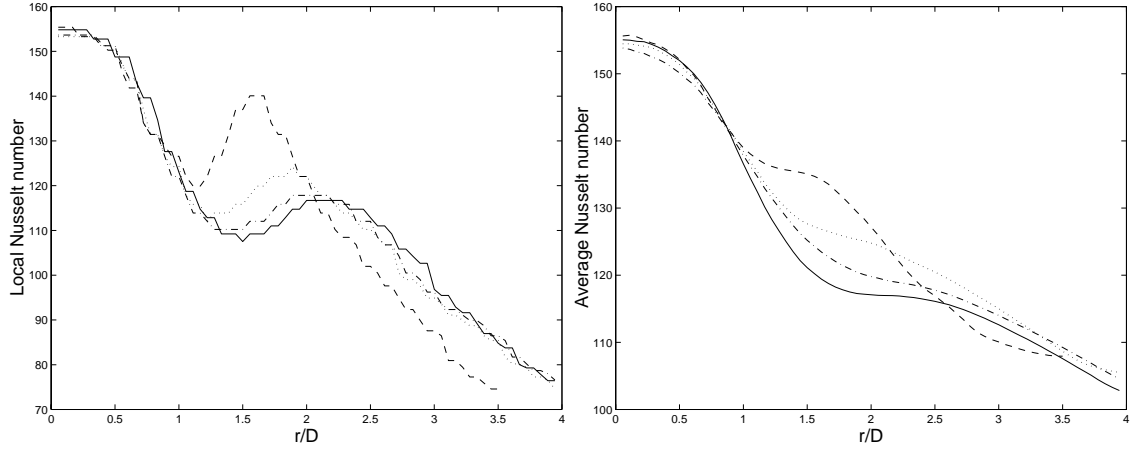
Figure 4.55: Distributions of local and average Nusselt number for Re=23,000 at H/D=2, − no trip, trip 2 & 4 with trip-to-plate distance - - C/t=0.50, ··· 1.14 and -·- 1.62.
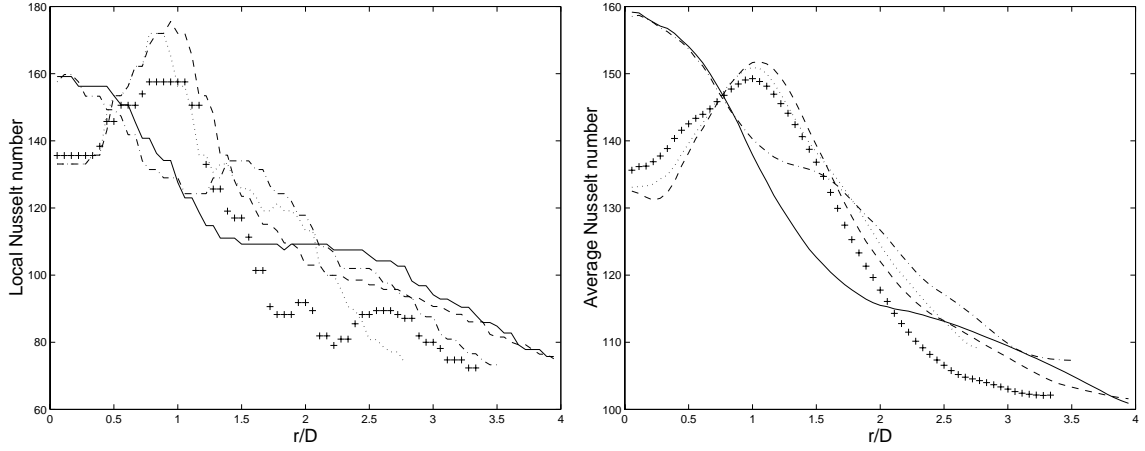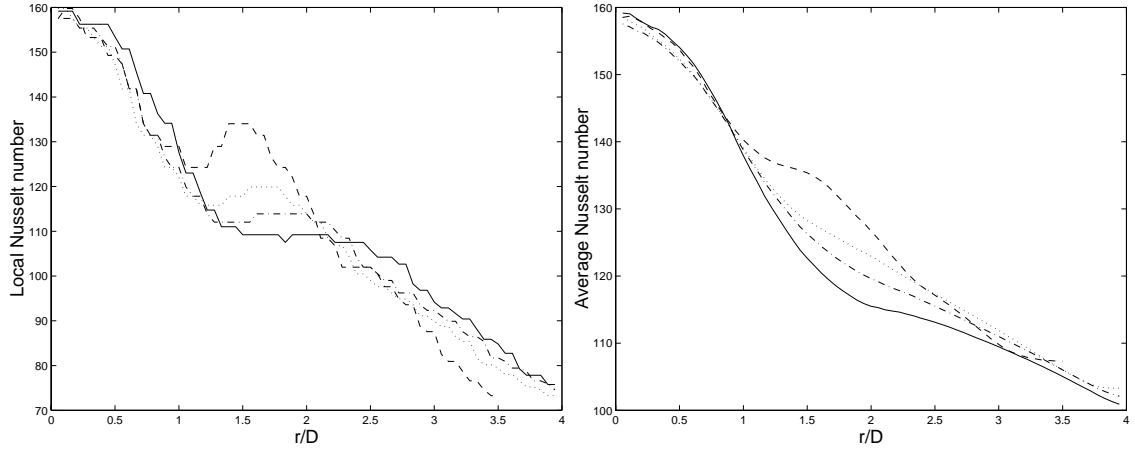

Figure 4.56: Distributions of local and average Nusselt number for Re=23,000 at H/D=4, symbols same as above.

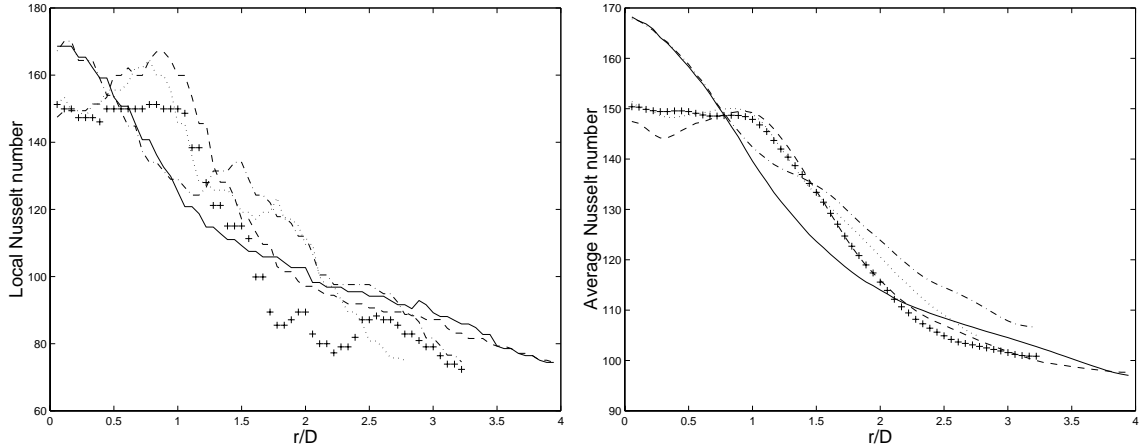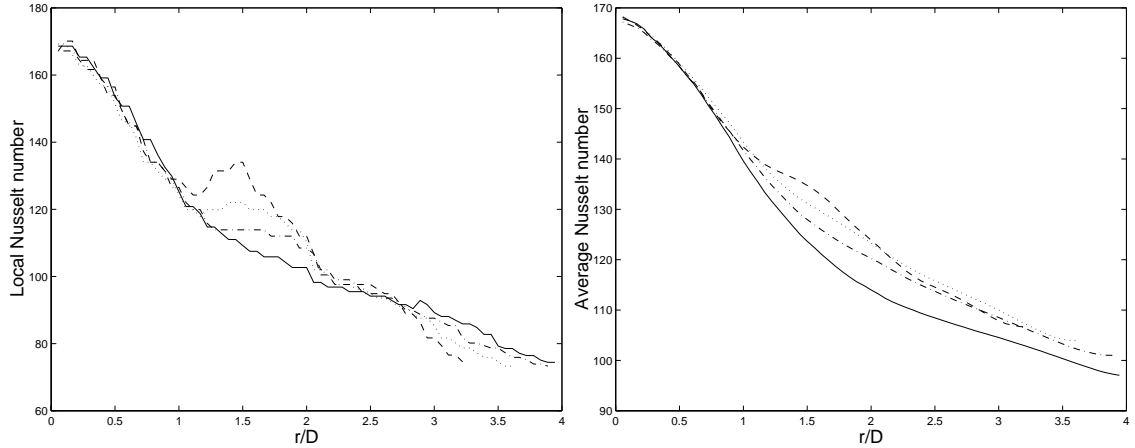Figure 4.57: Distributions of local and average Nusselt number for Re=23,000 at H/D=6, symbols same as above.

case for r/D>3 when the jet-to-plate spacing are H/D=2 and 4. For H/D=6 there is still heat transfer enhancement for r/D>3. Flow field measurements were performed in order to clarify the mechanism that causes the heat transfer enhancement.

Flow Measurement

The measurement of the heat transfer enhancement caused by the different trip combinations suggested that the trips were affecting the development of the wall jet. By comparing the Nusselt number distributions for these trip combinations, it is found that a trip at the first location has the largest effect on the flow. Thus, flow visualization experiments were performed in the plain impinging jet and the impinging jet with a trip ring at r/D=0.5 for a trip-to-plate distance of C/D=0.25. The images for a Reynolds number of 5,640 are shown in Figure 4.58. Again, although the Reynolds number is considerably lower than the Reynolds number used in the heat transfer studies, the images should give a qualitative understanding of the effect of the trips. The images do not very clearly show the difference between the two cases. The results indicate that the thickness of wall jet boundary layer for the with trip case is larger that for the plain case, indicating the trip is enhancing mixing in the wall jet.

The mean and dynamic pressure on the impingement plate were measured using pressure transducers and microphones in order to confirm the results of the flow visualization. Measurements were taken in the plain impinging jet and the impinging jet with a trip ring at r/D=0.5 for a Reynolds number of 23,00. The mean pressure distributions for these two cases are shown in Figure 4.59. It is found that the mean pressure on the impingement plate was increased in the entire region studied, indicating that the flow structure has been changed.

A comparison of the variance of the dynamic wall pressure measured in the flow with and without the trip are shown in Figure 4.60. The variance of the dynamic pressure was decreased in the region r/D≤0.5 by 15-25% when the trip was added to
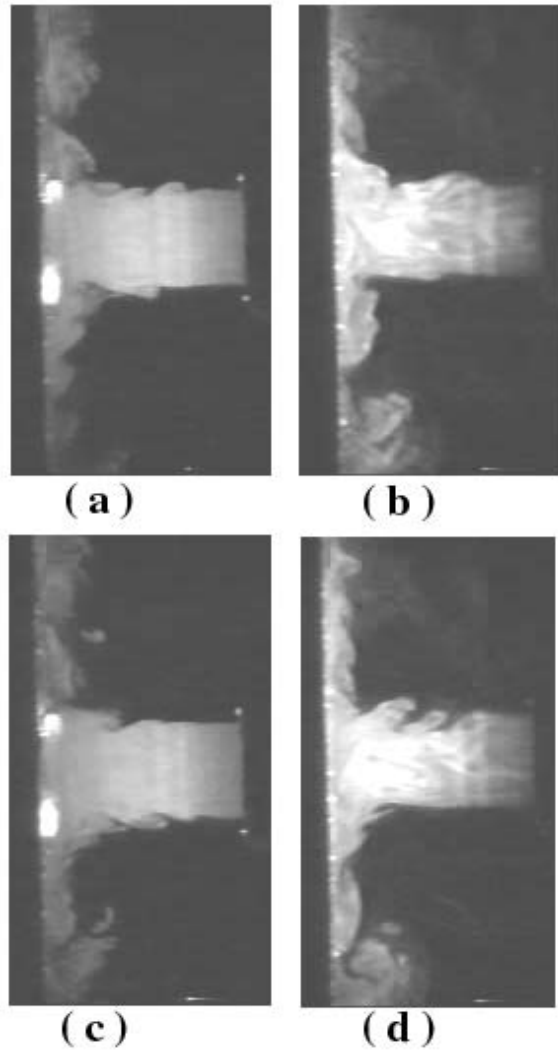
Figure 4.58: Flow visualization of impinging jet with and without trip on the plate for H/D=2 and Re=5,640, trip inner radius r/D=0.5, trip thickness t/D=0.1, trip-to-plate distance C/t=0.25. (a),(c) with trip, (b),(d) no trip
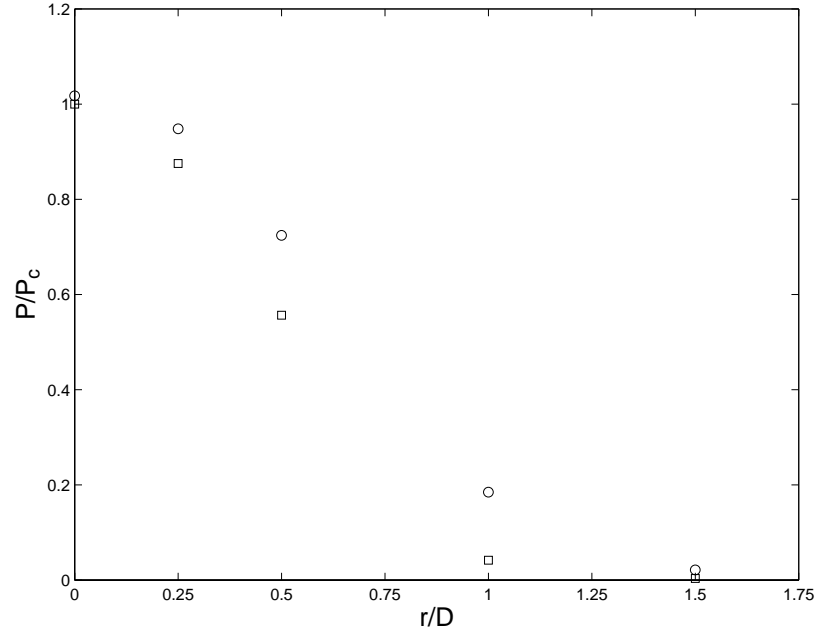
Figure 4.59: The mean pressure distribution on the impingement plate for the for H/D=2 and Re=23,000, normalized by the centerline pressure, □ no trip; ◯ with trip.

the wall, indicating that the trip was suppressing the turbulence fluctuations in this area and likely the heat transfer. The variance of the dynamic pressure increased by 50% at r/D=1.5. It is also clear from the pressure spectra shown in Figure 4.61, that the structure of the flow has changed significantly with the addition of the trip. The trip adds a significant amount of small-scale motions due to the flow separation at r/D=0.5∼1.0, but these are not seem at r/D=1.5. It is clear, though, these motions either reduce the strength of the ring vortices or move them away from the wall. The variance of the pressure does not rise between r/D=1 and 1.5 and the peak in the spectra associated with the vortex ring and vortex stretching does not seem to occur. Thus, the pressure measurements seem to explain both the peak in the heat transfer observed at r/D=1 and the seeming lack of secondary heat transfer peak in the region r/D=1-1.5.
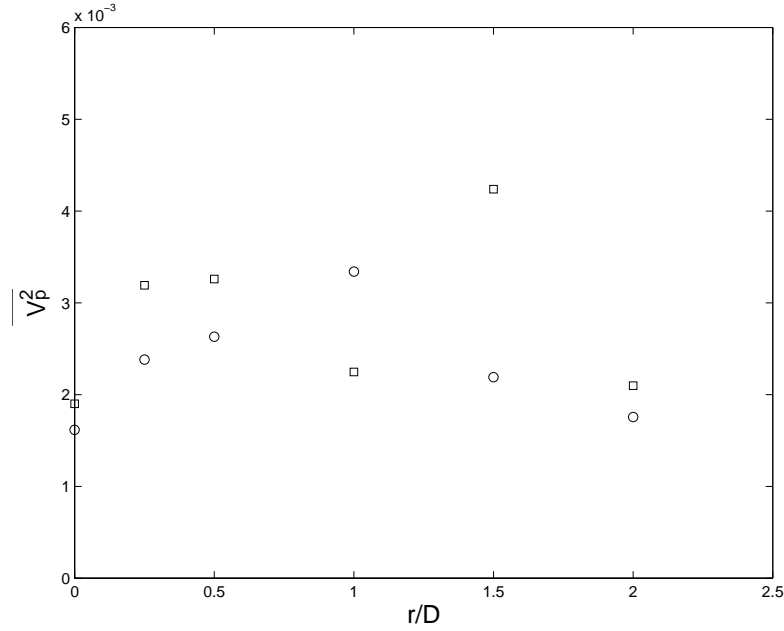
Figure 4.60: Distribution of the dynamic pressure variance on the impingement surface with a trip ring at r/D=0.5 for jet-to-plate spacing H/D=2 and Re=23,000, □ no trip; ◯ with trip.

The azimuthal correlations of the pressure around the impingement plate at r/D=1, 1.5 and 2 for H/D=2 were also measured in order to obtain a clearer understanding of the flow mechanism that causes the heat transfer enhancement. A comparison of the azimuthal correlations measured with the trip in place and the azimuthal spectra corresponding to these measurement are shown in Figure 4.62. The results for the plain impingement surface without the trip are shown again in Figure 4.63.

The most significant difference between the results is the significant reduction in the correlation length at r/D=1.0. This indicates the flow in this region is the result of the three-dimensional separated shear layer generated by the trip. The flow returns to a more two-dimensional flow at r/D=1.5 after the effect of the separated flow decays.
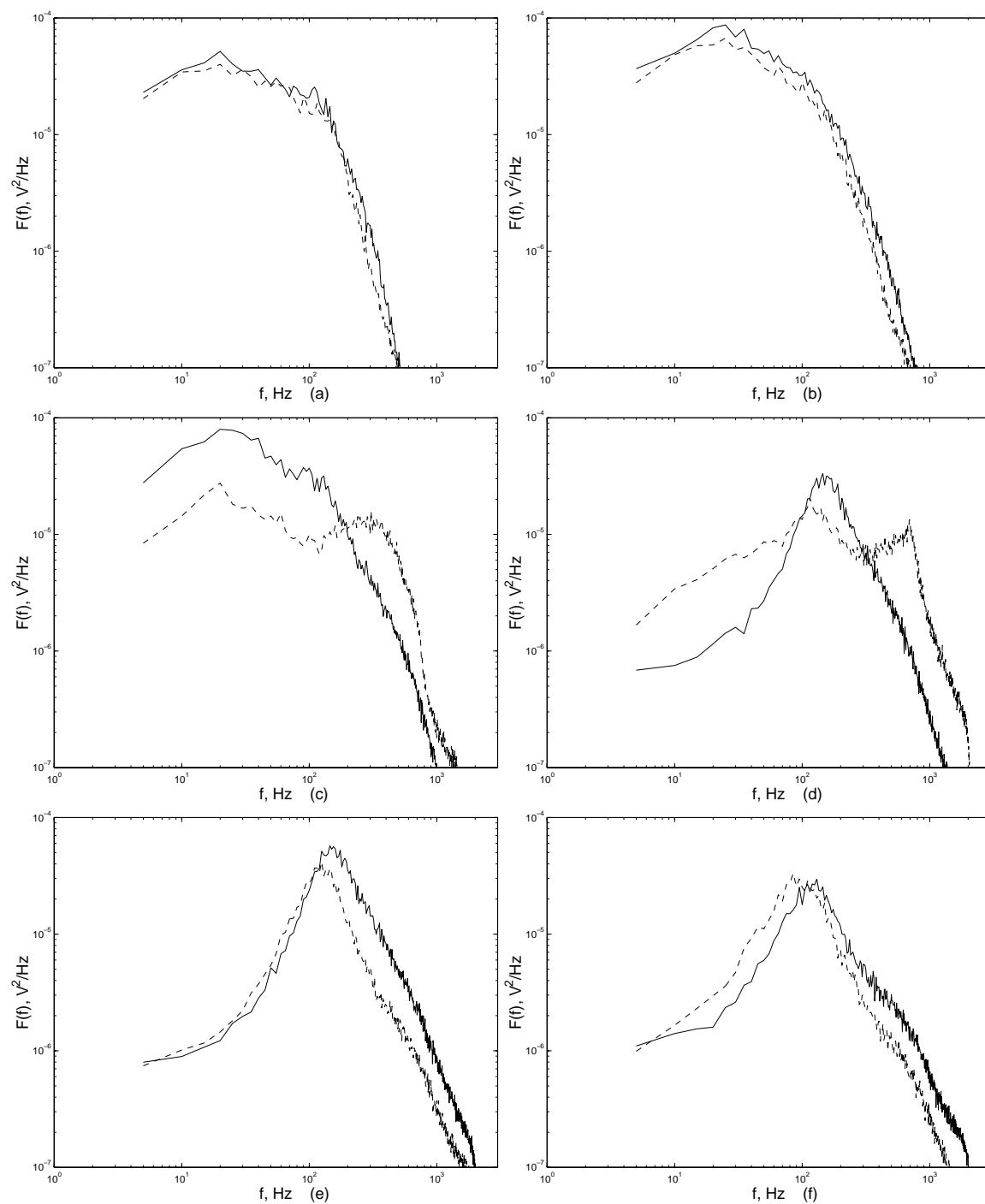
Figure 4.61: Spectra of dynamic wall pressure − without trip and - - with trip for Re=23,000 at H/D=2 and (a) r/D=0, (b) r/D=0.25, (c) r/D=0.5, (d) r/D=1, (e) r/D=1.5, (f)r/D=2.
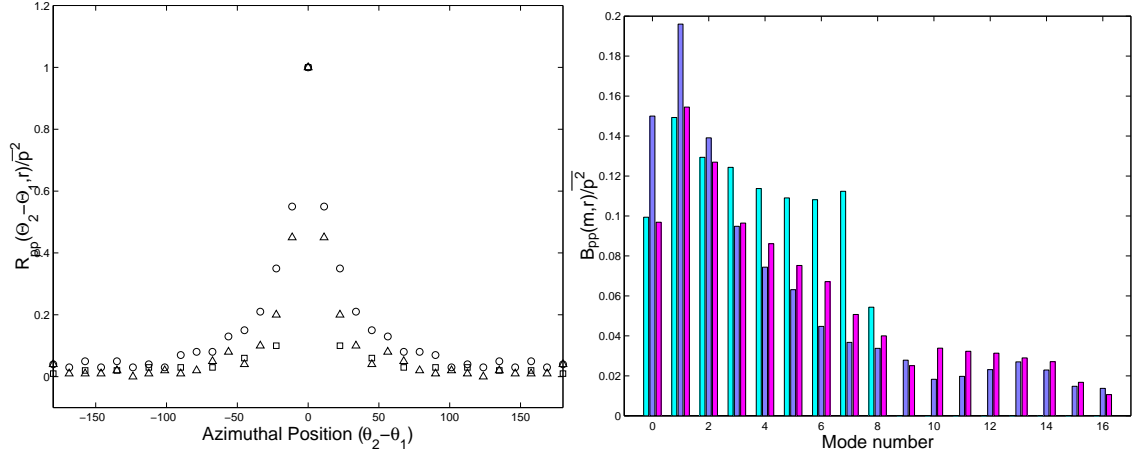
Figure 4.62: Azimuthal correlation of dynamic wall pressure and modal energy distribution for jet-to-plate spacing H/D=2 **with** a trip at r/D=0.5, (a) □ r/D=1, ◯ r/D=1.5, △ r/D=2. (b) from left to right r/D=1, 1.5 and 2.
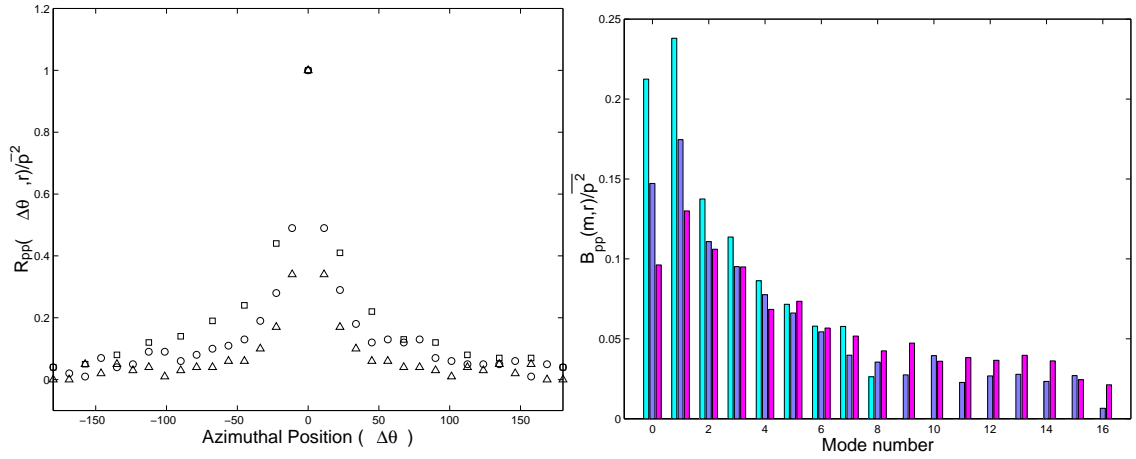
Figure 4.63: Azimuthal correlation of dynamic wall pressure and modal energy distribution for jet-to-plate spacing H/D=2, (a) □ r/D=1, ◯ r/D=1.5, △ r/D=2. (b) from left to right r/D=1, 1.5 and 2.

The flow after the separated region appears to become more two-dimensional as the structures in the wall jet re-attach. The vortex stretching and separation seen in the jet on the plane surface is not observed in the flow with the trip and hence the secondary peak in the heat transfer is suppressed. It appears the trip is playing a similar role to the vortex separation in the natural jet. The trip simply controls the location of the event. In addition, unlike the plane jet, later downstream trips do not seem to have as beneficial effect as the first. Unfortunately time did not permit an investigation of the flow field in these cases.

Chapter 5

Conclusion

Impinging round jets are used in a wide variety of cooling and drying applications, and commonly used to test turbulent heat transfer models. Measurements were performed in this investigation of the heat transfer produced by an impinging jet exiting a fully developed pipe with a Reynolds number of 23,000. The fully developed pipe was chosen for this investigation both to facilitate comparison with previous results and because this flow has well defined boundary conditions that facilitate the testing of turbulent models. Measurements were initially performed to extend the existing database by examining the change in the Nusselt number distribution with jet-to-plate spacing in more detail than previous measurements and to examine the effect that confinement has on the heat transfer. Measurements were also performed to determine the heat transfer enhancement produced by adding tabs on the pipe outlet that enhance the mixing in the jet, and by adding trips to the impingement surface to enhance the turbulence levels in the wall jet. The flow field in the impinging jets was also investigated using flow visualization, measurements of the velocity field in the jet, and the dynamic pressure of the wall jet.

Initially, it was shown that the Nusselt number distributions in the impinging jet measured here were in good agreement with the measurements reported previously

by Baughn and Shimizu[26] for jet-to-plate spacing of 2, 6 and 10 diameters. The change in the Nusselt number distribution with jet-to-plate spacing were investigated in more detail here by measuring the distribution for every diameter increase in the range 2≤H/D≤10. In all cases, the maximum Nusselt number occurred at the stagnation point, as expected. The stagnation heat transfer is approximately constant for $2 \leq H/D \leq 4$ because the centerline velocity and the turbulence intensity in the jet is approximately constant. The stagnation heat transfer increases significantly from H/D=4-6 due to the increase in the turbulence intensity near the center of the jet. This peak was broad, extending from approximately $6 \leq H/D \leq 8$, despite the fact the mean velocity in the jet was decreasing. This decrease in the mean flow was offset by the increase in the turbulence intensity on the centerline. It was found that the strong secondary peak observed previously for H/D=2 at r/D≈2 also occurred at H/D=3, but there was a larger change in the size of the peak between H/D=3 and 4. There was not a secondary peak for H/D≥5 but an inflection in the Nusselt number distribution was observed at the same location for H/D=5-7. In fact, the most significant difference in the Nusselt number distribution for H/D=6-8 was the decrease in this inflection in the Nusselt number distribution.

Landreth and Adrian and others had shown previously that the secondary peak in the heat transfer for H/D=2 was caused by the separation of the large-scale vortex ring structures from the plate. Measurements of the dynamic wall pressure were performed for H/D=2 and 4 to examine whether the same flow mechanism was causing the heat transfer in these two cases and potentially for jet-to-plate spacing up to 7 diameters. The measurement of the rms wall pressure and pressure spectra for H/D=2 showed strong evidence of the passage of the vortex rings for r/D≤1.5 and a distinct change at r/D≈2 associated with the separation and breakdown of the structures. Thus, these measurements confirmed that the evolution and separation of the vortex rings could be detected using measurements of the dynamic wall pressure. The measurements of

the pressure spectra for H/D=4 showed similar features though the strength of the rings and the effect of their separation was significantly smaller or the events were less frequent. This is not unexpected since the vortex rings that initially develop in the axisymmetric shear layer break down as the flow evolves downstream. The results suggest, though, that the flow mechanism causing the secondary heat transfer peak in the two cases was the same.

The changes of the Nusselt number distribution with Reynolds number were also investigated for H/D=2. The secondary peak became more pronounced as Reynolds number increased but its location did not appear to change as Lytle and Webb[37] found for H/D=0.5-1.0. The data was scaled using the correlation $Nu \propto Re^{0.7}$ proposed by Goldstein and Franchett[25]. It was found this correlation collapsed the data for Reynolds number greater than 15,400.

The effect of confinement on the heat transfer produced by impinging jets was also investigated by measuring the Nusselt number distributions for jets exiting long pipe with and without a confining wall. It was found that confinement affects the impinging jets within H/D≤3 with the largest effect for small jet-to-plate spacings, as expected. The local Nusselt number was increased for r/D≤2 for jet-to-plate spacings less than 2 diameters. The Nusselt number for H/D=0.25, the smallest spacing considered here, was increased by as much as 40%. The average Nusselt number in this region was increased by approximately 27% for H/D=0.25 and 7% for H/D=2. The heat transfer was decreased for r/D≥2 for all separation distances less than 3 diameters with the largest effect corresponding to the smallest separation distance. The average Nusselt number was increased for r/D≈3 except for at H/D=0.25.

The measurements of the variance of the dynamic wall pressure was larger near the impingement region for the confined jet, explaining the larger heat transfer in this region. The turbulence level on the plate surface for the confined case drops under the unconfined case at r/D=1.5, where the flow separation occurs in the unconfined

wall jet, indicating that the flow separation either disappears or shifts outward in the confined case. The heat transfer reduction for larger separation distance is likely caused by the reduction of entrainment into the wall jet.

Measurements were performed to examine the heat transfer enhancement generated when tabs are added to the end of the pipe. It is found that the tabs enhance the mixing and reduce the length of the potential core of the impinging jet. The heat transfer for short jet-to-plate spacing cases were significantly enhanced while the enhancement for H/D=6 was not as significant because the flow was already highly turbulent. The peak of the stagnation heat transfer, associated with the end of the jet potential core, shifted to smaller H/D when the tabs were added.

For the six tab array at small jet-to-plate spacing H/D=2, there were six regions of heat transfer enhancement surrounding the impingement region, and six alternative regions of heat transfer enhancement and reduction away from the centerline. It was shown using flow visualization and velocity measurements that the inner heat transfer regions correspond to the high-speed jets exiting between adjacent tabs due to the blockage of the tabs. The alternating regions of the heat transfer enhancement and reduction for large radial distances are caused by the effect of counter rotating vortices, produced by the tabs, traveling along the plate.

The tabs affect the flow differently for arrays of ten and sixteen tabs, where the gap between two adjacent tabs are small. Here, the flow tends to issue from the relatively large gaps so the number of the heat transfer enhancement regions is only half of the number of the tabs for small impingement regions. There were five and eight alternating enhancement and reduction regions in the far wall jet for the ten and sixteen tab arrays caused by the motions of the counter rotating vortices. Larger number of tabs generally give higher overall heat transfer rates within the circular region r/D≤3.

It was also found that the heat transfer enhancement was larger for the longer tabs

for all the jet-to-plate spacings. The larger tabs produce larger blockage effects and larger streamwise vortices that produce the most mixing. The effect of increasing the tab height is the most pronounced for the small jet-to-plate spacing case because of the enhanced blockage. The effect of the tab arrays are less pronounced for the large jet-to-plate case though they tend to significantly shorten the development length of the jet.

The strength of the vortex shed by the tabs can also be changed by angling the tabs relative to the flow. The 45° angled tabs produce a 3-4% increase in the heat transfer for the near impingement cases. For the larger impingement distance the angled tabs produce a small difference in the heat transfer, but not as large as that caused by the change in height of the tabs.

The heat transfer enhancement caused by trips on the impingement surface was also investigated. It was found that a trip ring on the impingement surface created a separated flow that is approximately 8-10 trip heights long. The mean pressure and pressure fluctuation were significantly higher than those of the no trip case at the end of the recirculation zone. The heat transfer was enhanced 30%-44% at this location. Ring shape vortices shed from the trip were formed one diameter downstream from it and broke down rapidly in another half diameter.

It is found that the heat transfer at the stagnation point was suppressed when there was a trip at r/D=0.5 likely because the trip reduced the speed of the flow next to the wall in the impingement region. It was also found that only the first trip in a trip array, no matter where it is, will cause the heat transfer enhancement while later trips did not have significant effect.

The mechanism causing the heat transfer in the wall jet portion of the impinging jet is the same for the the jet-to-plate spacing H/D=2-4. Thus, the results suggest that the heat transfer enhancement is mainly a function of how the trips affect the wall jet. The smaller trip-to-plate distances generate stronger vortices, which effectively

increase the turbulent intensity on the plate surface. However, these ring shape vortices break down very fast. This causes higher local Nusselt number in the near stagnation region $1 < r/D < 2$ and lower local Nusselt number in the far field region $r/D > 2$.

Bibliography

[1] M. Morris and C. Medwell (1996), Design of air jets for strip cooling, *Ironmaking and Steelmaking*, **23**, 436-440

[2] N. Rajaratnam (1976), Turbulent jets, Elsevie, New York

[3] G.N. Abramovich (1963), The theory of turbulent jets, MIT Press, Cambridge, MA.

[4] J. Walker, C. Smith, A. Cerra and T. Doligalski (1987), The impact of a vortex ring on a wall, *J. Fluid Mech.*, **181**, 99-140

[5] C.O. Popiel and O. Trass (1991), Visualization of a free and impinging round jet, *Exp. Thermal and Fluid Sci.*, **4**, 253-264

[6] N. Didden and C. Ho (1985), Unsteady seperation in a boundary layer produced by an impinging jet, *J. Fluid Mech.* **160**, 235-256

[7] C.C. Landreth and R.J. Adrian (1990), Impingement of a low Reynolds number turbulent circular jet onto a flat plate at normal incidence, *Experiments in Fluids*, **9**, 74-84

[8] E. Nelson, Phase-averaged measurements of vortex interaction with a solid surface and the breakaway process. M.S. thesis: Illinois Institute of Technology

[9] J. Harvey and F. Perry (1971), Flow field prooduced by trainling vortices in the vicinity of the ground, *AIAA J.*, **9**, 1659-1660

[10] K. Martin (1997), Heat and mass transfer between impinging gas jets and solid surfaces, *Advances in Heat Transfer*, Academic Press, **13**

[11] K. Jambunatham, E. Lai, M. A. Moss and B. L. Button (1992), A review of heat transfer data for singe circular jet impingement, *Int. J. Heat and Fluid Flow*, **13**

[12] R. Viskanta (1993), Heat transfer to impinging isothermal gas and flame jets, *Exp. Thermal and Fluid Sci.*, **6**, 111-134

[13] C. Donaldson, R.S. Snedeker and D.P. Margolis (1971), A study of free jet impingement. Part 2. Free jet turbulent structure and impingement heat transfer, *J. Fluid Mech.*, **45**, 477-512

[14] A. K. Mohanty and A. A. Tawfek (1993), Heat transfer due to a round jet impinging normal to a flat surface. *Int. J. Heat Mass Transfer*, **36**, 1639-1647

[15] J. Stevens and B. W. Webb, Local heat transfer coefficients under an axisymmetric, singe phase liquid jet. *ASME J. Heat Transfer*, **113**, 71-78

[16] Y. Haneda, Y. Tsuchiya, K. Nakabe and K. Suzuki (1998), Enhancement of impinging jet heat transfer by making use of mechano-fluid interactive flow oscillation, *Int. J. Heat Fluid Flow*, **19**, 115-124

[17] R.J. Goldstein and A. I. Behbahani (1982), Impingment of a circular jet with and without cross flow, *Int. J. Heat Mass Transfer*, **25**, 1377-1382

[18] R. J. Goldstein, A. I. Behbahani and K. K. Heppelmann (1986), Streamwise distribution of the recovery factor and the local heat transfer coefficient to an impinging circular air jet, *Int. J. Heat Mass Transfer*, **29**, 1227-1235

[19] R. J. Goldstein, K.A. Sobolik and W.S. Seol (1990), Effect of Entrainment on the heat transfer to a heated circular jet impinging on a flat surface. *ASME J. Heat Transfer*, **112**, 608-611

[20] L. Huang and M. El-genk (1994), Heat transfer of an impinging jet on a flat surface, *Int. J. Heat Mass Transfer*, **37**, 1915-1923

[21] L. Huang and M. El-genk (1998), Heat transfer and flow visualization experiments of swirling, multi-channel, and conventional impinging jets, *Int. J. Heat Mass Transfer*, **41**, 583-600

[22] D.A. Zumbrunnen and M. Aziz (1993), Convective heat transfer enhancement due to intermittency in an impinging jet, *ASME J. Heat Transfer*, **115**, 91-98

[23] J. Baughn (1995), Liquid crystal methods for studying turbulent heat transfer, *Int. J. Heat and Fluid Flow*, **16**, 365-375

[24] C.J. Hoogendoorn (1977), The effect of turbulence on heat transfer at a stagnation point, *Int. J. Heat Mass Transfer*, **20**, 1333-1338

[25] R.J. Goldstein and M. E. Franchett (1988), Heat Transfer From a Flat Surface to an Oblique Impinging Jet, *ASME J. Heat Transfer*, **110**, 84-90.

[26] J. W. Baughn and S. Shimizu (1989), Heat Transfer Measurements From a Surface With Uniform Heat Flux and an Impinging Jet, *ASME J. of Heat Transfer*, **111**, 1096-1098

[27] J.W. Baughn, A.E. Hechanova and Xiaojun Yan (1991), An Experimental Study of Entrainment Effects on the Heat Transfer ¿From a Flat Surface to a Heated Circular Impinging Jet. *ASME J. of Heat Transfer*, **113**, 1023-1025

[28] J.W. Baughn and X. Yan (1991), A preheated-wall transient method for measurements of the heat transfer to an impinging jet. *Eurotherm Seminar*, **25**, 1-7

[29] X. Yan, J.W. Baughn and M. Mesbah (1992), The effect of Reynolds number on the heat transfer distribution from a flat plate to an impinging jet, *Fundametal and Applied Heat Transfer Research for Gas Turbine Engine, ASME HTD*, **226**

[30] S.J. Lee, J.H. Lee, D.H. Lee (1994), Local heat transfer measurements from an elliptic jet impinging on a flat plate using liquid crystal, *Int. J. of Heat Mass Transfer*, **37**, 967-976.

[31] D. Lee, R. Greif, S.J. Lee and J. H. Lee (1995), Heat Transfer from a flat plate to a fully developed Axisymmetric Impinging jet, *ASME J. Heat Transfer*, **117**, 772-776

[32] D. W. Colucci and R. Viskanta (1996), Effect of nozzle geometry on local convective heat transfer to a confined impinging air jet, *Exp. Thermal and Fluid Sci.*, **13**, 71-80

[33] Huber and Viskanta (1994), Convection heat transfer to a confined impinging array of air jets with spent air exits, *ASME J. Heat Transfer*, **116**, 570-576.

[34] G. Carlomagno and L. de Luca (1989), Infrared thermography in heat transfer, *Handbook of Flow Visualization*, Hemisphere, 531-553

[35] Y. Pan, J. Stevens and B.W. Webb (1992), Effect of nozzle configuration on transport in the stagnation zone of axisymmetric, Impinging free surface liquid jets: part 2-local heat transfer, *ASME J. Heat Transfer*, **114**, 880-886

[36] K. Garrett and B.W. Webb (1999), The effect of drainage configuration on heat transfer under an impinging liquid jet array, *ASME J. Heat Transfer*, **121**, 803-810

[37] D. Lytle and B.W. Webb (1994), Air jet impingement heat transfer at low nozzle-plate spacings, *Int. J. Heat Mass Transfer*, **37**, 1687-1697

[38] L.F.A. Azevedo, B. W. Webb and M. Queiroz (1994), Pulsed Air Jet Impingement Heat Transfer, *Exp. Thermal and Fluid Sci.*, **8**, 206-213

[39] C. Meola, L. de Luca and G. M. Carlomagno (1995), Azimuthal instability in an impinging jet: adiabatic wll temperature distribution, *Exp. in fluids*, **18**, 303-310

[40] C. Meola, L. de Luca and G. M. Carlomagno (1996), Influence of Shear Layer Dynamics on Impingement Heat Transfer, *Exp. Thermal and Fluid Sci*, **13**, 29-37

[41] J. Seyed-Yagoobi, V. Narayanan and R.H. Page (1998), Comparison of heat transfer characteristics of radial jet reattachment nozzle to in-line impinging jet nozzle, *ASME J. Heat Transfer*, **120**, 335-341

[42] C.M. Ho and J. Gutmark (1987), Vortex induction and mass entrainment in a small aspect ratio elliptic jet, *J. Fluid Mech.*, **179**, 383-405

[43] Robert Gardon and J.C. Akfirat (1996), The role of turbulence in Determining the Heat transfer characteristics of Impinging Jet, *Int. J. Heat Mass Transfer*, **8**, 1261-1272

[44] S.M. Kum and Y. Kawaguchi (1995), A study on heat transfer enhancement by a square rod array in an impinging jet system, *Heat Transfer-Japanese Research*, **24**

[45] L.G. Hansen and B. W. Webb (1993), Air jet impingement heat transfer from modified surface, *Int. J. Heat Mass Transfer*, **36**, 989-997

[46] T. Liu and J.P. Sullivan (1996), Heat transfer and flow structures in an exited circular impinging jet, *Int. J. Heat Mass Transfer*, **39**, 3695-3706

[47] C. Gau, W.Y. Sheu and C.H. Shen, Impingement cooling flow and heat transfer under acoustic excitations, *ASME J. Heat Transfer*, **119**

[48] M. Behnia, S. Parneix, Y. Shabany and P.A. Durbin (1999), Numerical study of turbulent heat transfer in confined and unconfined impinging jets, *International Heat and Fluid Flow*, **20**, 1-9

[49] K. Kataoka, M. Suguro, H. Degawa, K. Maruo and I. Mihata (1987), The effect of surface renewal due to large scale eddies on jet impingement heat transfer, *Int. J. Heat Mass Transfer*, **30**, 559-567

[50] K. Kataoka, S. Hamano, A. Onishi, H. Kawasaki and G.Y. Li (1992), Control of jet impingement heat transfer by a wake flow behind an array of circular cylinders, *J. of Chemical engineering of Japan*, **25**

[51] C.D. Donaldson, R.S. Snedeker and D.P. Margolis (1971), A study of free jet impingement, Part II. Free jet turbulent structure and impingement hat transfer, *J. Fluid Mech.*, **45**, 477-512

[52] M. Smith and A. Kuethe (1966), Effects of turbulence on laminar skin friction and heat transfer, *Physics Fluids*, **9**, 2337-2344

[53] J. Kestin and R. Wood (1971), The influence of turbulence on mass transfer from cylinders, *J. Heat Transfer*, **93**, 321-327

[54] G.W. Lowery and R.I. Vachon (1975), The effect of turbulence on heat transfer from heated cylinders, *Int. J. Heat Mass Transfer*, **18**, 1229-1242

[55] R. Fox and A. McDonald (1992), Introduction to fluid mechanics 4th edition. John Wiley and Sons

[56] N. Rajaratnam (1976), Turbulent Jets, Elsevier, New York

[57] S.J. Kline and F. A. McClintock (1953), Describing uncertainties in single-sample experiments, mechanical engineering, **75**, 3-8

[58] F.P. Incropera and D.P. DeWitt (1981), Fundamentals of heat transfer, John Wiley and Sons

[59] C. Lomas (1986), Fundametals of hot wire anemometry, Cambridge University Press

[60] Dantec Corp, DISA type 55M01 main unit setup manual,

[61] AGEMA Infrared Systems (1987), AGEMA thermovision 880 operating manual

[62] C.M. Ho and E. Gutmark (1987), Vortex induction and mass entrainment in small-aspect-ratio elliptic jet, *J. of Fluid Mech.*, **179**, 383-405.

[63] L Bradbury and A. Khadem (1975), The distortion of a jet by tabs, *J. Fluid Mech.* **70**, 801-813

[64] M. Samimy, K. Zaman and M. Reeder (1993), Effect of tabs on the flow and noise field of an axisymmetric jet, *AIAA Journal*, **31**, 609-619

[65] K. Zaman, M. Reeder and M. Samimy (1994), Control of an axisymmetric jet using vortex generators, *Phys. Fluids*, **6**, 778-793

[66] M.F. Reeder and M. Samimy (1996), The evolution of a jet with vortex-generating tabs: real-time visualization and quantitative measurements, *J. Fluid Mechanics*, **311**, 73-118

[67] J. Mi, G. Nathan (1999), Effect of small vortex-generators on scalar mixing in the developing region of a turbulent jet, *Int. J. of Heat and Mass Transfer*, **42**, 3919-3929

[68] Z.D. Husain and A.K.M.F. Hussain (1979), Axisymmeric mixing layer: influence of the initial and boundary conditions, *AIAA Journal*, **17**, 48-55

[69] T.C. Corke and S. M. Kusek (1993), Resonance in axisymmetric jets with controlled helical-mode input, *J. of Fluid Mechanics*, **249**, 307-336

[70] M. Glauser (1987), Coherent structures in axisymetric turbulent jet imxing layer, PhD thesis, State University of New York at Buffalo

[71] A. Pollard, S. McIlwain, R. Avva, R. Barron, A. Boglaev, A. Latypov and M. Malin (1995), Validation exercise CFD95 Impinging turbulent round jet with heat transfer, *Annul conference of the CFD Society of Canada*

[72] G. Broze and F. Hussain (1994), Nonlinear dynamics of forded trasitional jets: periodic and chaotic attractors, *J. Fluid Mechanics*, **263**, 93-132

[73] Hinze (1975), Turbulence, McGraw-Hill Ryerson

[74] Citriniti (1996), PhD thesis, State University of New York at Buffalo